Search for supersymmetry in events with intermediately displaced leptons

Author:
Neža Ribarič, B.Sc, M.Sc

Supervisor:
Prof. Dr. Roger Jones

A thesis submitted to
Department of Physics, Lancaster University
for the degree of
Doctor of Philosophy

February, 2024

Search for supersymmetry in events with intermediately displaced leptons

Neža Ribarič, B.Sc, M.Sc.

Department of Physics, Lancaster University

A thesis submitted for the degree of *Doctor of Philosophy*. February, 2024.

Abstract

As the ongoing operations of the Large Hadron Collider continue to push the boundaries of high-energy particle physics, there arises a compelling need to revisit our search strategies for potential new physics phenomena at the TeV scale. A considerable amount of work has been dedicated to the development of novel reconstruction techniques, one of which is presented in this thesis; the formulation and investigation of an adaptive multi-vertex fitting and finding algorithm. In the process, this endeavour unveiled an opportunity for a new study. In this study, the focus centres on the investigation of final states characterised by two displaced leptons that neither originate from the primary interaction point nor are connected to a common vertex. This signature provides sensitivity to new theoretical particles, sleptons, arising from an extension of the Standard Model called Supersymmetry (SUSY). The region of interest is an unexplored gap in phase space for LHC-accessible SUSY, existing between final states with leptons with large displacement and prompt leptons. From 139 fb^{-1} of $\sqrt{s} = 13$ TeV proton-proton collision data collected by the ATLAS detector, events with oppositely charged lepton pairs with millimetre-range impact parameters are selected. The background contributions are estimated using a data-driven background estimation method. Expected sensitivity to sleptons in final states with electrons is presented and the unblinded results in final states involving two muons. Results are consistent with the background hypothesis, therefore limits on slepton lifetimes and masses are set in the di-muon channel.

Acknowledgements

Achieving a PhD has been a lifelong aspiration of mine, and it still astonishes me that I have reached this milestone. The journey has been far from easy, and I owe my success to the remarkable individuals who supported me along the way.

I am profoundly thankful for the opportunity to be a part of an extraordinary research institute that welcomed me as a driven master's student. They guided me through the intricacies of data analysis and provided profound insights into the realm of particle physics. My sincere appreciation goes to my mentor, Prof. Dr. Roger Jones, whose pivotal role helped me establish myself in the academic community. Under his guidance, numerous opportunities unfolded before me, exceeding even the most ambitious expectations I've had for myself. Special thanks to Maria for her unwavering support in all physics-related matters, Melissa for patiently teaching me about ATLAS and SUSY, and Andy for enduring with me through all these years; challenging my ambitious yet nonsensical ideas, and especially assisting with coding challenges, there have been many along the road.

Beyond the academic support system, I am indebted to my exceptional friends who tolerated countless discussions about my research, whether in the gym, R1, or atop mountains. My heartfelt gratitude goes to Maja, James, David, Jurij, Julija, Alina, and Rob.

Lastly, my journey would not have been possible without the unwavering support of my parents. I want to convey my deepest appreciation for their belief in my abilities during moments of self-doubt, for shining a light when I was lost in darkness, and for allowing me to evolve into the person I am today. It deeply saddens me that I cannot share the fruits of this labor with my father, from whom I have learned so much. Concluding my PhD journey, I can sincerely express immense pride in my accomplishments, and I am confident that he, too, is equally proud of me.

Declaration

I declare that the work presented in this thesis is, to the best of my knowledge and belief, original and my own work, except where explicit reference and citation is made to the work of others. The material has not been submitted, either in whole or in part, for a degree at this, or any other university.

Neža Ribarič

List of Tables

List of Figures

Contents

Chapter 1

Introduction

1.1 Problem Overview

Human curiosity is an innate trait that drives our relentless inquiry into the structure and origin of the world we inhabit. The question of what are the fundamental constituents of matter and the forces governing their interactions has captivated the minds of philosophers and physicists for millennia. In response the Standard Model (SM) was formulated in the 1950s and has since been vigorously tested. It provides an explanation to almost all phenomena we see in experiments with remarkable accuracy. Yet, like a story with an unresolved mystery, the SM encounters difficulties in providing a complete and cohesive explanation for its structure and other phenomena, like astronomical observations of dark matter. Thus, in response to these limitations, many Beyond the Standard Model (BSM) theories emerged to extend and enhance the SM. Many of those have already been subjected to experimental testing, however these endeavours have not yet yielded conclusive evidence, leaving the quest for understanding the structure of the universe ongoing and ever-fascinating.

Currently, the world's largest particle physics facility seeking to find hints of BSM is the Large Hadron Collider (LHC) situated at the European Center for Nuclear Research (CERN). While there are multiple experiments at CERN and on the LHC, this thesis uses data collected by A Toroidal LHC Apparatus (ATLAS), the largest among the four primary detectors positioned on the LHC ring. Operating at centre-of-mass energy $\sqrt{s} = 13$ TeV, the LHC collides protons, providing rich environment for testing the SM and probing

various BSM phenomena. As we anticipate future hadron collision campaigns at the LHC, it is noteworthy that while the collision energy is expected to increase by a small margin, there will be a substantial increase in the amount of collected data. This prompts us to reevaluate our existing search strategies and examine potential oversight in our pursuit of new physics at the TeV scale.

1.2 Research Questions

The ATLAS detector was designed with the primary objective of detecting new heavy particles that decay almost immediately after production. The decay products are said to be prompt and point back to the interaction point. However, within the realm of particle lifetimes, there exists a fascinating territory characterised by particles living for a brief, but detectable, amount of time before decaying in the detector material. Identifying and reconstructing these distinctive signatures poses new challenges, yet they fall well within the capabilities of the ATLAS detector. Long lived particles are not only predicted by many BSM theories, they also find their place within the SM; notable examples being muons, heavy flavour and neutral hadrons. All of the processes are equally important to understand and reconstruct as efficiently as possible: identification and rejection of neutral hadron decays will improve b-tagging, which will in turn improve estimation of heavy flavour processes and therefore improve sensitivity to any BSM theories producing b-quarks in the final state. This prompted the following question, which was addressed during my qualification task (QT):

QT Question

Can we improve the performance of secondary vertex reconstruction algorithms?

Through this effort, an unexpected outcome emerged: the discovery of an unexplored region in LHC accessible phase space. This thesis presents a search for hypothetical new particles called *sleptons*. They are produced in pairs, each decaying to a detectable SM lepton and a weakly interacting particle that escapes our detection. Therefore, the focus is on final states with two SM leptons; two electrons, two muons or an electron and muon pair. The leptons must be displaced, do not point back to the interaction point and are not

connected to a vertex. Initially, the research direction at the LHC singularly focused on signatures involving prompt objects, where this signature would have been rejected. With a paradigm shift to increase focus on long lived particles during the Run 2 data taking period, subsequent analysis considered leptons with high displaced, a signature devoid of SM background. This search focuses on leptons with millimetre-range displacement targeting a previously unexplored gap in phase space for LHC-accessible BSM theories. This brings us to the central question tackled in this thesis:

Analysis Question
Could new physics lie in this narrow band of phase space?

The signature, two displaced SM leptons, is searched for in data collected by the ATLAS detector at the LHC between 2015 and 2018. Significant sources of background come from algorithmic inefficiencies and inaccurately modelled SM processes, necessitating the adoption of a data-driven background estimation method.

1.3 Thesis Structure

The thesis is structured into four main sections: first, a theoretical motivation for the search is presented; second, the experimental setup; finally, the qualification task and lastly the analysis strategy with results. Chapter 2 starts with a brief overview of the SM and the BSM theory called supersymmetry which motivated the model used in this analysis as well as in the validation step of the qualification task. Chapter 3 describes the LHC and ATLAS detector, from detector components to particle detection and reconstruction. Chapter 4 gives an in dept description of secondary vertex reconstruction and validation that was developed during the qualification task. It contains its own introductory and conclusion sections relating to the It can be read completely independently of the analysis for those interested in vertexing, but it may also be entirely skipped by those interested only in the slepton search. Chapter 5 gives context for long lived particles, reviews previous searches and defines the targeted phase space. Chapter 6 elaborates on the analysis strategy, including the definitions of signal regions and background estimation method. Chapter 7 describes the assessment of theoretical and detector systematics and finally the research

outcomes are presented in Chapter 8. I have been fortunate to receive a scholarship from the Centre for Doctoral Training, which enabled me to develop knowledge and skills in the field of large data analysis, manipulation and storage. As part of education, I have undertook a 6 month industrial placement as a Machine Learning (ML) expert at the BBC. Therefore special emphasis is put on Appendix 1.3, which presents the work I completed during that period.

1.4 Contribution Statements

Adaptive Multi Secondary Vertex Fitter

The development and implementation of a novel algorithm into the common reconstruction software used by ATLAS presented in this thesis is the work I have done as part of my qualification task to become an ATLAS author. The idea and some of the components have previously been developed for primary vertex reconstruction and have been cited appropriately. The work of adapting the components to fit the purpose for secondary vertex reconstruction, implementation into the Athena software, the development of a validation method and software package for secondary vertex reconstruction is my contribution to the ATLAS Collaboration.

Search for pairs of muons with small displacements (SR$\mu\mu$)

Parts of the analysis presented in this thesis, which involved the search for BSM phenomena in di-muon final states are published in Physics Letters B [1] and submitted as parts of a thesis [2]. My contribution to these works was the choice of background estimation method, its optimisation and validation. The analysis presented in that work was unfortunately not sensitive to superpartners of the tau lepton, therefore that data is re-analysed in this thesis to target those specifically.

Search for pairs of leptons with small displacement (SRee and SR$e\mu$)

The analysis of final states involving electrons in this thesis are solely my work. This includes, but not limited to, the choice of working points, producing and validating the datasets, optimisation and validation of background estimates.

Computer Says No

Although I have been involved in several projects during my industrial placement at the BBC, the biggest project and publicly disclosed work has been on the Computer Says No documentary [3]. For this project I acted as the main ML expert responsible for data acquisition, model choice and training, and ensuring the real-time performance of the software.

Chapter 2

Theoretical Motivation

The SM of particle physics provides a description of fundamental particles and their interactions. Over the course of several decades, it demonstrated remarkable robustness; predicting new particles before their discovery as well as high-precision measurements of its parameters. Despite its remarkable achievements, the SM is not without its limitations that have, in turn, led to the development of numerous BSM theories. Each of these BSM theories is designed to address specific shortcomings of the SM, wether it concerns a single limitation or a set of related challenges. This chapter aims to provide a brief overview of the SM, emphasising the role of symmetries within its structure. This lays a foundation for delving into a possible extension of the SM, specifically, the theory known as "supersymmetry". Supersymmetry postulates the existence of an additional spectrum of particles, some of which are targeted in this analysis.

2.1 The Standard Model

The SM is an effective Quantum Field Theory (QFT), combining quantum mechanics, special relativity and classical field theory. Much like the classification of elements in the periodic table was done by their properties, the particles in the SM are divided into two groups based on a quantum mechanical property called spin. *Fermions*, or the matter particles, are particles with spin $\frac{1}{2}$ and *bosons*, particles mediating interactions, have integer spin. The fermions can be further divided into quarks and leptons; particles with or without a quantum property called *colour*. The structure of particles within the SM is

schematically shown in Figure 2.1.

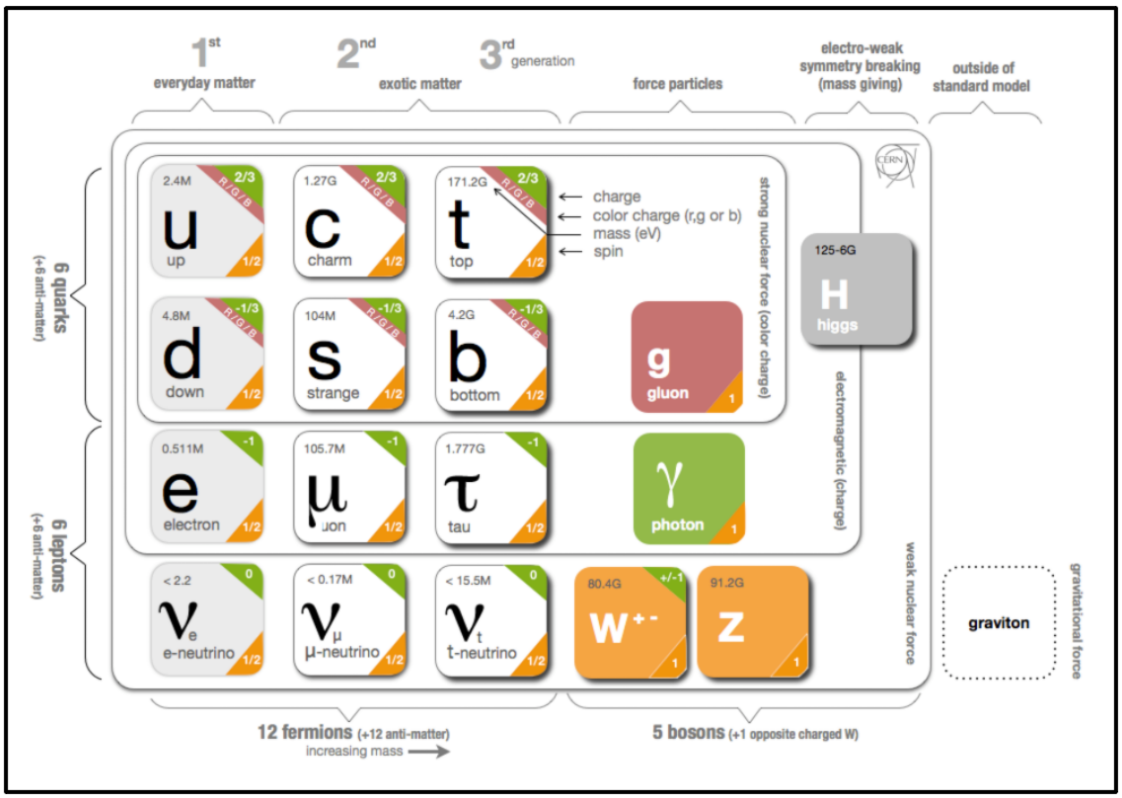

Figure 2.1: An illustration of the particle content of the Standard Model [4].

2.1.1 Leptons

There are three so-called flavours of leptons, l, which are ordered by mass: electron (e), muon (μ) and tau (τ). Each lepton has negative electromagnetic charge, an anti-particle with a positive charge and interacts via electromagnetic and weak forces. There are also three flavours of neutrinos ν, with an unknown mass ordering and no electromagnetic charge. The neutrinos have very small masses and interact only via the weak interaction, making them extremely hard to detect and are not studied at the LHC. Their presence in pp collisions is inferred from energy conservation and measured as missing energy. Each generation of leptons consists of a doublet, or pair, of the same flavour: electron (e) and electron neutrino (ν_e), muon (μ) and muon neutrino (ν_μ), tau (τ) and tau neutrino (ν_τ). In any SM process the number of leptons, L, of each flavour is a conserved quantity.

2.1.2 Quarks

Similarly to the charged leptons, there are three massordered generations of quarks, which are fermions that interact via electromagnetic, weak and strong forces. Like the leptons each generation is a doublet, the first consisting of an up quark (u) and down quark (d), the second of a beauty quark (b) and a charm quark (c) and the third consisting of a strange quark (s) and top quark (t). The charge of first element of the doublet is $+\frac{2}{3}$ and the second element $-\frac{1}{3}$, relative to the positron charge. Each quark has an additional property called colour, which is the charge of the strong force. The quark can be either red (R), green (G) or blue (B). Isolated, or bare, quarks have not been observed in nature, they rather group themselves to form colour neutral composite particles called *hadrons*. Hadrons have integer charges and are either *baryons*, composed of three quarks of different colour, or *mesons*, composed of two opposite colour quarks. Similar to leptons, the baryon number B is observed to be preserved in SM processes.

2.1.3 Force carriers

Interaction between the fermions can be described by the exchange of a boson particle. The photons (γ) are massless, charge neutral and mediate the electromagnetic interactions. The weak force carriers, $W^{\pm}$ and Z, are massive and have charges of ± 1 and 0 respectively. There are eight massless, charge neutral, but colourful gluons (g) that mediate the strong interactions. Lastly the Higgs particle is a massive, spin 0 boson whose field provides masses to the weak force carriers, quarks and leptons. Gravity is not described by the SM, its interaction strength is very small compared to quantum effects at the energy scale of current experiments.

2.1.4 Symmetries of the Standard Model

In the SM, particles and their interactions are described in terms of fields where the excitations correspond to the physically observable elementary particles. The kinematics of a field are governed by the Lorentz invariant Lagrangian density $\mathcal{L}$, generally referred to as simply the Lagrangian. A symmetry, in particle physics, is defined as a transformation of the Lagrangian in the theory in such a way that the predictions of the theory do not change. In elementary particle physics the two general classes of symmetries you can encounter

are $space - time$ symmetries and *internal* symmetries. The first group correspond to transformations of a field theory acting explicitly on space-time coordinates; rotations, translations, etc., and the second group contains transformations of the different fields in the field theory:

$$\phi^a(x) \to M^a_b \phi^b(x), \tag{2.1}$$

where indices a, b label the corresponding fields. If M^a_b is constant, the symmetry is said to be a *global* symmetry or in case of space-time dependance, $M^a_b(x)$, the symmetry is called a *local* or *gauge* symmetry. Symmetries play a crucial role in the SM for three reasons:

- for a field that is left invariant under a set of transformations, one can define an elementary particle based on conserved quantum numbers identified by the space-time and internal symmetries: mass, spin, charge, colour, etc.

- the interactions among particles are governed by symmetries, for instance through the gauge principle

- symmetries can hide or be spontaneously broken, which introduces a natural way to impose an energy scale to the system, but also implies that the fundamental symmetries of the theory may be larger than observed.

The symmetry group of the SM is

$$SU_C(3) \times SU_L(2) \times U_Y(1), \tag{2.2}$$

where C stands for colour, which is the charge of the strong force; L stands for left, because the weak interaction is chiral, meaning it couples only to left-handed particles where the handedness of a particle describes the orientation of the particle's spin relative to its direction of motion and lastly Y stands for *hypercharge*, which is the quantum number of the electroweak force.

2.1.5 Shortcomings

The discovery of the Higgs boson at CERN in 2012 stands as a monumental achievement [5]. However, it is important to note that, within the SM, there exists no inherent property that dictates the mass of the Higgs boson. At the energy scales currently achievable by experiments, gravity is very weak. Its effects become non-negligible at the Plank Scale, denoted as M_P and on the order of $\mathcal{O}(10^{19})$ GeV. The puzzle arises from the stark contrast between the experimentally measured Higgs mass, approximately 125 GeV, and, in comparison, the monumental Planck Scale. This is widely know as the *hierarchy* problem in particle physics, which implies the existence of new physics lying below the Planck Scale governing the mass of the Higgs boson. The implication stems from the nature of the experimentally determined mass, which comprises both the base mass, appearing in the Lagrangian, and quantum corrections that arise from interactions with other particles.

Considering a correction to Higgs mass, m_H^2, originating from a loop involving a fermion f of mass m_f coupled to the Higgs through the Lagrangian term $-\lambda_f H\bar{\Psi}_f\Psi_f$, the correction takes the following form [6]:

$$\Delta_f m_H^2 = -\frac{|\lambda_f|^2}{8\pi^2}\Lambda^2 + ... \tag{2.3}$$

Here Λ represents a cutoff parameter, which ensures that finite amplitudes are obtained in the theory. It can be interpreted as the lowest energy scale, where the SM remains a valid theory, beyond which new physics must be introduced. The measured Higgs mass can then be rewritten as:

$$m_H^2 = m_{H,bare}^2 + \sum_i \Delta_i m_H^2, \tag{2.4}$$

where the sum is over all possible particles participating in the higher order loops. In the absence of new physics beneath the Planck Scale, the turn of events that lead to the difference between two substantially large quantities, namely $m_{H,bare}^2$ and $\sum_i \Delta_i m_H^2$, lead to the relatively small measured Higgs mass seems "unnatural" to physicists. This is commonly referred to as the "naturalness" problem.

Another enigma on a cosmic scale is known as the "Dark Matter" problem. Astro-

nomical observations have revealed the existence of a novel form of matter constituting approximately 85% of the total matter content in the universe, yet it remains entirely absent in the framework of the SM [7]. It earned the name "dark" due to lack of interactions via the electromagnetic force, so it does not absorb, reflect or emit any electromagnetic radiation. Instead its existence is inferred from its gravitational effects on other baryonic matter as observed through phenomena such as rotation of galaxies, gravitational lensing and cosmic microwave background. As the majority of the matter content within the SM consist of charged particles, it fails to provide a viable candidate. Numerous extensions to the SM have been proposed to address one or more of these unanswered questions. These extensions often impose additional symmetries under which some of the particles would be charged. This thesis focused on a search for evidence supporting the existence of a theory incorporating an overarching grand symmetry in the SM - a symmetry connecting fermions and bosons.

2.2 Supersymmetry

Supersymmetry (SUSY) [8] is a theory proposed and developed in the 1970s in which each fermion has a bosonic *super partner* with all the same quantum numbers except for spin. It is of no surprise that the theory developed shortly after the SM, since it involves a very basic idea; much like the colour SU(3) group of the SM reshuffles the colour states of a given quark flavour among themselves and the weak SU(2) group mixes fields appearing in the weak doublets, supersymmetry interchanges bosonic and fermionic fields. Super partners of ferminons are named $sfermions$ and the fermionic super partners of bosons are added "-ino" to their names. For example the super partner of the muon μ is a smuon $\tilde{\mu}$ and the super partner of a gluon g is the gluino $\tilde{g}$. It is worth mentioning that there is no equivalent particle to the smuon in the SM or any other proposed super partners. Imposing the supersymmetry necessarily involves the inclusion of new particles, which form so-called *super multiplets* together with their SM partners. Thus far, we have not observed any spin 0 or spin 1 particle with precisely the same mass as the electron or any other super partners with identical masses to their SM counterparts. However, their absence does not rule out the possibility of realising supersymmetry. It simply suggests that the symmetry is not exact. A similar issue exists within the SM, where if the symmetry listed in 2.2

were exact, it would imply that gauge bosons should be massless, which contradicts our observation of the heavy W and Z bosons. In the SM, this issue was resolved through spontaneous symmetry breaking via the Higgs mechanism. Therefore, one might hope to employ a similar trick to allow for heavier super partners.

2.2.1 Minimal Supersymmetric Standard Model

The Minimal Supersymmetric Standard Model (MSSM) [9] is the simplest realisation of SUSY introducing the minimal number of new particles to the SM to ensure its self-consistency. Within the MSSM, there exist two Higgs doublets: one interacts with up-type quarks, while the other interacts with down-type quarks and charged leptons. After the electroweak symmetry breaking, five distinct Higgs states emerge: A, H, $H^{\pm}$ and h. The latter is the lightest state and is presumed to correspond to the already discovered Higgs boson within the SM. The remaining Higgs particles, referred to as *higgsinos*, undergo mixing with the electroweakinos, the super partners of the electroweak gauge bosons. This mixing results in the formation of mass-eigentates known as the *charginos* and *neutralinos*. In total the MSSM has four charge neutral neutralinos, namely $\tilde{\chi}_1^0$, $\tilde{\chi}_2^0$, $\tilde{\chi}_3^0$ and $\tilde{\chi}_4^0$, along with two charged charginos $\tilde{\chi}_1^{\pm}$ and $\tilde{\chi}_2^{\pm}$. In the MSSM, each lepton from the SM has two "slepton" super partners, a right-handed $\tilde{l}_R$ and a left-handed $\tilde{l}_L$ state, where the left- and right-handed states mix to form mass eigenstates $\tilde{l}_1$ and $\tilde{l}_2$. The *squarks*, the super partners of SM quarks, mirror this pattern, where $\tilde{q}_R$ and $\tilde{q}_L$ states mix to form $\tilde{q}_1$ and $\tilde{q}_2$. With the particle count in MSSM doubling compared to the SM, a multitude of interactions emerge between the particles and sparticles as well as sparticles themselves. In general in each interaction of the SM, it is possible to replace two particles with their corresponding sparticles. In the SM the baryon number, B, and lepton number, L, conservation is not observed to be broken, however the additional interactions in MSSM can violate the B - L symmetry. Consequently, this opens the theoretical possibility for the proton to decay via a super partner into a positron and neutral pion. However empirical evidence suggest the proton is stable. A new conserved quantity, known as R-parity, is introduced to reconcile this. It is defined as:

$$R - \text{parity} = (-1)^{2s+3B+L}, \tag{2.5}$$

where s is the spin; B is the baryon number and L is the lepton number. All particles of the SM have R-parity of +1 and SUSY particles have -1. This imposes a stringent requirement: sparticles must be produced in pairs, and the decay of massive sparticles must occur in a cascade involving lighter sparticles and SM particles. If supersymmetry was exact, then the super partners would be mass degenerate and would have already been observed in experiments. The symmetry must be broken to allow for the masses of the super partners to be much heavier than the SM super partners. The lightest sparticle must then be stable, to conserve R-parity, presenting a candidate to solve the dark matter problem. Furthermore, the inclusion of super partners into the theoretical framework introduces additional contributions to the Higgs mass. These contributions have the opposite sign than the terms arising from the SM particles, offering an elegant solution to the hierarchy problem. However, this relies on the assumption that the masses of the sparticles are only slightly greater than those of their SM super partners. While searches for SUSY have not yet yielded concrete evidence, the prospect remains promising, as it suggests that new physics may be within reach at the TeV scale and the LHC.

2.2.2 Gauge Mediated Supersymmetry Breaking

Given all the theoretical successes of supersymmetry, the central problem and prime focus of theoretical research is the question: What is the mechanism that breaks SUSY? In a Gauge Mediated Supersymmetry Breaking (GMSB) [10] model it follows a mechanism analogous to the Higgs mechanism, where SUSY is broken by a vacuum expectation value, $< F >$, of a superfield. However, this occurs in a so-called 'hidden sector', constructed of particles interacting with each other, but not directly with the 'visible sector', which is formed from SM particles and their super partners. It is therefore no longer the mechanism with which the SUSY breaking occurs, but rather the mechanism that mediates the SUSY breaking that dictates the way supersymmetry will manifest itself in our colliders. In GSMB the introduction of new gauge symmetries gives rise to heavy gauge 'messengers', which are carrying SM 2.2 charges and appear in loop or non-renormalizable interactions, that "inform" the SM about the SUSY breaking [10, 11, 12, 13]. GMSB models exhibit some notable characteristics:

- the gravitino $\tilde{G}$ is always the lightest supersymmetric particle, as it does not get its

mass through the gauge interactions. Its mass is proportional to the SUSY breaking and Plank scale $\frac{F}{M_P}$, where 10 TeV $\leq F \leq 10^3$ TeV, making the mass very small. The coupling to matter particles is proportional to $\frac{1}{F}$, which leads to decays lengths on μm to meter scale for matter particles it couples to;

- depending on the model, the next-to-lightest sparticle (NLSP) is either the neutralino $\tilde{\chi}_1^0$ or the slepton $\tilde{l}$. In the later case, the NLSP is either the stau $\tilde{\tau}$ or all three lepton flavours, $\tilde{e}, \tilde{\mu}, \tilde{\tau}$, are mass degenerate co-NLSPs.

This thesis searches for a model where the $\tilde{l}$ is the NLSP. The sleptons are pair produced in pp collisions and decay to the same flavour lepton and gravitino, $\tilde{l} \rightarrow l\tilde{G}$, as depicted in Figure 2.2.

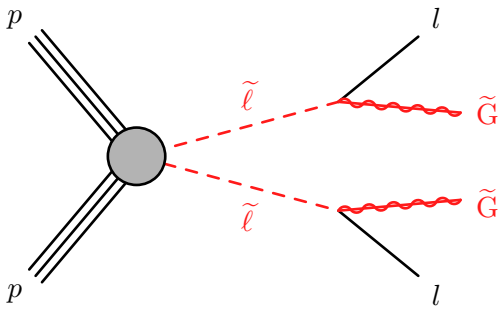

Figure 2.2: Feynman diagram showing the decay of a slepton, $\tilde{l}$, to a same flavour lepton, l, and gravitino, $\tilde{G}$.

The sleptons can manifest as either left- or right-handed states. Nevertheless, it is typically assumed that these states are mass-degenerate, while the production cross-section may differ depending on chirality. In case the $\tilde{\tau}$ is the NLSP, mixing can occur between the chiral states creating a mass ordered $\tilde{\tau}_1$ and $\tilde{\tau}_2$. Although the exact mechanism of SUSY breaking is no longer a concern, there are still 106 unknown parameters in MSSM [14]: 26 masses, 37 angles and 43 phases. In this thesis, as well as in numerous other searches at the LHC, a *simplified* model is used. In contrast to the full SUSY models, simplified models are more generic, with a smaller number of parameters that are directly related to observable quantities in the detector, such as particle masses and lifetimes. The lifetime of the slepton can be expressed as [15]:

$$c\tau \approx 100\mu\text{m} \left(\frac{100 \text{ GeV}}{m_{\tilde{l}}}\right)^5 \left(\frac{\sqrt{F}}{100 \text{ TeV}}\right)^4. \tag{2.6}$$

Hence, even at the lower ranges of SUSY breaking scales, the sleptons will travel a small distance before decaying inside the ATLAS detector. Consequently this results in a *displaced* signature of the observable decay product, i.e. the SM leptons. The majority of previous SUSY searches conducted at the LHC have predominantly used *prompt* tracks, or vertex-associated signatures. These conventional approaches lack sensitivity required to detect sleptons predicted in this model.

Chapter 3

The Experiment

The world's largest and most powerful particle accelerator, the LHC, located on the French-Swiss border just outside of Geneva, Switzerland, started operating on 10th September 2008 [16]. It occupies the same tunnel that previously housed the Large Electron-Positron Collider (LEP), which remains the largest lepton collider ever constructed. LEP was used for precision measurements of the W and Z bosons, while concurrently hosting a broad and diverse physics programme. The LHC operates by injection of two beams, comprising either protons or heavy ions, which are subsequently accelerated along a 27-km-long ring before colliding at four intersection points. Each of the intersection points house a detector that investigates and analyses the physical phenomena arising from the collisions. Among these detectors, ATLAS and CMS serve as general purpose detectors, studying and measuring a broad spectrum of processes and particle properties within the SM. Additionally, they tirelessly seek evidence for new phenomena like supersymmetry. They were designed independently and function in a complementary manner, cross-validating each other's findings. ALICE and LHCb are designed to fulfil distinct roles: ALICE is dedicated to the study of quark-gluon plasma, while LHCb, characterised by its asymmetric design, studies the difference between matter and anti-matter in processes involving heavy flavour hadrons.

This thesis uses data collected only by the ATLAS experiment in proton-proton (pp) collisions during Run 2 of the LHC, spanning from 2015-2018 with a centre of mass energy of $\sqrt{s} = 13$ TeV. Therefore this chapter aims to provide an initial introduction to the fundamental principles and concepts related to particle acceleration. Subsequently, it

describes the coordinate system utilised by the ATLAS detector, followed by an in-depth exploration of the detector's individual components. The chapter then delves into the process of event selection at the detector level, concluding with a brief description of reconstruction techniques related to objects that hold particular relevance for this thesis.

3.1 A Large Hadron Collider

Throughout the history of particle physics, a broad range of accelerators have operated, each distinguished by its structure and the types of particles it accelerates. LEP operated by colliding electron and positron pairs, which yielded clean and well-understood collisions. These collisions occurred at energies determined by the beams' properties, given that both electrons and positrons are elementary particles. In contrast, the LHC accelerates protons, which are not elementary particles. When two protons collide within the LHC, it is their constituents-quarks and gluons-that interact, creating a much richer dynamic. The fraction of energy of the proton carried by the constituents is not a known quantity, but must be measured. The probability of finding a given constituent of the proton with a fraction x of the proton's momentum is described by the Parton Distribution Function (PDF). The PDF is difficult to measure, its uncertainty adding to the uncertainty of the final result. Therefore, while lepton colliders like LEP provide a very clean and controlled environments for precision measurements, hadron colliders offer a broader energy spectrum with each collision. This, in combination with smaller energy losses by synchrotron radiation, makes hadron colliders well-suited for the discovery of a multitude of BSM phenomena.

3.1.1 Injection Chain

Accelerators can generally be categorised into two primary types: linear or circular. The selection of accelerator type depends on their intended physics objectives and can collide charged particles of various different types. Linear accelerators propel a particle from the source to the opposite end, incrementally increasing the particle's energy during its journey. Subsequently it either injects the particles into another accelerator or collides them with another beam or stationary target. In contrast, a circular accelerator allows

the particles to complete many revolutions around the accelerator ring before progressing along the acceleration chain to a different accelerator or fixed target. Circular accelerators have the advantage of achieving higher energies within the same acceleration distance compared to their linear counterparts. However the initial energy upon entering the circular collider must be sufficient for the particles to maintain their orbit at that radius. The LHC is the last accelerator in a succession of particle accelerators. The data examined in this thesis describes collisions of protons that commenced their journey from a bottle of hydrogen. Electric fields strip away the electrons in the hydrogen atoms, leaving only protons. The protons are then injected into the first and sole linear accelerator, LINAC 2, which accelerated them to 50 MeV. Subsequently, the protons progress through a series of circular accelerators, including the Proton Synchrotron Booster (PSB), consisting of four superimposed synchrotron rings that accelerate the protons to 1.4 GeV. After this the protons enter the Proton Synchrotron (PS) and Super Proton Synchrotron (SPS), which further accelerate them to 25 and 450 GeV, respectively. Before entering the LHC, the proton beam is divided into two beams, each of which circulates the LHC in opposite direction, attaining an energy of 6.5 TeV. The entire injection chain, along with experiments at CERN, is illustrated in Figure 3.1.

3.1.2 Acceleration

The LHC and all the circular accelerators within the injection chain operate as synchrotrons, employing multiple Radio Frequency (RF) cavities for particle acceleration. RF cavities generate an oscillating electric field, wherein the negative field attracts protons at one end while the positive field repels them. Protons possessing too little/much energy, enter the cavity too late/early with respect to the oscillating field. Consequently, they are decelerated/accelerated by the cavity, but propagate through the accelerator at a constant speed once in sync with the RF cavities. This synchronisation results in a regular pattern within each proton beam, characterised by the formation of "bunches" of protons. The spacing between these bunches is determined by the oscillation frequency of the RF cavities, which at the LHS is set at 25 ns.

A diverse array of electromagnets are used to bend the beams around the circular accelerator, keep the protons in a tight beam, limit the spread of particles just after

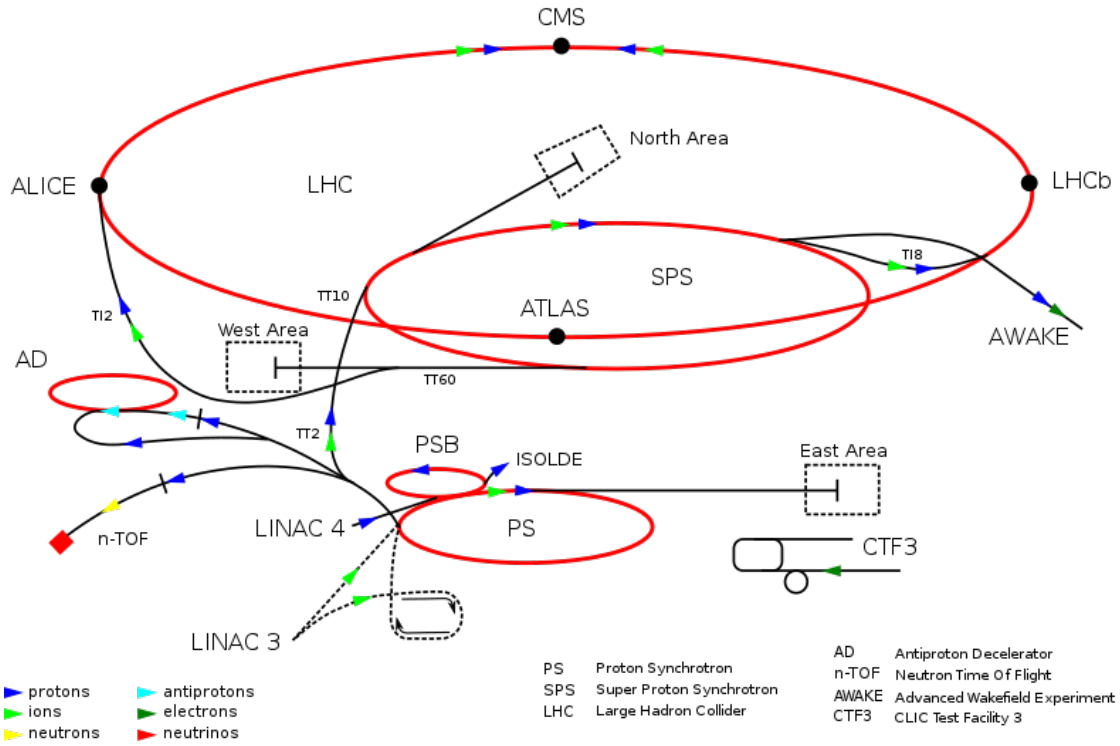

Figure 3.1: Overview of current particle and nuclear facilities at the CERN accelerator complex [17].

collision and to squeeze the beams into a smaller area just before collisions. Among these are 1232 superconducting dipole magnets made of niobium-titanium (NbTi), producing a field of 8.4 T and used to bend the beam into its circular shape. To maintain superconductivity, these magnets must be cooled using superfluid helium to an exceptionally low temperature of 1.9 K. Accompanying them are sextuple, octuple and decapole magnets strategically positioned to address edge effects at the extremities of the dipoles. Quadrupole magnets, on the other hand, are used to help focus the beams just before the interaction (collision) points (IP).

Particles that do not collide the first time the beams cross can be recycled, by enabling them to complete another revolution around the LHC ring. This recycling enables continuous collisions to take place over extended periods of time, often spanning hours. A period of collisions is called a *run*, while an entire collection of runs taken from 2015-2018 is called *Run* 2. When beam intensity drops, the run ends, beams are deliberately discarded, and the process starts again.

3.1.3 Luminosity

If the goal is to study unseen BSM physics, then alongside the centre of mass energy, $\sqrt{s}$, enough data must be produced to be able to study them. For a given process the number of events produced in a collision dataset is given by

$$N_{events} = \mathcal{L}_{int} \times \sigma_{process}, \tag{3.1}$$

where $\mathcal{L}_{int}$ is the integrated luminosity of the dataset and $\sigma_{process}$ is the cross-section for the given process. If we want to study rare processes (small σ), then more data ($\mathcal{L}_{int}$) is needed to have the statistical power in order to make a discovery. The cross-section is dictated by the theory, whereas the integrated luminosity is the integral of the instantaneous luminosity over the data taking period, where the instantaneous luminosity is related to the parameters of the accelerator as:

$$\mathcal{L} = \frac{N_1 N_2 f}{4\pi\sigma_x^*\sigma_y^*}\mathcal{F} = \frac{N_b^2 n_b f}{4\pi\sqrt{\epsilon_n \beta_x^* \beta_y^*}}\mathcal{F}, \tag{3.2}$$

where $\sigma_{x,y}^*$ are root mean square (RMS) of the beam width in the x and y directions; and $\mathcal{F}$ is a correction factor that takes into account geometric effects such as the beam crossing angle and beam length. The second equality holds specifically for the LHC, where it was rewritten to include: the number of protons per bunch N_b (assuming $N_1 = N_2$), number of bunches in the beam n_b, emittance ϵ_n, which describes the spread of the particles in the bunch and the value of the β-function at the IP, $\beta_{x,y}^2$. The β-function describes the size of the beam as a function of location. Several of these factors can be manipulated *in situ*, increasing or decreasing the luminosity depending on need. As an example: before the IP, the quadrupole magnets squeeze the beams, therefore increasing luminosity by decreasing β^*. During Run 2, the LHC produced an integrated luminosity of 156 fb^{-1}. Since ATLAS does not operate with a perfect efficiency, 147 fb^{-1} was recorded and 139 fb^{-1} could be used for physics analysis after data quality checks.

Pileup

High luminosity is of high importance when one wishes to study rare processes. However, it also gives rise to a dense environment in which these processes occur. When two bunches of protons cross there can be a number of concurrent pp collisions, referred to as *pileup*.

This poses a challenge in isolating the interaction of interest from less relevant ones. Pileup collisions are characterised by lower $\sum p_T$, generally lower energy QCD interactions producing sprays of low energy in the trackers and calorimeters. Consequently, this leads to increasing number of fake tracks and clusters or add energy to non-pileup detector signatures. There are two important quantities in estimating the amount of pileup, firstly the number of primary vertices and secondly the average number of inelastic interactions per bunch crossing, σ_{inel}:

$$\langle \mu \rangle = \frac{\mathcal{L}_b \sigma_{inel}}{N_b f}, \tag{3.3}$$

where $\mathcal{L}_b$ is the instantaneous luminosity per bunch, N_b is the number of bunches per beam and f the revolution frequency of the bunches. This number can be substantial as the instantaneous luminosity is greater that the pp inelastic scattering cross section. The mean $\langle \mu \rangle$ for Run 2 is ≈ 33, with the peak at ≈ 70 as can be seen in Figure 3.2. Pileup can be mitigated by reconstructing all hard scatter vertices in the event and removing detector signatures associated to non-primary vertices.

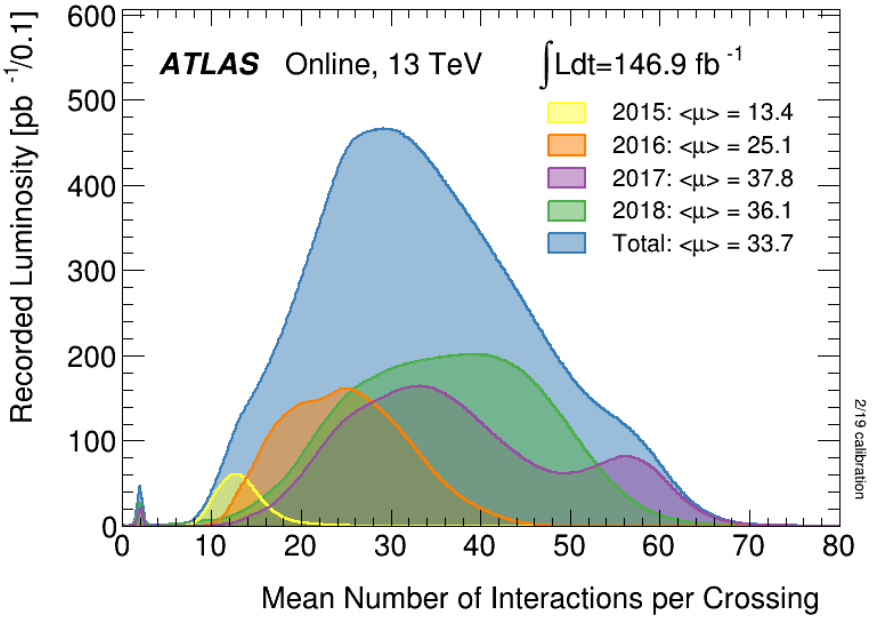

Figure 3.2: Average number of interactions per bunch crossing during Run 2 [18].

3.2 The ATLAS detector

The ATLAS detector, designed as a cylindrical, general-purpose particle detector [19, 20], serves the purpose of measuring particles and their interactions, whether originating from within the Standard Model or beyond. It measures 44 metres in length, 25 metres in height, and weight of approximately 7000 tons. The two beams collide in the centre of the detector with particles coming out of those collisions transversing through its three main sub-detector layers. Closest to the beam line lies the Inner Detector (ID), playing a vital role in the reconstruction of trajectories of charged particles. Next are the Calorimeters, responsible for measuring the energies of electromagnetic and hadronic particles. Finally, the Muon Spectrometer (MS), enables the measurement of trajectories of muons. In general each sub-detector is split into barrel and end-cap regions, which are positioned concentrically and perpendicularly to the beam pipe respectively. A schematic of the ATLAS detector is shown in Figure 3.3.

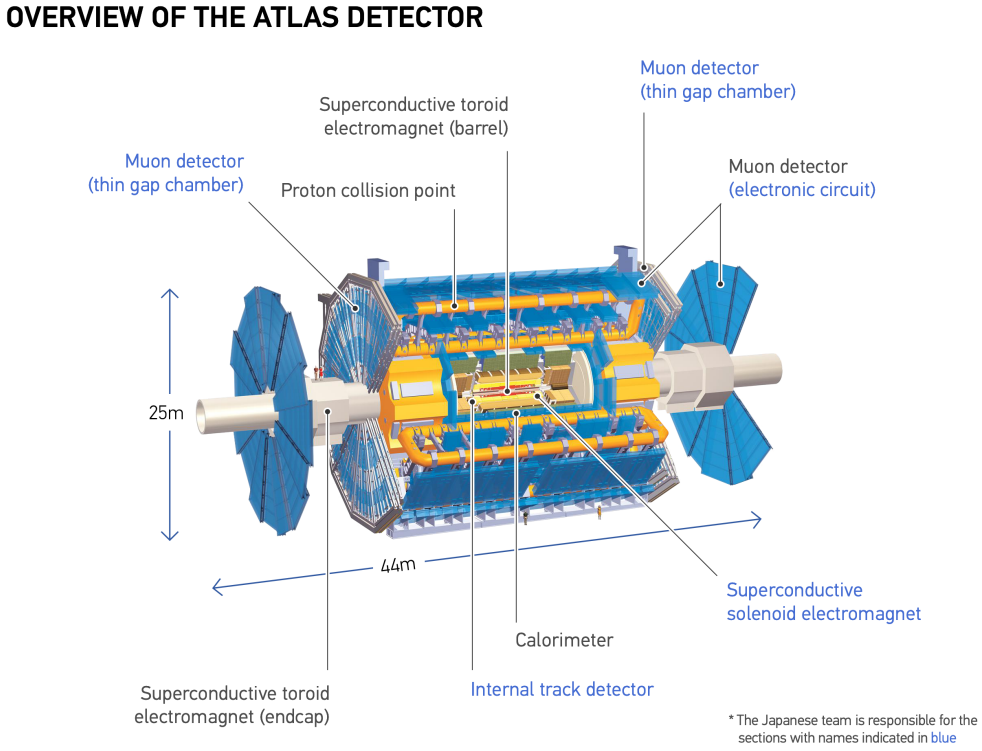

Figure 3.3: A diagram of the ATLAS detector [21].

3.2.1 Coordinate System and Variable Definitions

ATLAS uses a Cartesian right handed coordinate system with the origin at the nominal interaction point; where the proton beams collide. The z-axis is chosen to be along the beam pipe whereas the x-axis and y-axis point toward the centre of the LHC ring and upward, respectively. The azimuthal angle ϕ is measured in the x-y plane around the beam pipe while θ is the polar angle defined with respect for to the z-axis. The coordinate system can be seen in Figure 3.4.

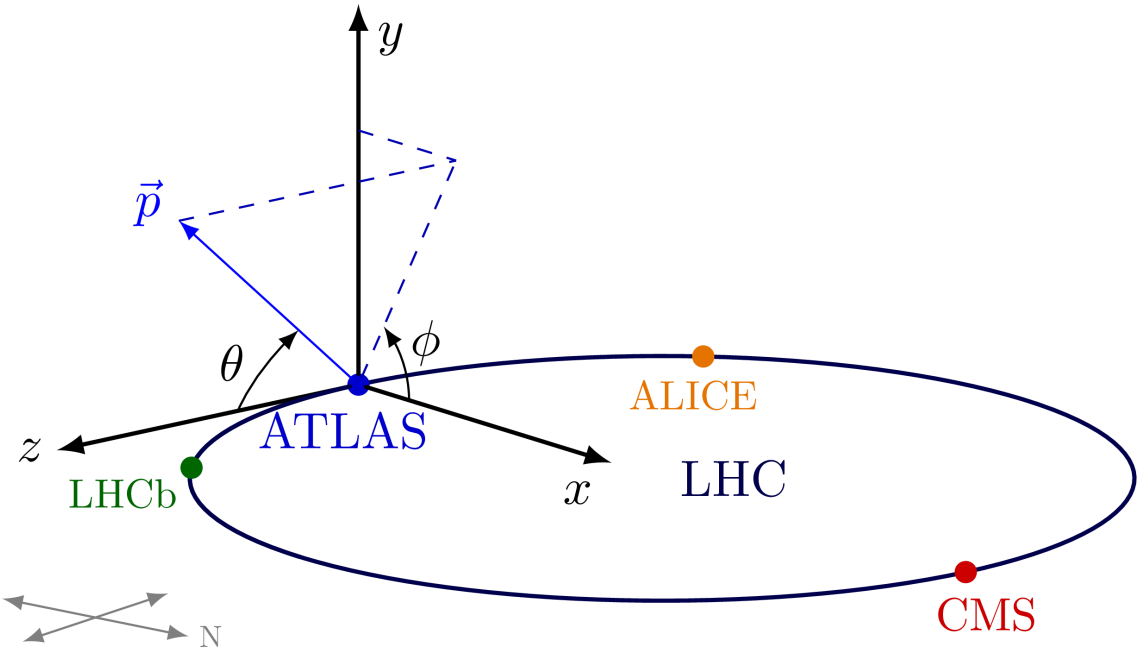

Figure 3.4: Depiction of the ATLAS coordinate system. It is defined such that the x-axis points towards the centre of the LHC ring, the y-axis points up from the cavern to the surface, the z-axis defines a right-handed coordinate system [22].

As protons are composite particles, the momentum is distributed between the constituent partons. Therefore in a given parton collision, the initial momenta along the beam pipe are not known. However, as the two beams travel towards each other along the z-axis, the momentum of the protons in the transverse plane, the x-y plane, is close to 0. It is therefore advantageous to define variables for particles coming out of the collision independent of the momentum along z-axis. The transverse momentum $p_T = \sqrt{p_x^2 + p_y^2} = p \sin\theta$ is momentum component in the x-y plane. Instead of θ, pseudorapidity, η, is used to describe

the angle from the z-axis, defined as

$$\eta = \frac{1}{2}\ln(\frac{|p|+p_z}{|p|-p_z}) = -\ln(\tan\frac{\theta}{2}), \tag{3.4}$$

where p_z is the component of the momentum along the beam axis. Particles perpendicular to the z-axis have $\eta = 0$, while those parallel to the beamline have $\eta \to \inf$. For highly relativistic and massless particles the difference in η is almost invariant under boosts along the z-axis so is the angle ϕ, therefore the radial distance between two particles defined as $\Delta R = \sqrt{\Delta\phi^2 + \Delta\eta^2}$ is commonly used. The Lorentz invariant mass of the two particles, labeled i and j, is defined as:

$$m_{i,j} = \sqrt{(E_i + E_j)^2 - (\vec{p}_i + \vec{p}_j)^2}. \tag{3.5}$$

The magnetic field, B, within ATLAS is not homogeneous, however for simplicity it is assumed so for the following definitions. A charged particle, with charge q, will have travel in a homogeneous magnetic field along a trajectory that can be represented by a helix. Since the majority of the particles studied with the ATLAS detector have a large enough p_T, their trajectory through the detector can be represented by a smooth curve of approximately fixed radius. The radius of curvature is defined as:

$$R = \frac{cp_T}{qB}, \tag{3.6}$$

the d_0 of a track is defined as the distance of closest approach of the track to the centre of the beam spot in the x-y plane:

$$d_0 = q(\sqrt{(x_c - x_{BS})^2 + (y_c - y_{BS})^2} - |R|), \tag{3.7}$$

where (x_c, y_c) is the coordinate of the centre of the curve the particle's track forms when extrapolated, R is the radius of this circle and (x_{BS}, y_{BS}) is the centre of the beam spot. z_0 of a track is the distance to the beam spot along the z-axis from the point at which d_0 is defined. For a visual depiction, please see Figure 3.10.

3.2.2 Inner Detector

The Inner Detector, positioned in close proximity to the beam pipe, plays a crucial role in reconstructing the paths of charged particles within the region defined by $|\eta| <$

2.5. To achieve exceptional momentum and vertex resolution, this detector comprises three distinct sub-components: the Pixel Detector, SemiConductor Tracker (SCT), and Transition Radiation Tracker (TRT). While the Pixel Detector and SCT are specialised for high-granularity precision tracking, the TRT not only enhances momentum resolution but also assists in distinguishing electrons from low-mass hadrons like pions. The ID and its subcomponents are depicted in Figure 3.5. All the information collected by these sub-detectors is utilised for track reconstruction, serving two primary purposes: primary vertex reconstruction, which pinpoints the location of the parton interaction, and secondary vertex reconstruction, used to determine the decay position of particles that exist for a brief duration while traversing through the ID. The ID is surrounded by a solenoid magnet that generates a 2 T magnetic field, curving the trajectories of charged particles as discussed in Section 3.2.1. As particles traverse the detector, they interact with individual modules, resulting in a detector response known as a "hit". Specialised software, described in Section 3.2.6.1, is then employed to link these hits into reconstructed tracks. Notably, the Pixel and SCT detectors play a critical role in secondary vertex reconstruction and impact parameter measurement, facilitating heavy flavour and τ lepton tagging.

The Pixel Detector

The Pixel Detector [24], situated closest to the interaction point, has the highest granularity. It is constructed using silicon n-type semiconductors with added impurities to enhance the number of potential charge carriers. When a charge particle transverses a semiconductor, electron-hole pairs are produced which drift towards the readout chips. If the signal exceeds a noise threshold, it is registered as a "hit". Pixels provide a very high signal-to-noise ratio, making them the preferred choice in regions with high occupancy, such as the immediate vicinity of the beamline.

The sub-detector comprises three barrel layers and two identical endcap regions, incorporating a combined total of 1744 silicon sensors. Each sensor is subdivided into 41,984 "standard" pixels measuring 50 $\times$ 400 μm^2 and 5284 "long" pixels of size 50 $\times$ 600 μm^2. The latter are necessary for covering the gaps between adjacent front-end chips. This pixel structure provides a resolution of 10 μm in the R-ϕ plane and 115 μ m in the $z(R)$ direction of the barrel (endcap). The Insertable B Layer (IBL), was added after Run

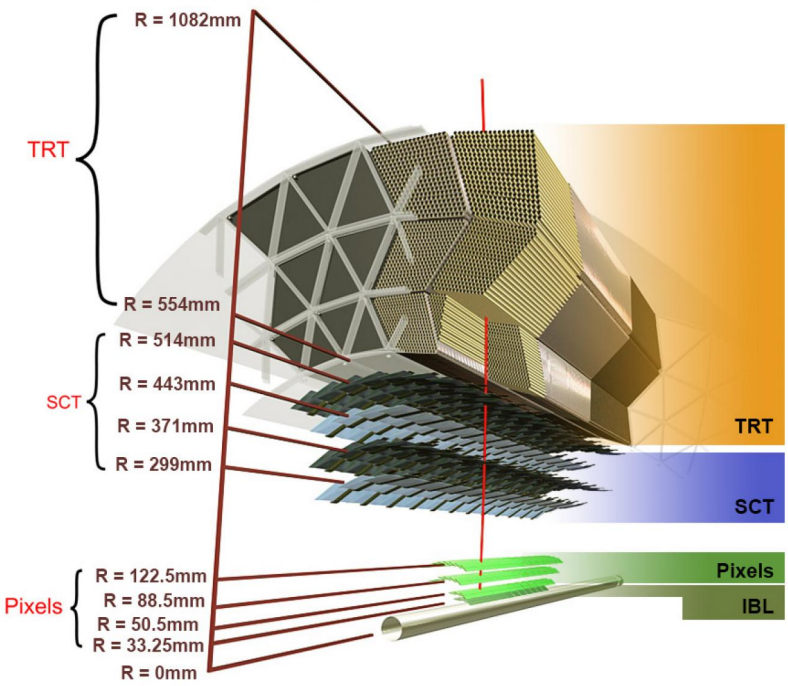

Figure 3.5: Structure of the ATLAS Inner Detector [23].

1 when the beam pipe's radius was reduced. It is composed of 12 million smaller pixels, offering a remarkable resolution of 8 μm in R-ϕ and 40 μm in z.

The Silicon Microstrip Tracker

The SemiConductor Tracker [25, 26] employs a concept similar to that of the Pixel Detector, but with longer and narrower sensors resembling "strips". This design reduces construction costs and limits the number of readout channels. The SCT consists of four barrels and two endcaps, each comprising nine disks. Each module is constructed from two single-sided strip sensors, which are glued back-to-back with a 40 $m$rad angle between them. This arrangement enables the strips to provide a 2D measurement of a passing particle. Due to the strip configuration of the SCT, it offers lower precision than the Pixel Detector, with a resolution of 17 μm in the $R\phi$ plane and 580 μm in the $z(R)$ direction in the barrel (endcaps). As a particle traverses the SCT, it crosses four bilayers of the detector, resulting in four hit measurements as it interacts with eight layers of material. The bilayers are arranged in concentric cylinders parallel to the z-axis in the barrel, while

the endcap configuration comprises nine disks on each side. The strips are 12 cm long and 80 μm thick.

The Transition Radiation Tracker

The Transition Radiation Tracker (TRT) [27, 28] is the outermost component of the Inner Detector and features a different design and construction compared to the previous sub-detectors. It consists of "straws", which are gas-filled proportional drift tubes. Each straw has a radius of 4 mm and comprises a gold-plated tungsten wire anode with a diameter of 30 μm at its centre, surrounded by a tube made out of a thick layer of kapton covered by an aluminum and graphite-polyimide layer. Argon gas is used inside the tubes, and when a charged particle passes through the straw, it ionises the gas, generating a signal that is read out by the electronics. The TRT extends the tracking volume by nearly 500 mm without the need for additional silicon. The wires are divided into two halves around $\eta = 0$. In the barrel, there are 52,544 straws that are 144 cm long and are arranged parallel to the beam axis, while in the endcaps, there are 122,880 straws, 37 cm long and arranged radially in wheels. Typically, a particle passing through the TRT leaves 36 hits, and the TRT provides an $R\phi$ accuracy of 130 μm per straw. The TRT's radius offers an advantage in momentum resolution and can provide timing information at the ns level. Between the straws, there is a polypropylene-polyethylene fibre foil, which has a different dielectric constant than air. This causes particles to generate transition radiation, the intensity of which depends on the mass of the particle. This provides an additional means of particle identification, particularly in separating electrons from pions.

Solenoid Magnet

The central solenoid magnet surrounds the ID providing a nearly uniform 2 T field that bends the trajectories of charged particles. The momentum of the particle can be inferred from the radius of the curvature in the x - y plane using equation 3.4. The solenoid magnet contributes approximately 0.66 radiation lengths; where the unit describes the mean distance over which the energy of an electron is reduced by a factor of e^{-1}. This feature enables the calorimeters to precisely measure the particle's energy. To achieve this, the magnet and the electromagnetic (EM) calorimeter share the same vacuum vessel, eliminating the need for two separate vacuum walls. The magnet itself is constructed using

an aluminum-stabilized NbTi superconductor, which allows for the generation of a high electric field while optimising the coil's thickness. The solenoid operates at a temperature of 4.5 K and has an axial length of 5.8 m and a radial thickness of 100 cm.

3.2.3 Calorimeters

Following the Inner Detector and Solenoid Magnet, there is the Calorimeter system [29], consisting of the electromagnetic and hadronic calorimeters. While their compositions differ, they all share the common design of being sampling calorimeters, constructed using alternating active and passive layers. When a particle passes through the calorimeter, it initiates a shower in the passive layers, and the energy deposited is then measured in the active layers. Each passive layer absorbs a portion of the shower, therefore the active layers measure only a fraction of the total energy. The size of the calorimeters is determined by their radiation length or nuclear interaction length, ensuring that the calorimeter effectively absorbs the majority of a particle's energy before it reaches the end of the calorimeter, thereby minimising any punch-through to the muon system. The only SM particles that manage to escape are neutrinos and muons. Neutrinos have an exceedingly low interaction cross-section, and muons possess a high critical energy threshold beyond which radiative energy loss processes become more significant than ionisation. Unlike the tracker, the energy resolution of the calorimeters improves as the energy of the particle increases due to enhanced signal generation.

Electromagnetic Calorimeter

The Electromagnetic Calorimeter is situated closest to the interaction point and employs Liquid Argon, LAr, in the active layers, with lead absorbers incorporated in the passive layers. It utilises a distinctive accordion design to mitigate the presence of dead zones resulting from cabling, reduce the overall length of cables, and consequently minimise readout times. The first layer has a very fine granularity in order to distinguish: photons from neutral pion decay to two photons, electrons from charged pions and to provide precise position measurement in η of photons, which do not produce an ID track. There is a small active layer, known as the presampler, located before the solenoid magnet, which is used to correct for the energy lost by the electrons and photons upstream of the

calorimeter. The third layer of the EM calorimeter is used to estimate any energy not sampled by the second layer, but also serves as a presampler for the hadronic calorimeter. A barrel module of the electromagnetic calorimeter is shown in Figure 3.6.

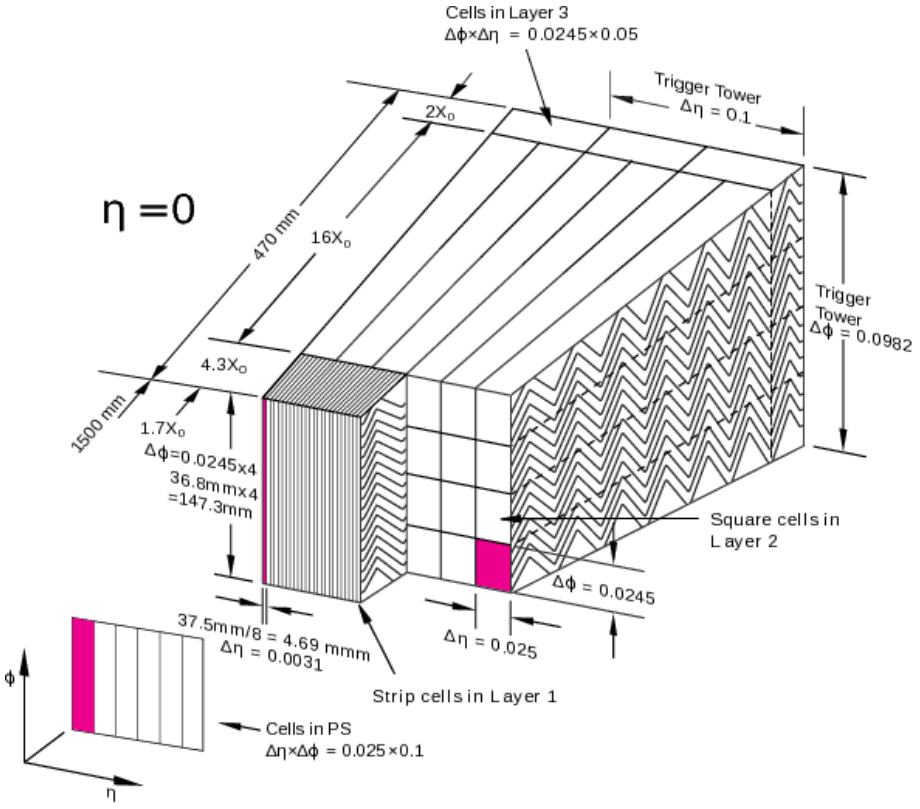

Figure 3.6: Diagram of a barrel module of the ATLAS ECal. [30]

Hadronic Calorimeter

The hadronic calorimeter surrounds the EM calorimeter and is made of steel absorbers with scintillating tiles serving as the active layers. The signal is read out by wavelength shifting fibres to two separate photomultiplier tubes (PMTs). The calorimeter is approximately 2 m long in the radial direction and covers about 8 interaction lengths.

Forward Calorimeter

The Forward Calorimeter (FCal) is, as the name suggests, in the forward region, 3.1 $< \eta <$ 4.9, and is designed to provide measurements in a high radiation environment. It is approximately 10 radiation lengths deep, consisting of three modules in each end-cap,

where all three use LAr as the active layer. The first layer uses copper as the passive layer and is designed to measure electromagnetic showers, whereas the other two modules use tungsten for the passive layer and target hadronic interactions.

3.2.4 Muon Spectrometer

The Muon Spectrometer [31] is the outermost subdetector, specifically designed to identify and measure the momenta of muons. Muons, which do not interact strongly and have substantial mass, are capable of traversing the EM calorimeter and HCal without significant energy loss. The Muon Spectrometer relies on a toroid magnet system providing a magnetic field orthogonal to the muon's direction of motion. This magnetic field bends the trajectories of muons as they navigate through high-precision tracking chambers and dedicated triggering chambers. Much like the detector itself, the magnet system exhibits discrete rotational symmetry in ϕ. The primary objective of the Muon Spectrometer is to provide an independent momentum measurement separate from the Inner Detector (ID).

The Muon Spectrometer has the capacity to measure muons with $|\eta| < 2.4$ and momenta within the range of 3 GeV to 10 TeV. It achieves a momentum resolution of 10% for $p_T > 1$ TeV. Precision tracking within the region $|\eta| < 2.7$ is accomplished using Monitored Drift Tubes (MDTs), which are replaced by Cathode-Strip Chambers (CSCs) in the innermost layer within the region $2.0 < |\eta| < 2.7$. Triggering and ϕ measurements are facilitated by Resistive Plate Chambers (RPCs) in the $|\eta| < 1.05$ region and Thin Gap Chambers (TGCs) within the $1.05 < |\eta| < 2.7$ region. These chambers are arranged in concentric cylindrical shells encircling the beam axis, with a single gap around $|\eta| < 0.1$ allowing for detector access during maintenance and service operations. The overall layout is schematically depicted in Figure 3.7.

Monitored Drift Tubes

The MDT chambers are composed of pressurised drift tubes filled with Ar/CO_2 gas and a thungsten-rhenium wire. The wire has a diameter of 50 μm, while the tube diameter is 30 mm. A charged particle passing through the tube will ionise the atoms in the gas, allowing the free electrons to drift towards the positively charged wire. The location of the electrons along the tube gives a position measurement, referred to as a hit and the time of arrival of

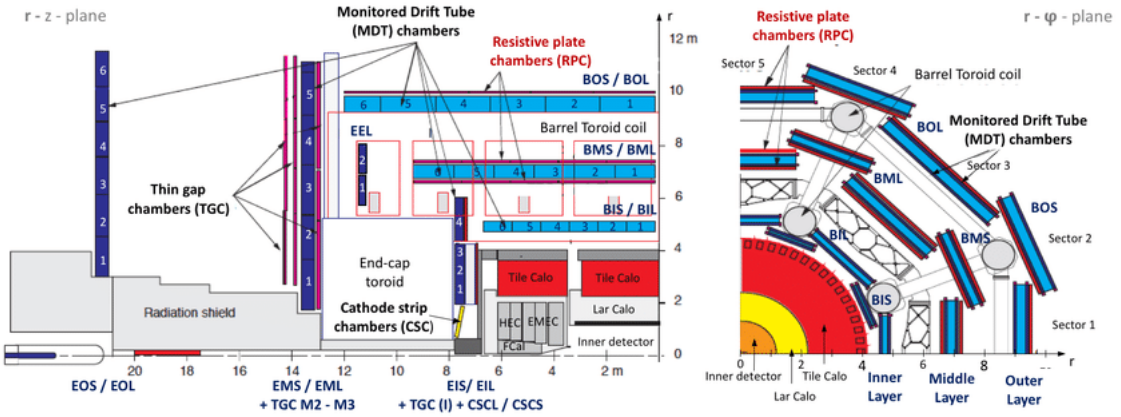

Figure 3.7: Cross-section of a quadrant of the ATLAS Muon Spectrometer in the Rz plane (left) and the $R\phi$ plane (right) comprising all detector modules. [32]

the first drifted charges to the wire determines the radius of the drift-circle. A single drift tube can provide a spatial resolution of 80 μm. The MDT readout provides a time profile of the measured hits with the peak of the distribution at t_0, at which the signal began, with respect to $t = 0$, which indicates the time that the pp interaction was measured by the ATLAS clock. Two multilayers of drift tubes separated by a mechanical spacer compose the MDT chambers. In the inner most chambers, the multilayers are composed of four layers of drift tubes, increasing the resolution to 30 μm, while the middle and outer chambers are composed of multilayers with three layers, increasing the resolution to 35 μm. The three chamber combination gives the required sagitta resolution with 15 measurements per muon passing the detector.

In comparison the CSCs are multi-wire proportional chambers with the radially oriented anode wires. The wires are placed between two cathodes, one having strips oriented perpendicularly to the wires and the other segmented parallel to the wire. The first gives a precision measurement of 40 μm in η and the later with 5 mm resolution in ϕ. The position of the CSCs are segmented in ϕ with each chamber consisting of four layers giving four precision measurements per muon transversing the detector.

Resistive Plate Chambers

In the barrel RPCs are used for trigger purposes. They are parallel plate detectors composed of of two phenolic-melaminic plastic laminate plates with a 2 mm gap and

4.9 kV/mm electric field between them. The chambers are filled with $C_2H_2F_4$ gas which is ionised by a passing muon. Both sides of the chambers have perpendicular readout strips providing both z and ϕ measurements. The chambers are composed of two detector layers each and positioned above or below each MDT chamber.

In the endcaps multi-wire proportional chamber TGCs are used. Similarly to the CSCs, they have perpendicular anode wires and cathode strips, however the placements of the individual components is more compact providing the necessary increase in speed. The fine granularity of the multi-wire proportional cambers readout provides good coverage in the endcaps where the inhomogeneity of the magnetic field is largest.

Toroid Magnets

Surrounding the MS is the toroid magnet system composed of a single barrel, $|\eta| < 1.4$ and two endcap, $1.6 < |\eta| < 2.7$, systems. They provide a magnetic field of 0.5 T and 1 T respectively. Both are made up of Al-stabilized Nb/Ti/Cu conductor with an air-core structure, which gives strong bending power while minimizing additional material that could result in additional scattering.

The two ATLAS magnet systems overlap in a transition region, $1.4 < |\eta| < 1.6$ resulting in a inhomogeneous field with geometric regions where the muon's trajectory is not bent at all and therefore adding to the challenges of triggering on hight p_T muons in that region.

3.2.5 Trigger and Data Acquisition

As mentioned in Section 3.1.2, the RF cavities dictate the spacing between the individual proton bunches. A bunch crossing occurs every 25 ns at the LHC with at average of 33 interactions per bunch crossing. If one wanted to store the entire detector output of a single event, this would equate to almost 1 TB of data. Subsequently the amount of data all of the ATLAS sub-detectors provide is too big to be stored and even processed at such a high rate. For this reason the ATLAS detector employs a real time event filter as part of the data acquisition system. Many of the events that occur at each bunch crossing are uninteresting, as discussed in Section 3.1.3. However, a great deal of caution and optimisation goes into the development of the trigger hardware and software. Events that do not pass the trigger selections are not recorded and therefore forever lost.

Trigger Architecture

The LHC generates events at a rate of 40 MHz, which must be reduced to 1 kHz by the ATLAS trigger system [33]. This reduction is achieved through two sequential steps, each operating on different systems.

The Level 1 (L1) trigger system is hardware-based and employs isolated detector components and regions of interest (RoI), specifically focusing on the calorimeters and MS, to lower the event rate from 40 MHz to 100 kHz. The L1 Calorimeter Trigger divides both calorimeters into coarse-grained towers with a size of $\Delta\eta \times \Delta\phi = 0.1 \times 0.1$. The algorithm selects towers with significant energy deposits to establish RoIs, subsequently summing the energy around each tower. The shape and size of the energy clusters are then used to identify individual physics objects, while the sum of the clusters in the event is used to compute Missing Transverse Energy (MET). In comparison the L1 Muon Trigger searches for high p_T muons by correlating hits in different layers of the RPC and TGC detectors. The ID is not used at the L1 stage due to the high number of readout channels and the computational intensity associated with track reconstruction, further discussed in Section 3.2.6.1.

The decision to accept an event at L1 is made by the Central Trigger Processor (CTP), which utilises a predefined trigger menu. Each trigger item in the menu includes a description of the event topology and energy requirements. The trigger architecture employed during Run 2 is illustrated in Figure 3.8. The full information from the entire detector is subsequently read out and forwarded to the High-Level Trigger (HLT). The HLT operates using CPU resources but receives significantly less data, affording it more time to make the final decision. However, there isn't sufficient time for complete full event reconstruction at this stage. Instead, the HLT is initiated by a L1 trigger, which defines the RoIs for subsequent finer reconstruction procedures. The HLT makes the final decision based on its own trigger menu, which includes more intricate event topologies and energy thresholds. Each entry in the trigger menu has a unique name. The naming convention is as follows: starting with defining the trigger level, "HLT", followed by a series of physics object of interest and their requirements; "e" for electron, "mu" for muons, etc.; the number before a physics object defines the number of those objects required in the event, where the number after the physics object defines the energy threshold in GeV

that is required by each of the objects; lastly the ID working points, impact parameter cuts are stated. The HLT makes the final reduction of the event rate to 1 kHz. Triggers exhibit a turn-on behaviour before becoming fully efficient. Consequently, HLT triggers have higher energy thresholds than L1 triggers to ensure that subsequent algorithms are executed in regions where the previous trigger is fully effective. Events that pass the trigger selection criteria are saved to disk and undergo more precise offline reconstruction. Offline reconstruction is further discussed in Section 3.2.6.

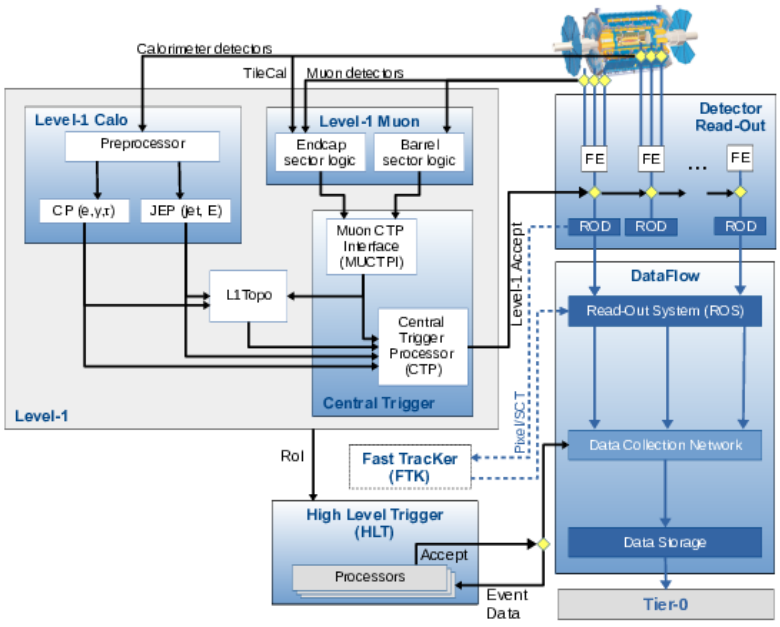

Figure 3.8: ATLAS trigger architecture during Run 2. Level-1 (L1) denotes the hardware trigger, which uses coarse granularity of the detector to accept events based on the information provided by the calorimeters and muon spectrometer only. High Level Trigger is software based and seeded by L1, meaning only measurements by the detector in regions of interest are considered. The tracks, used in this analysis and necessary for electron and muon identification, are reconstructed later in offline data processing [34].

3.2.6 Object Reconstruction

Each subdetector within ATLAS serves a distinct purpose in measuring various particles and their associated properties. Before the data captured by the ATLAS detector can be utilised for analysis, it must undergo a conversion process into a format comprehensible to physicists. An example is a charged particle leaving hits in the ID; reconstructed as a track, as well as energy deposit in the calorimeter; reconstructed as a calorimeter cluster. Both components are required to pass quality criteria before they are combine to a physics object; an electron. The process to reconstruct and identify physics objects is complex and centrally developed by the collaboration. Typically, the reconstructed objects are: electrons, muons, taus, photons, jets and MET. A depiction of signatures left in the detector by a variety of particles is displayed in 3.9. This chapter describes the reconstruction of only a subset of ATLAS objects and their quality criteria, which are used in this analysis: electrons and muons. Although both are elementary particles, in comparison to more complex objects like jets or MET, their reconstruction involves the inclusion of all ATLAS subdetectors.

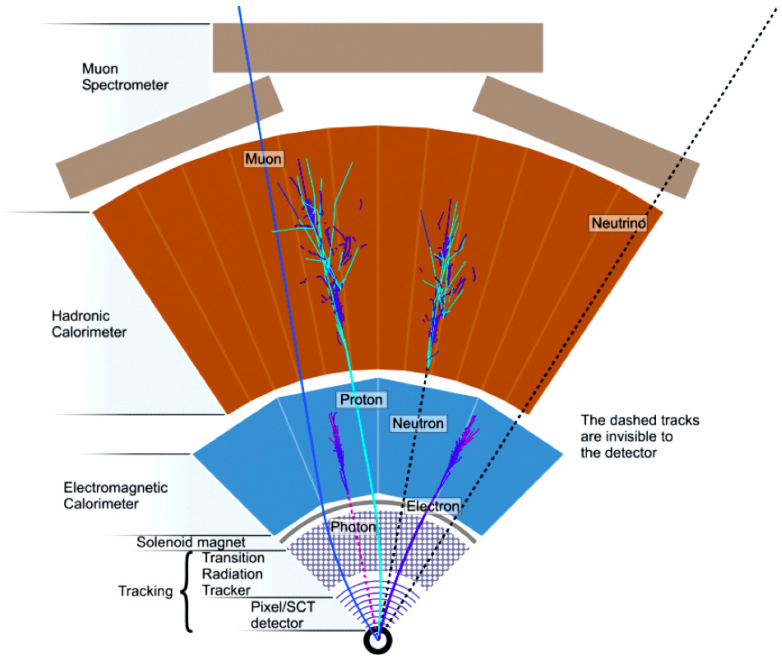

Figure 3.9: Particle signatures left in the detector for different particle types [35].

3.2.6.1 Track Reconstruction

The process to reconstruct a particle's trajectory from hits in the ID is a complicated process due to the density of particles in each event as well as the curvature of the tracks. Each track is completely described by five parameters measured with respect to the beam position:

- d_0: the transverse point of closest approach or transverse impact parameter
- z_0: he longitudinal point of closest approach or longitudinal impact parameter
- ϕ: the azimuthal angle of the track momentum
- η: the polar angle of the track momentum
- q/p: the ratio of the track's charge to the magnitude of its momentum

which can also be seen in Figure 3.10.

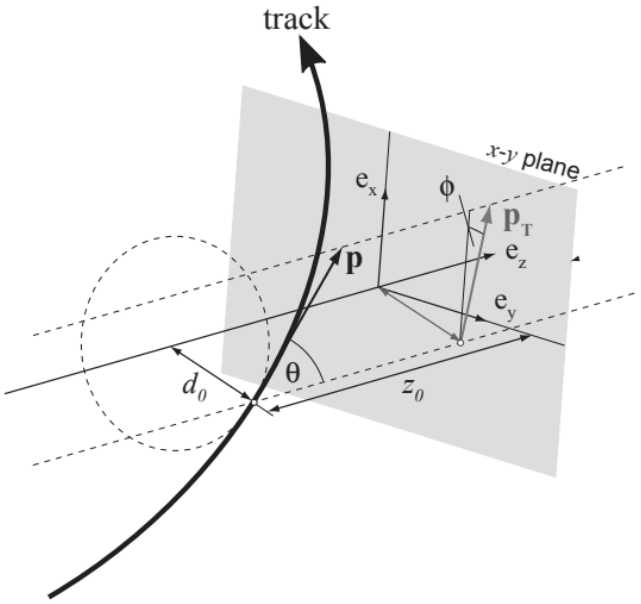

Figure 3.10: Visualisation of global track parameters [36].

The following subsections describe the steps of the standard track reconstruction algorithm used by the ATLAS collaboration. It is worth emphasising that no Large Radius

Tracking [37] is used in this analysis, which is a newly developed algorithm utilising left-over hits from standard track reconstruction to reconstruct tracks with large impact parameters.

Inner Detector Tracks

Broadly speaking the ATLAS tracking software first performs track reconstruction "inside-out" and then "outside-in" with respect to the interaction point, as illustrated in Figure 3.11. Both processes are preceded by a clusterization step in which charge deposits, exceeding a charge threshold in the Pixel and SCT subdetectors, are combined into clusters. This merging step assumes that the deposits were left by a single charged particle. A single pixel cluster or hits from both layers of the sterostrip in SCT form a three-dimensional space point. The "inside-out" approach starts by finding triplets of

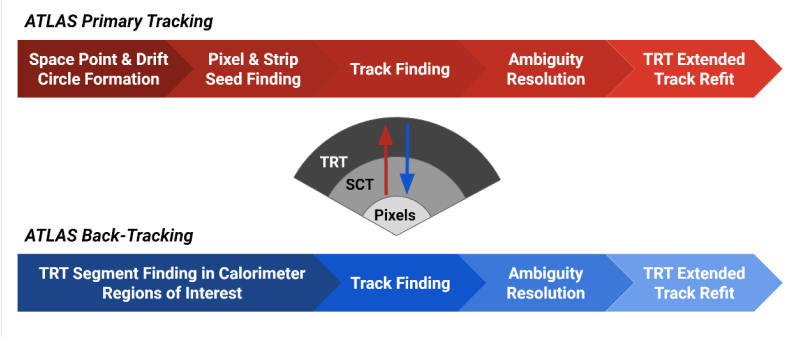

Figure 3.11: Diagram depicting ATLAS steps in track reconstruction [38].

space points in either Pixel or SCT, which form track seeds. They are refined by a very loose selection criteria to mitigate the computational expense and limit reconstruction of low-quality tracks. The seeds are used for constructing track candidates through a combinatorial Kalman filter. This filter recurrently expands the track seeds by incorporating spatial points from successive layers of the detector, extending both outward and inward along the radial direction. This approach allows for paralellization of a complex combinatorial process. Each successive layer can create several branches; one for each measurement in the next layer or a single branch for a missing measurement to account for detector inefficiencies. This facilitates building multiple track candidates from a single track seed. Each branch independently updates the linearisation and extends to the next layer, where the process is repeated. Branches lacking measurements in several layers

are removed and only those with best quality are selected in the end. Track seeds that fail the track finding selection are checked for compatibility with calorimeter clusters. If the seed is within a RoI of the calorimeter deposit, the track finding procedure is redone allowing for an additional "kink" in the track. This extra step is referred to as Bremsstrahlung recovery, and it aids in restoring the efficiency of electron reconstruction by accounting for the change in track direction caused by radiation. While the Kalman filter is effective in track reconstruction within high pileup environments and typically provides great precision, it is computationally very intensive.

All possible track combinations are resolved in the ambiguity solving step, which compares track candidates scores computed from a variety of quality criteria like number of holes (active sensor material layers without a measurement), χ^2 and p_T. Tracks are not allowed to share the same cluster. However, the cluster may be removed from the track candidate and its score recalculated. Finally, the track candidates are extended into the TRT in the same Kalman filter approach and re-fit with a global χ^2 fit. This method is optimised for reconstruction of prompt particles, those decaying immediately after their production. Neutral particles decaying after the first layers of the Pixel detector leave no hits, subsequently being rejected by track quality requirements of the "inside-out" method. To increase acceptance to long lived particles the so called "outside-in" approach starts from unused track segments in the TRT and extends them back into the SCT and Pixel detector in the same Kalman filtering approach. This step is only performed in RoIs determined by deposits in EM calorimeter, starting from segments of TRT hits within the RoI.

Muon Spectrometer Tracks

Rather than beginning with space points, MS hits are processed through a pattern matching algorithm known as the Hough transform. It tries to identify if a particular signature can be described using a known parametric form. The algorithm relies on a transformation from a physical to parameter space, where each point in physical space maps to a line in parameter space. The intersection of these lines in parameter space gives the values of the constants of the parametric form we are trying to describe them with. For example we could take a set of space points (x_i, y_i), which all lie on a line, $y = ax + b$.

A Hough transform maps all of the points from the $x-y$ space, to $m-b$ space, where each point (x_0, y_0),...,(x_n, y_n) maps to a line in parameter space. The intersection of these lines in parameter space is at (a_i, b_i), which define the lines in physical space with parameters a_i and b_i. This is sketched in Figure 3.12.

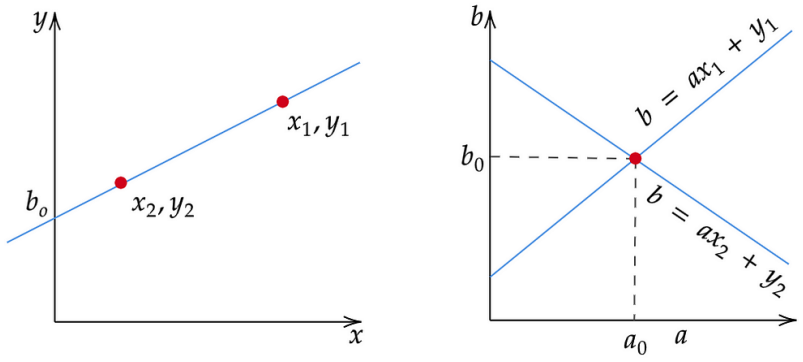

Figure 3.12: Illustration of a Hough Transform. Points in coordinate space (left) are transformed into lines in the Hough parameter space (right). Lines that cross each other at one point in Hough parameter space correspond to collinear points in coordinate space [39].

As the complexity grows exponentially with the number of dimensions and the pattern must be known a priori, this pattern finding algorithm can not replace the ID tracking algorithm. It is however very useful for reconstructing short straight-line tracks in the same MS station. These track candidates are referred to as 'segments'. Preliminary track candidates are formed by combining segments from different MS stations. Lastly the tracks are extrapolated back to the interaction point, where possible multiple scattering and energy loss in the calorimeters are accounted for. A global χ^2 is performed taking into account the bending of the muons trajectory in the inhomogeneous magnetic fields and a track candidate is accepted if it satisfies quality criteria.

3.2.6.2 Electrons

Electrons are reconstructed by combining a localised cluster of energy from the EM calorimeter and a track from the ID, that closely match in $\eta \times \phi$ space. The involvement

of photons, converted photons, charged hadrons and bremsstrahlung radiation make the identification and accurate measurement of electrons quite challenging.

Cluster Seed Reconstruction

Firstly calorimeter towers are formed, in $\eta \times \phi$ space, of size $\eta \times \phi = 0.0025 \times 0.025$. The energy of each tower is the sum of the first, second, third and the presampler, for $|\eta| < 1.8$, layers. Cluster seeds are formed using a sliding window algorithm, which moves a 3×5 window in $\eta \times \phi$ units in steps of 0.025 in either η or ϕ direction searching for localised energy deposits. If the energy sum is above a threshold, $E_T > 2.5$ GeV, and is a local maximum, this window is considered a cluster. If two cluster seeds are in close proximity, the candidate with the higher transverse energy is kept, providing the difference from the other candidate cluster is more than 10%, otherwise the candidate with the highest E_T central tower is kept and the duplicate cluster is removed. Inefficiencies of the cluster seeding procedure are negligible compared to the track reconstruction and track-cluster matching. As a function of E_T, the efficiency ranges from 65% at $E_T \approx$4.5 GeV, to 96% at $E_T \approx$7 GeV to more than 99% above $E_T \approx$15 GeV [40].

Track Reconstruction

Track candidates that cannot be extended to the required silicon layers, as detailed in Chapter 3.2.6.1, and are found in close proximity to a quality EM cluster, undergo another pass at track reconstruction. The tolerance for energy loss due to bremsstrahlung is increased, allowing for up to 30% of energy loss at each intersection of the track with detector material. Track candidates with $p_T > 400$ GeV are fit under the hypothesis, that the track originates from a pion. If the fit fails and the track is in close proximity of a EM cluster, the track is assumed to have been produced by an electron where another degree of freedom is added to the χ^2 calculation that accounts for additional radiation. With this extended tracking procedure, efficiency of track-fitting for electrons reaches 98% for electrons with $E_T > 10$ GeV [40]. Tracks that are in close proximity with EM clusters and possess a minimum of four silicon hits are subjected to an additional fitting procedure that employs the optimised Gaussian-Sum Filter (GSF). This procedure, which builds upon the Kalman filter framework, is specifically designed to address non-linear effects associated with bremsstrahlung radiation. The GSF consists of a number of Kalman filters running

in parallel, where each track parameter is approximated by a weighted sum of the gaussian functions; six describing the material-induced energy loss and up to twelve describing the track parameters. When accounting for radiative losses with the GSF method, all track parameters related to the bending-plane, like transverse impact parameter significance, are expected to improve.

Electron-candidate Reconstruction

The electron reconstruction process is completed by associating GSF track candidates with calorimeter seed clusters. The cluster-to-track matching closely resembles that of the GSF procedure, but with stricter requirements. In cases where multiple tracks are linked to a single cluster seed, the primary electron track is identified as the one exhibiting superior quality and closer proximity to the cluster. However, if the primary track lacks Pixel hits and is associated with a secondary vertex, it is categorised as a photon, likely originating from a conversion process. Further classification of electrons or potential photons is performed based on parameters like E/p, p_T, and the number of pixel hits. Finally clusters are reconstructed around the seed clusters using an extended window by simply expanding in size in either η or ϕ on either side of the cluster. The energy of the final electron is computed from the calibrated energy of the extended-window cluster. Above E_T $\approx$15 GeV the efficiency of reconstructing an electron with a track of good quality varies from 97% to 99% [40].

Electron Identification

Electrons are further distinguished from photons, light jets, and leptonic heavy flavour decays through a likelihood-based (LH) electron identification method. This approach offers more flexibility compared to a simple cut-based identification, which may reject electrons based on a single criterion, and it incorporates variables with similar distributions in both signal and background. Some variables are employed as thresholds during the identification process, such as the number of pixel and silicon hits. Others are utilised to construct the likelihood function, such as track quality and energy ratios between layers of the EM calorimeter. The electron LH relies on the products of signal (L_S) and background

(L_B) likelihoods derived from a set of n probability density functions (pdfs) P:

$$L_{S(B)}(x) = \sum_{i=1}^{n} P_{S(B),i}(x_i), \tag{3.8}$$

where x is the vector of the various quantities used in the construction of the likelihood function and $P_{S(B),i}(x_i)$ corresponds to the signal (background) pdf for quantity i at value x_i. For each electron candidate, a discriminant d_L is formed:

$$d_L = \frac{L_S}{L_S + L_B}, \tag{3.9}$$

on which the electron LH identification is based on. For convenience the operating points are chosen based on the inverse sigmoid function of this discriminant, where values larger than the chosen cut mean the electron is a signal electron.

3.2.6.3 Muons

Hits from various segments in multiple layers are fit to from track candidates. The fitting procedure is seeded from segments in the middle layers of the MS, where more trigger hits are available, then extrapolated inward and outward in R. The extrapolation relies on relative positional and angular information as well as the fit quality and hit multiplicity of the segments. At least two segments are required to form a track, except in regions with limited detector coverage. Similarly to the ID track finding, an ambiguity solving step removes track candidates and allows for a segment to be shared with at most two tracks. A χ^2 fit is performed where outlier hits can be removed and additional hits consistent with the track candidate can be added.

Combined Muons

This thesis makes use of muons identified as combined muons (CB), combined "inside-out" (IO). IO muons are reconstructed by extrapolating the ID tracks to the MS and requiring at least three loosely aligned MS hits. CB muons are identified by matching the MS tracks to the ID tracks and performing a combined track fit, taking into account the energy loss in the calorimeters. Hits from the MS, not the ID, may be added or removed to improve the fit between the two tracks.

Muon Identification

In comparison to electrons, muon identification working points employ a cut and count approach, where reconstructed muons are said to pass the medium working point in the barrel region of the detector if:

- they are CB or IO muons
- they include hits from at least two precision stations, except in the region $|\eta| < 0.1$, where muons can include hits from only one precision station, if they additionally include at most one precision hole station.

A "precision station" is defined as the MS station having at least three hits in the MDT and CSC detectors, whereas a 'precision hole station' is a station with less than three hits, but at least three are expected given the muon's trajectory, the detector layout and operational status. Finally a requirement is placed on the compatibility of the MS and ID tracks, namely the q/p significance, the difference between the charge and momentum ratio in the ID and MS divided by their uncertainties summed in quadrature, is required to be less than 7.

3.2.6.4 Overlap Removal

Each of the reconstruction chains described above, as well as the reconstruction of other analysis objects like τ leptons and jets, are run simultaneously. This means that one track of calorimeter deposits can be shared between multiple objects. For this reason an overlap removal procedure is applied in a sequential way. Firstly electron-electron overlap is performed, where the η and ϕ in the second layer of the calorimeter is compared. In case overlap is found the electron not reconstructed by the cluster based algorithm or the lower p_T electron is rejected. Next electron-muon overlap is performed by comparing the muon and electron ID tracks. In case the electron and muon share the same track or the electron track is within $\Delta R < 0.01$ of the muon track, the electron is rejected.

3.2.6.5 Isolation

To reject leptons coming from heavy flavour processes, the leptons in this analysis are required to be isolated. This means they are not surrounded by much other activity from

the hard scatter in either the ID or Calorimeters. Isolation is defined as a scalar sum of energy in a cone of radius ΔR around the lepton track, which depends on the p_T of the lepton. An example is the track based isolation variable $p_T^{varcone30}$, which is the scalar sum of the transverse momenta of tracks with $p_T > 1$ GeV in a cone with:

$$\Delta R = \min\left(\frac{10\text{GeV}}{p_T}, 0.3\right). \tag{3.10}$$

The cone size gets smaller for larger momenta due the smaller opening angle of its decay products, however the cap at 0.3 prevents the cone getting too small for very high p_T. Similarly for calorimeter based isolation we define a variable $neflowisol$, which is the sum of transverse energy in the calorimeters in a cone around the lepton track, $E_T^{topocone}$. $E_T^{topocone}$ is calculated by subtracting the energy deposit of the lepton itself, the core energy, from the raw whole topocluster energy measured by the detector then applying pile-up and leakage corrections. For both calorimeter and ID track isolation, values are centrally defined by ATLAS to determine if a lepton is isolated. In comparison to muons, isolation calculation for electrons is more complex as electrons are more likely to emit bremsstrahlung radiation. These photons can convert to electron positron pairs, however these secondary tracks are considered part of the electron's p_T. Electrons also leave their own energy deposit in the EM calorimeter, which needs to be subtracted from the $E_T^{topocone}$ calculation.

Chapter 4

Adaptive Multi Secondary Vertex Finder

4.1 Introduction

An Adaptive Multi-Vertex Finder (AMVF) [41] has been developed for the primary vertex reconstruction and showed great improvement in performance in high pile-up environment, which can be seen in Figure 4.1. This prompted an interest in implementing the adaptive multi-vertex approach to secondary vertexing in hopes of reproducing the increase in performance. The Inclusive Secondary Vertex Finder (ISV) has also been recently implemented for reconstructing secondary decay along with the AMVF, but neither have been previously used, validated or compared. Both the iterative and adaptive multi-vertex approach use the same adaptive estimator to calculate weights of tracks, probabilities that the tracks belong to the vertex in the vertex fit and the deterministic annealing procedure to progressively de-weight and reject outlier tracks. However, the AMVF uses a global track pool to select tracks for new vertex candidates whereas the iterative method uses only tracks not compatible to the previously fit vertices. Subsequently, in AMVF the tracks can have weights to multiple vertices. Although both fit vertices iteratively, the AMVF fits all vertices sharing tracks with the current vertex candidate simultaneously. The main objective of the Qualification Task has been the implementation of the adaptive multi-vertex approach to secondary vertexing, which is described generally in Section 4.2 and in detail for both ISV and AMVF in Sections 4.2.2.3 and 4.2.2.3 respectively. A

new secondary vertex validation package has also been developed, which is described in detail in Section 4.3. Finally Section 4.4 provides a comparison of the two vertex finders to other finders using the validation package and briefly discusses possible upgrades as part of future continuation of this work.

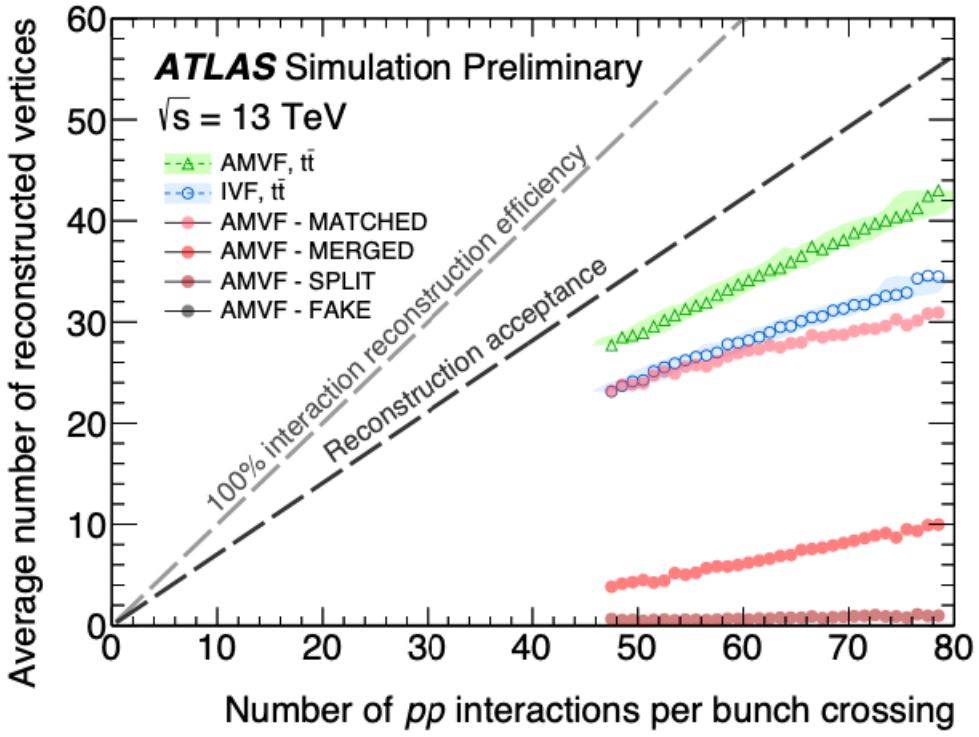

Figure 4.1: Number of reconstructed vertices as a function of average interactions per bunch crossing [41].

4.2 Vertex Finding and Fitting

The ATLAS detector is composed of several sub-detectors from which the ID plays the major role in vertex reconstruction. The ID itself is composed of the Pixel, SCT and TRT detectors, which together provide an $R\phi$ resolution of $\approx$ 10 μm, 17 μm and 130 μm, respectively. On average a charged particle transversing through the ID will provide 4+(4×2)+30 measurements [42], which allows for an efficient reconstruction of the particle's trajectory and subsequently the decay vertex that produced it. In a typical

collision, the interaction will produce a primary vertex, however the particles resulting from the primary interaction may themselves decay further in the detector producing additional secondary vertices. Those can be from photon conversions to electron-positron pairs, cascade decays such as b-hadron decays, long-lived neutral particles such as Λ^0, $\overline{\Lambda^0}$ and K_S^0, but they are also predicted in several beyond the Standard Model theories. They are all equally important to understand and reconstruct as efficiently as possible as, for example, the successful reconstruction, identification and rejection of V^0 decays improves the performance of b-tagging. The reconstruction strategy of the mentioned processes differs as the vertex topology is itself different. However, both the ISV and AMVF are aimed to provide a common software that would allow the reconstruction of different vertex topologies. Both have been implemented into the ATLAS Athena reconstruction software [43] and are based on object-orientated C++ with a Python configuration and running script. The version of reconstruction algorithms and tools, which are to be used for the particular situation, is entirely defined in the Python steering script.

4.2.1 Event Data Model and Athena Software

The implemented framework is based on a common Event Data Model (EDM), which allows the use of common software between online data processing and offline reconstruction. The EDM is a set of data classes storing relevant information to vertex reconstruction generally composed of Analysis Object Data (AOD), which is a summary of the reconstructed events and contains sufficient information for common analysis. Different vertex topologies will generally require different levels of detail to be stored in the EDM objects, which is achieved through using inheritance in the data model. This gives the vertex reconstruction tools access to EDM of reconstructed tracks as well as provides a unified way of retrieving and storing common vertex information shared amongst the different vertex topologies. As an example the tracks are fitted measurements on multiple surfaces, due to the inhomogeneous field when going from the Inner Detector and the solenoid magnet to the Muon Spectrometer and the toroid magnet system. The track is then a grouping of available information by the surfaces it is defined on. These tracks would have been an unnecessarily large object for vertex reconstruction, so a "TrackParticle" object is created from tracks. It stores only the relevant information like number of

hits of the parent track, perigee parameters ($\phi, d_0, z_0, \theta, q/p$) etc., necessary to do vertex reconstruction. Almost all EDM objects are stored in containers, which are of custom `DataVector< T >` type and store a variable number of elements per event. To avoid saving multiple instances of the same object, objects can point to each other, which is normally done with pointers and references. However, those are not easily persistified i.e. writable to disk. Those links are stored as `ElementLink< T >`, which stores two numbers: identification number of the container of the target object and the index of the target object in its container. Athena is the software framework in which all offline data processing is done. Although the software itself is written in C++, the scripting and configuration is written in Python. The framework provides a way to analyse the data provided by the ATLAS detector in the same manner they are recorded; on an event to event basis, independently of each other. The software is also responsible for loading the right metadata for the events we are reconstructing, which is the data about data, i.e. information about the trigger used, if the data is simulated, detector geometry etc. The input data is loaded to a central whiteboard, called `StoreGateSvc`, from which all the subsequent tools and algorithms may access it as well as through which new data is written to output files. The data is being analysed by several algorithms, which are executed in order defined by the main algorithm sequence called "top sequence". The algorithm sequence class `AthSequencer` is itself an algorithm to which subsequent algorithm sequences may be added, for example a filtering sequence, which only runs if the event passes the filtering algorithm. The algorithms do not depend on each other and may interact only via exchange of information, which is through `StoreGateSvc`. This independency of individual components of the software is realised by a component-based software engineering model. It implements an interface class through which the steering script asks the framework to provide an object that implements the interface. Algorithms for example are being called via the `IAlgorithm` interface class. If an algorithm is being requested, the Athena software takes care of loading and configuring the algorithm before the event processing begins (initialization), executing the code on event data once per event (execution) and possibly provides some summary or executed other pieces of code once the event processing has finished (finalization). The individual components report back on their success by returning a StatusCode object, for example a `StatusCode::SUCCESS`

if a tool within an algorithm has been initialised. Bits of code that are to be performed multiple times per event, such as track reconstruction, and can be called by multiple algorithms are combined into tools. Tools are also initialised and configured by the tool interface class, which takes the specific configuration from the python steering script. The algorithm then refers to `ToolHandle`, which makes the tool available to the algorithm for use. The tools and algorithms are grouped within the software to software packages, which may depend on each other. One such example would be the secondary vertex validation package containing an algorithm `InDetSecVertexTruthMatchAlgorithm` and three helper tools `InDetSecVertexTruthMatchTool`, `InDetSecVertexTruthMatchUtils` and `InDetSecVertexValidationHelper`.

4.2.2 Secondary Vertexing

The process for vertex finding and fitting may be split into four components:

- Track Selection
- Seed Finding
- Vertex Fitting
- Vertex Filtering

In some cases, the processes are intertwined, so both "finding-through-fitting" and "fitting-after-finding" approaches are possible. A prime example of the "finding-through-fitting" approach is the AMVF. The selected tracks are used to form a single secondary vertex, which is fitted with the adaptive multi-vertex fitter. The tracks not compatible with the vertex in the first iteration are used to form a new vertex seed, however the global track pool is used in the fit of the new vertex. A simultaneous fit of the two vertices is performed, if the vertices share any compatible tracks. With each iteration, more vertices compete with each other to gain more tracks with an annealing procedure preventing the fall to local minima. On the contrary, the Inclusive Secondary Vertex Finder is an example of a "fitting-after-finding" approach. The selected tracks are analysed for clusters of tracks, which are fitted to form a vertex. If a track is rejected from a vertex candidate it is never

used for fitting again, so the number of possible vertices produced is fully determined at the seeding stage.

4.2.2.1 Track Selection

Starting from all available tracks, vertices are found from pairs of tracks in an iterative manner. The high multiplicity of a typical collision makes considering all possible track combinations impractical, instead the tracks are firstly selected on quality and kinematic cuts. Two tools are called to do the track selection, `InDetTrackSelectionTool` and `InDetSecVxTrackSelectionTool`, responsible for a base selection of tracks and a specific selection for secondary vertexing respectively. The tools check whether a `xAOD::TrackParticle` in question passes the criteria provided in a cut family, each of which is composed of one or more `InDet::TrackCuts`. This is done by looping over the track's `InDet::TrackAccessors` and only retrieving the data it needs for the check. The cut selection can be set to a pre-defined level, through the 'CutLevel' property. The tools return an `asg::AcceptData` object, which is treated as a boolean in the vertexing tool, but it also provides detailed information about passed and failed cuts by organising the results into cut families. Specifically, the tracks are not allowed to be associated to any primary vertices and are required to have the transverse momentum above 1 GeV. To fine tune the selection to the physics search in consideration, the cuts on impact parameters, projections of the point of closest approach to origin or primary vertex in transverse (xy) and longitudinal (rz) planes, are adjustable. The setup procedure is inverted for the secondary vertexing to that for primary vertexing, meaning that while the search for primary vertices is based on impact parameters being smaller than a given value, only tracks with larger values enter the search for primary vertices.

4.2.2.2 Seed Finding

Selected tracks form a vector of global tracks, which initially also fills a vector of seeding tracks. The vector of seeding tracks is used to access the track parameters, which fill a vector that is fed into `IndexedCrossDistanceSeedFinder` along with the primary vertex x and y positions. The seed finder takes tracks two by two and uses the `SeedNewtonTrkDistanceFinder` to record the distance between the two tracks. This

is based on a Newton minimisation procedure, which finds a two dimensional point (position on first and second track) for which the derivatives of the distance is zero. The tool is initialised with two initial points to avoid maxima. They are obtained with the `Trk2dDistanceSeeder`, which finds the two points of minimal distance on the transverse plane and is analytically well defined. In case there are multiple such points, the tool chooses the ones closest in the z coordinate. Once the track to track distance has been found for all (N*(N-1)/2) combinations, where N is the number of tracks, the mode has to be calculated using the `Mode3dFromFsmw1dFinder`. It combines three 1 dimensional modes into one 3 dimensional mode. Data points are sorted according to their associated median distance and weight. The weight associated to a given distance between two data points is the sum of the weights of the data points. Starting from the top, the distances' weights are added until half of the total sum of weights is exceeded. This is considered as the weighted average distance and the data points are sorted by this quantity. The final estimate is now the weighted mean of the data points, which is returned by the seed finder as a `Amg::Vector3D`.

4.2.2.3 Vertex Fitting

Before the vertex is fit, tracks compatible to the seed position are selected. For the case of AMVF, the global vector of tracks is used, however for the ISV only tracks remaining in the vector of seeding tracks are used. For each track in the selected vector of tracks the `ImpactPoint3dEstimator` is used to construct a plane intersecting the track at the point of closest approach with the track being orthogonal to the plane and the seed position placed in the centre of the plane. This returns a track to vertex minimum distance. If this distance is smaller than a user defined variable, then the track is deemed compatible with the seeding position and is added to a vector of tracks to fit.

ISV and the Adaptive Vertex Fitter

Tracks entering the vertex fit are first linearised with the `LinearizedTrackFactory` tool to circumvent the potential problems one may encounter with the tracks metric properties. The idea is to represent the tracks as simple points in Euclidean 3D space and ease the jobs of the pattern recognition algorithms. The measurement equation, i.e. the dependance of

the track parameters on the vertex position and track momentum at vertex is linearised at the vicinity of the user-provided linearisation point, in this case the seed position. The measurement equation is linearised as follows:

$$q_k = A_k * (x_k - x_{k_0}) + B_k * (p_k - p_{k_0}) + c_k, \tag{4.1}$$

where q_k are the parameters at perigee nearest to the linearisation point, x_k is the vertex position, p_k the track momentum at vertex and c_k the constant term of expansion. A_k and B_k are the matrices containing derivatives, the position Jacobian and momentum Jacobian respectively. The vertex fitting procedure is based on the typical Kalman filtering approach, where the inverse of the track parameters covariance matrices are down-weighted according to the probability that the track is compatible to the vertex. This smoothly rejects any outlier tracks not belonging to the vertex. The weight w_i is a function of the distance of the track i from the current vertex, measured by the chi-square χ_i^2:

$$w_i(\chi_i^2) = \frac{\exp(-\chi_i^2/2T)}{\exp(-\chi_i^2/2T) + \exp(-\chi_c^2/2T)}, \chi_i^2 = r_{i|n}^T G_i r_{i|n}, \tag{4.2}$$

where T is the temperature parameter , $r_{i|n}$ represent the smoothed residuals, $G_i = V_i^{-1}$, where V_i is the covariance matrix, and χ_c^2 sets the threshold where the weight is equal to 0.5. Beyond this cut, the tracks is considered to be an outlier. The `KalmanVertexUpdator` is responsible for adding or removing the tracks from the vertex estimate, whereas the `SequentialVertexSmoother` updates the tracks with the knowledge of the new reconstructed vertex. The estimation of vertex position during the initial iterations is not particularly good, so an annealing technique is implemented. This softens the rejection of outliers at the beginning and hardens it towards the end of the fit, for which the `AnnealingMaker` tool is responsible for. This exploits a physics analogy for the problem of finding clusters in data sets. The energy of the data set is interpreted as a thermodynamical system and lowered with every phase transition, where the initial centre splits along the principal component of the data associated with the initial centre of mass of the data points [44]. The temperature T modifies the shape of the w_i function, where at low temperature, the weight is close to 1 for $\chi_i^2 \leq \chi_c^2$ and close to 0 for $\chi_i^2 > \chi_c^2$, with a sharp drop at $\chi_i^2 = \chi_c^2$ [45]. The full procedure for the vertex fit can be summarised in these steps:

- set initial counter of steps — to zero, set initial tracks covariance matrices, set the initial vertex estimate as the seed position, choose a threshold χ^2_c and T
- for each track, compute the smoothed residuals, the χ^2-statistic χ^2_i using the vertex estimate, the covariance matrices and weights w_i at step I
- increase the iteration counter I by 1 and set for each track i, the covariance matrices $V_i^I = v_i/w_i$
- set the temperature T_I according to the chosen annealing schedule and go back to the second step
- after reaching the final temperature, iterate until convergence

The Adaptive Vertex Fitter returns a new vertex with tracks attached in a vector of `Trk::VxTrackAtVertex` decorator. The new vertex undergoes an initial check to ensure a good vertex is found. The vertex is rejected after fit, if n_{dof} is less or equal 0 or number of tightly bound tracks (weight of track at vertex > 0.001) is less than two, otherwise a good vertex is written into the output container. If the vertex is deemed good, then the tracks attached to the vertex are removed from the seeding list, from which a new seed and vertex are found and fit. Once there are no more tracks left in the seeding list or the new seed position has no more compatible tracks in the seeding list of tracks, the vertex search is concluded.

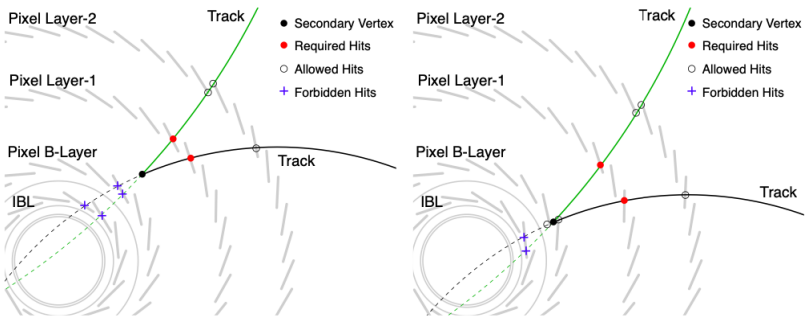

Figure 4.2: The schematic shows as example a transverse view of the pixel detector in the barrel region. The tracks of the reconstructed secondary vertex must not have hits on the layers within the vertex radius [46].

ISV and vertex cleaning

The ISV implements another interesting feature, which is vertex robbing. This involves a loop over all vertices and all tracks at vertices to check wether a track from vertex A could be more compatible to vertex B. In case such a track is found, the track is added to vertex B, which is then re-fitted with the new track. Vertex A is marked for robbing, where in the end the track is removed and the vertex is again re-fit. The ISV employs a level system for additional vertex cleaning: at this point a good vertex is found and fit, labelled as secondary and written into the container if the filter level is set to 0. However, additional checks are used to help eliminate potential fake vertices:

1. Hits pattern
2. Minimum distance between vertices
3. Vertex momentum relative to its direction
4. V^0 removal

Level 0 The first filter tries to ensure tracks used in vertex forming have hits in Inner Detector layers at radii larger than the vertex position, but have no hits in layers at smaller radii, since tracks typically travel through the tracker. This is schematically shown in Figure 4.2. For a track tightly bound to a vertex, the hit pattern is checked against the vertex position and removed from vertex in case the condition is not satisfied. For each vertex, the number of removed tracks and their p_T is checked with Equation 4.3.

$$m_{hif} = 0.4 \cdot \frac{n_{\text{removed}}}{n_{\text{tightly bound}}} + 0.6 \cdot \frac{p_T^{\text{removed}}}{p_T^{\text{total}}}. \tag{4.3}$$

If m_{hif} exceeds the value of 0.8, then the vertex is rejected and for other non-zero values vertex grooming is tried. Grooming is a process of removing tracks with hits in layers below the secondary vertex and attempting to re-fit the vertex. In case the removal of tracks leaves the vertex with less than two good tracks or the re-fitting procedure yields a bad vertex, the vertex is again rejected.

Level 1 The ISV allows an additional option, which is vertex splitting. It can be turned on by the user and is defined by a vertex split fraction. The decision procedure is outlined

in Table 4.1. The split vertex option was added to ensure a single high track multiplicity vertex is not reconstructed from two vertices in (user defined) close proximity, however no tool has yet been implemented to do the actual vertex splitting afterwards.

Number of available tracks	Vertexing option	Tracks used in fit
2	/	all
> 2	/	tracks with distance to seed $<$ significance cut
$\leqslant 4\times$ (split vertex fraction)	split vertices	all
$> 4\times$ (split vertex fraction)	split vertices	all (vertex marked for splitting)

Table 4.1: Decision process in ISV for selecting the number of tracks entering the vertex fit

Level 2 The vertex momentum and its direction is checked with respect to the primary vertex position by calculating the dot product of normalised vertex momentum vector and vector of positional difference between the primary and secondary vertex, where the former is calculated with a vector sum of all tracks momenta. If the dot product is smaller than a primary vertex reference input, the vertex is rejected.

Level 4 Last, the vertices coming from decays of particles in the standard model are rejected by conducting a V^0 check. These are charge neutral particles, most frequently Λ^0, $\overline{\Lambda^0}$, K_S^0 and γ. The signature we are looking for is a decay to two oppositely charged particles, not mediated by the weak interaction, balanced in momentum with sufficient energy to, for example, come from a Λ^0 and decayed to a $\pi^+\pi^-$ pair. Vertices that pass the criteria that describe any of those decays are rejected. Once all of these procedures are done, the ISV yields a container of vertices, where the good ones are marked as `xAOD::VxType::SecVtx`. Vertices that failed in any stage of checks are not deleted, but marked as `xAOD::VxType::KinkVtx`, `xAOD::VxType::NoVtx`, depending on the stage and process it failed at.

AMVF and Adaptive Multi-Vertex Fitter

To the point of entering the vertex fit, the AMVF is equivalent to the ISV. The seed is found from the seeding vector of tracks, however the compatible tracks to the new seed

position are always chosen from the global list of tracks. A new vertex with an initial position of the seed is created and decorated. In order to aid the multi-vertex fitting, the tracks are decorated with a link to the vertex. So each track has a vector of links to vertex and each vertex a vector of tracks at vertex. Now the vertex enters into the Adaptive Multi-Vertex Fitter, where the linearisation and compatibility estimations are the same as in the Adaptive Vertex Fitter. At each iteration in the Adaptive Multi-Vertex Fitter all of the vertices are fit using the tracks in their respective decorations, however the tracks that are shared among multiple vertices get their weights dynamically updated, so each track has weights at multiple vertices. The deterministic annealing ensures that the tracks are eventually assigned to the vertex they are most compatible with. The Adaptive Multi-Vertex fitter again returns a new vertex with a list of tracks most probably belonging to the vertex. An attempt is made to remove those tracks from the seeding list, if they are on it. In order for the next iteration to find a different seed position, cases where no track used in the fit was on the seeding list are resolved by removing a single track that is closest to the old seed position. Compared to the ISV, the AMVF does not yet contain any additional vertex rejection mechanism, apart from the 'good vertex' check. The two finders are schematically compared in Figure 4.3.

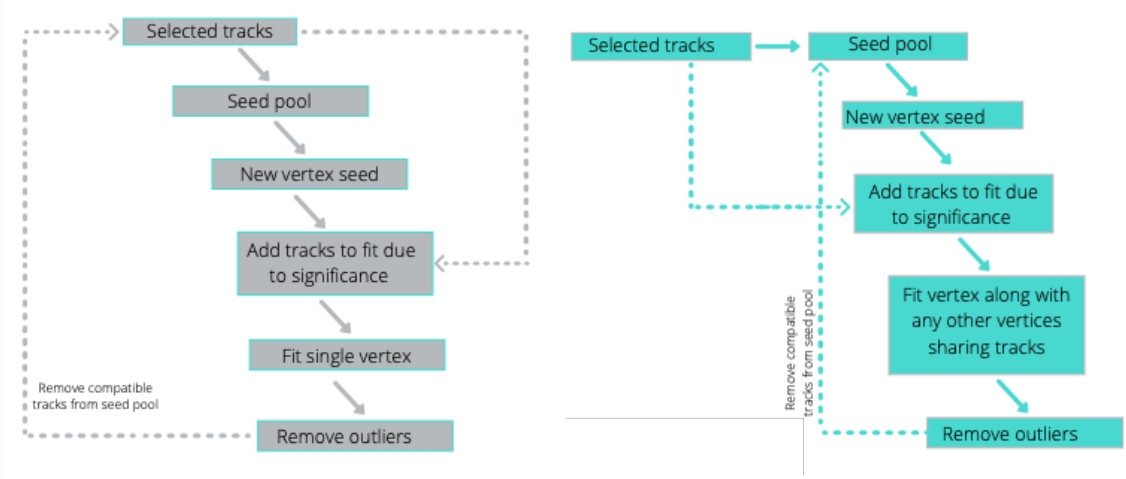

Figure 4.3: Schematic representation of the inclusive and adaptive multi-vertex finding method, shown left and right respectively.

4.3 Secondary Vertex Validation Package

4.3.1 Truth Matching

In order to test the performance of the various secondary vertex finders, a new algorithm was developed. The algorithm is applicable to all reconstructed secondary vertices regardless of the MC sample used. For each vertex finder output the algorithm associates the reconstructed to the vertices in the MC event record by Truth Matching. The efficiency of the vertex reconstruction is then assessed based on the ability to reconstruct a generator-level (truth) vertex. The algorithm works in three simple stages: initial checks, vertex labelling and producing efficiency plots.

The first step is to ensure the secondary vertex finder output can be used in an analysis starting with a vertex label check. Part of the finding procedure is also fake vertex rejection, where the rejected vertices do not satisfy one or several of the quality checks that the finder conducts. If they are rejected, but nonetheless written into output, they should be marked appropriately with either a `VxType::KinkVtx`, `VxType::NoVtx` or `VxType::V0Vtx` type. Vertices not passing this initial check are labelled `VxType::NoType`. In primary vertex finding, the offline beam spot can be used as a constraint in the fit of the vertex position. The beam spot is the luminous regions inside the detector where collisions occur, its shape and position is determined by the LHC beams. Offline beam spot measurements are performed before bulk reconstruction, and are uploaded as conditions data for use in offline algorithms like vertex finders [47]. The Inclusive Secondary vertex package was directly copied from the primary vertex package, including the beam constraint option, and hence leaving the option to fit a vertex with a single compatible track and the beam constraint. This option was since removed and an additional check was placed in the validation package ensuring that the vertex has at least two attached tracks and information about the tracks weights, which come from the vertex fit. The number of attached tracks should match the length of the track weight vector. A vertex failing to comply with these conditions is labelled as MissingInfo.

Vertices not yet labelled enter into the Truth Matching procedure, schematically shown in Figure 4.4. Similarly to the truth matching procedure for primary vertices, the reconstructed vertices are classified by first assorting the vertex tracks based on

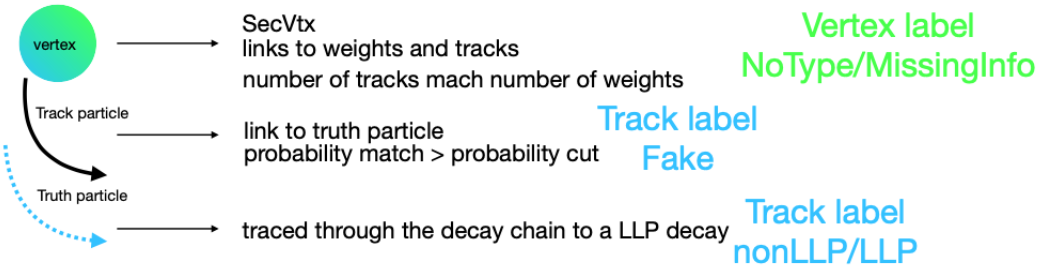

Figure 4.4: Schematic representation of labelling reconstructed vertices and its tracks.

their origin. However, for the primary vertex, you are interested in finding the highest weight match to the hard scatter interaction, where a simple track to truth validity check is sufficient. In secondary vertex reconstruction, the main interest is not precision of reconstructed vertex position, but correctly tagging the the vertices coming from desired decays. The metric for evaluating the performance of individual algorithms is purity of the reconstructed vertices - the fractions of tracks used for reconstructing the vertex that came from the desired decay. The tracks' origin has to therefore be traced through the decay cascade at truth level and traced to the desired decay. To ensure the vertex label is justified, the tracks are required to pass a truth validity check. Each charged particle traversing through the detector produces hits in the inner detector. The hits are used in track reconstruction to produce the particle path - a reconstructed track. The reconstructed tracks (detector level) may not represent the true trajectory of the particle at generator level - the truth track. The reconstructed track is linked to a truth particle with which it shares the most detector hits and a probability match, which describes the number of hits used in the track reconstruction and the total number of hits coming from the truth particle. The truth validity check for reconstructed tracks used in the vertex fit consists of checking the reconstructed track is linked to a truth track and that the probability match is equal or greater than 0.5. Reconstructed tracks that do not pass this criteria are labelled as fake. Reconstructed tracks unsuccessfully traced through truth tracks to a desired decay are labelled *nonLLP*, which is solely due to the fact that a long-lived particle (LLP) sample was used as the validation sample. In the last case where the reconstructed track is successfully traced to a desired decay, the reconstructed track is labelled as *LLP* and is also marked with the truth vertex ID. The transverse momentum

of reconstructed tracks sharing the same label is summed and compared to the transverse momentum sum of all reconstructed tracks associated with the vertex. In case more than 0.5 of the sum of tracks momentum is coming from fake tracks, then the vertex is labelled as *Fake*. The same deduction follows for *nonLLP* tracks and *nonLLP* vertices. In the last case, where the majority contribution comes from LLP decays, the vertex can be labelled as one of three options: *Clean*, *Split* or *Merged*. For each truth vertex ID, a match score, defined in Equation 4.4, is calculated, which is the ratio of sum of reconstructed tracks transverse momentum sharing the same truth vertex ID label and sum of all reconstructed tracks transverse momentum at vertex.

$$\text{match score}(v, l) = \frac{\sum_{i \in \text{trk} \in v} (p_T^{(i)} | \text{descendant of decay } l)}{\sum_{i \in \text{trk} \in v} (p_T^{(i)})} \tag{4.4}$$

If the reconstructed tracks matched to the desired decay also share the truth vertex ID, meaning they are all traced to the same truth level decay vertex, then the reconstructed vertex is considered *Clean* and has only one match score number. If on the other hand the reconstructed tracks do not share the truth vertex ID, then the reconstructed vertex is representing multiple desired decays and is labelled as *Merged* with multiple match assorted in lowering order. The last option is that multiple reconstructed vertices are matched to the same truth vertex, in this case all of the reconstructed vertices are labelled as *Split*.

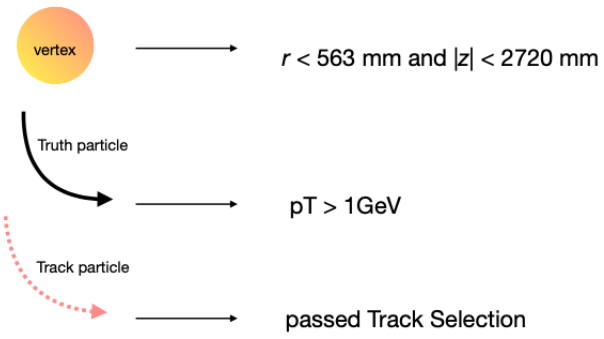

Figure 4.5: Schematic representation of truth vertex label dependancy.

Once all of the reconstructed vertices are labelled, the algorithm continues to label the truth vertices, which is schematically shown in Figure 4.5. The algorithm finds all desired

truth decay vertices in the MC event record based on the decaying particle PDG ID. The vertices are then checked based on their position and composition of their decay chain. The first check ensures the vertex is within the tracking volume of the inner detector, the later ensures the vertex could be seeded and the tracks have a large enough momentum in order to be reconstructed by the tracking algorithm. They are then labelled as follows:

- If the vertex has at least two truth particles in the decay chain with transverse momentum larger than 1 GeV, the vertex is considered *Inclusive*
- If the vertex is *Inclusive* and located in the inner detector region, then it is labelled as *Reconstructable*
- If the vertex is *Reconstructable* and the decay contains at least two reconstructable tracks that passed the tracking selection, then the vertex is labelled *Seeded*
- If a reconstructed vertex is matched to the truth vertex with a match score > 0.5, then the vertex is considered *Reconstructed* or *Matched*

To attempt to decouple the vertexing performance from the track reconstruction performance, the efficiency is factorised in independent terms, as defined in Equation 4.5:

- The acceptance of MC truth vertices, denoted as $\mathscr{A}_{\overrightarrow{x}}$ in given a given local volume δV at position $\overrightarrow{x}$ is defined as the ratio of number of reconstructable truth vertices and inclusive truth vertices. This would be the efficiency of an ideal performance of both tracking and vertexing algorithms and should only depend on the MC sample used.
- Total reconstruction efficiency, $\varepsilon^{tot}_{\overrightarrow{x}}$, is given as a ratio of number of truth vertices matched to a reconstructed vertex with a match score of at least 0.5 and number of reconstructable truth vertices.
- Seeding efficiency, $\varepsilon^{seed}_{\overrightarrow{x}}$, is defined as the ratio of number of truth vertices labelled as seeded and number of reconstructable truth vertices. This accounts for the track selection efficiency and served as a cross check when implementing the track selection tool into individual vertex finders

- Algorithmic efficiency, $\varepsilon^{alg}_{\overrightarrow{x}}$, attempts to decouple the vertexing efficiency from the tracking efficiency and is defined as the ratio of total efficiency and MC acceptance
- Core efficiency, $\varepsilon^{core}_{\overrightarrow{x}}$, is defined as the ratio of algorithmic efficiency and seeding efficiency. It probes the success rate of the vertex fitting when constituent tracks are provided.

Therefore the reconstruction efficiency is given by:

$$\varepsilon^{tot}_{\overrightarrow{x}} = \mathscr{A}_{\overrightarrow{x}} \cdot \varepsilon^{alg}_{\overrightarrow{x}} = \mathscr{A}_{\overrightarrow{x}} \cdot \varepsilon^{seed}_{\overrightarrow{x}} \cdot \varepsilon^{core}_{\overrightarrow{x}} \tag{4.5}$$

4.4 Performance Analysis: Established Secondary Vertex Finders

The Inclusive Secondary Vertex Finder has recently been implemented as an alternative method to VKalVrt [48] for reconstructing secondary decay vertices and has now been joined by an alternative Adaptive Multi Secondary Vertex Finder. Neither ISV or the new AMSVF have been validated before this point. The initial testing sample was 1000 generated events of the gluino decay. In this model, the supersymmetric partner of the gluon, the gluino ($\widetilde{g}$), is kinematically accessible at LHC energies while the SUSY partner particles of the quarks, the squarks ($\widetilde{q}$), have masses that are several orders of magnitude larger [49]. Figure below shows a pair-production of gluinos decaying to two quarks and the lightest supersymmetric particle (LSP), assumed to be the lightest neutralino ($\widetilde{\chi}^1_0$).

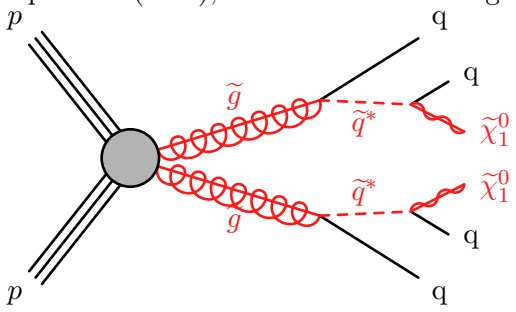

Figure 4.6: Diagram showing pair-production of gluinos decaying through $\widetilde{g} \to q\widetilde{q}\widetilde{\chi}^1_0$ via a virtual squark $\widetilde{q}^*$.

A comparison of the ISV and AMVF to the established and frequently used secondary vertex algorithms available in the Athena software was performed. This included

integrating the tracking tool and employing the same track selection into the broadly used Vertex Sec Inclusive, VKalVrt and its recent upgrade newVSI. Figure 4.7 displays a comparison of how an inconsistent track selection would show in the seed efficiency, since that strongly depends on track reconstruction efficiency. The acceptance of this signal model is also displayed in Figure 4.7, which serves as an idealistic benchmark for reconstruction efficiency. A plot comparing the number of reconstructed vertices with

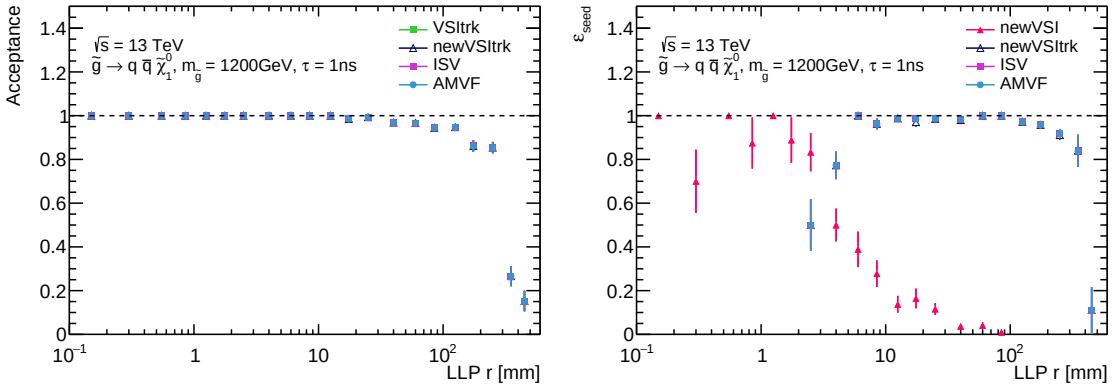

Figure 4.7: Acceptance of truth vertices and seed efficiency as a function of vertex position, left and right respectively. ISV denotes the ISV algorithm with the vertex filter level set to 5, AMVF is the adapative multi-vertex fitter, VSI is the commonly used Vertex Sec Inclusive, newVSI denotes the updated VSI algorithm used with its default track selection, whereas newVSItrk denotes a common track selection was employed.

their corresponding labels is showed in Figure 4.8. The AMVF shows improvement in the number of reconstructed clean vertices and the suppression of reconstructing multiple vertices from a single high-multiplicity decay, but shows an increase in the number of reconstructed *Fake* and *nonLLP* vertices. From Figure 4.9 it can be seen that there is a peak at 2 tracks in the distribution of number of tracks at vertex, which could be interpreted as an indication that the algorithm could greatly benefit from V^0 removal. On the right hand side of Figure 4.9 it can be seen that although the majority of vertices are reconstructed before the first material layer, the peaks in number of reconstructed vertices in material layers is significant and a material map veto should be employed.

The core efficiency reflects the success rate of the vertex fitting method when the tracks originating at truth vertex are provided. Figure 4.10, left-hand side, displays a cutoff at $r = 2$ mm, which comes from the track selection requirement of $|d_0| > 2$ mm.

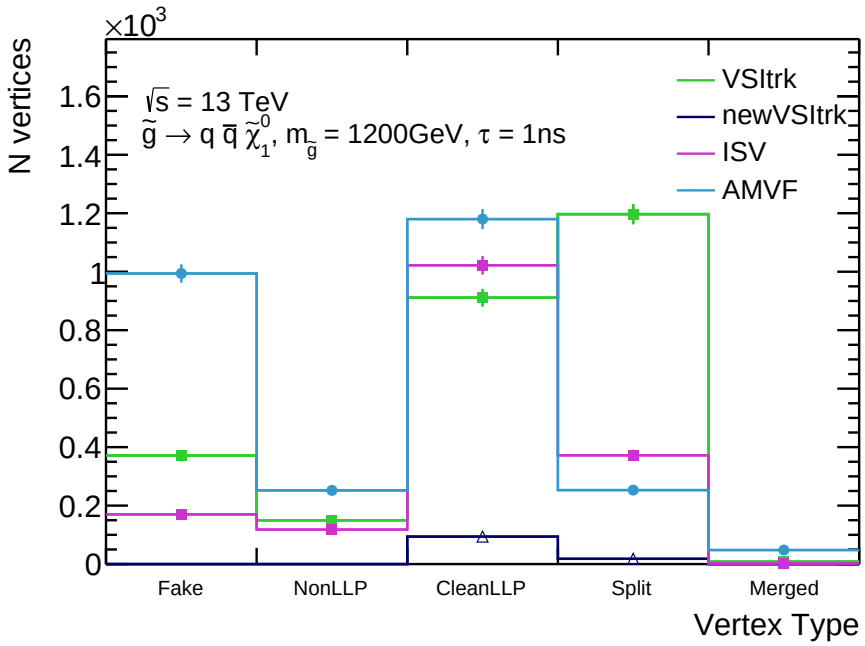

Figure 4.8: Number of reconstructed vertices of each type, where 'VSI' and 'newVSI' denote the Vertex Secondary Inclusive algorithm; the later denoting the latest update and the 'trk' denotes the track selection tool in VSI was replaced to match the one used in ISV and AMVF.

Above the cutoff, the efficiency degrades due to two effects, the first being the degradation of track reconstruction efficiency as a function of radius, resulting in a smaller number of reconstructed tracks at higher radii and consequently the lowering of the probability of reconstructing the vertex. Additionally, at larger radii, the boost of a given LLP decay is higher, resulting in a collimation of the decay products and a more difficult vertex topology to reconstruct. The total vertex reconstruction efficiency, which includes the track reconstruction efficiency, the track selection efficiency and the pure vertex reconstruction efficiency is displayed in Figure 4.10 on the right. The performance of AMVF appears to surpass that of the ISV and is compatible to that of currently broadly used VSI. Statistically however it is hard to tell based on a mere 1000 events and a single tested vertex topology. Future analysis would greatly benefit from a single white paper, which describes the various vertex fitters currently available, their fitting and finding procedures, and their comparisons on a few benchmark signal models.

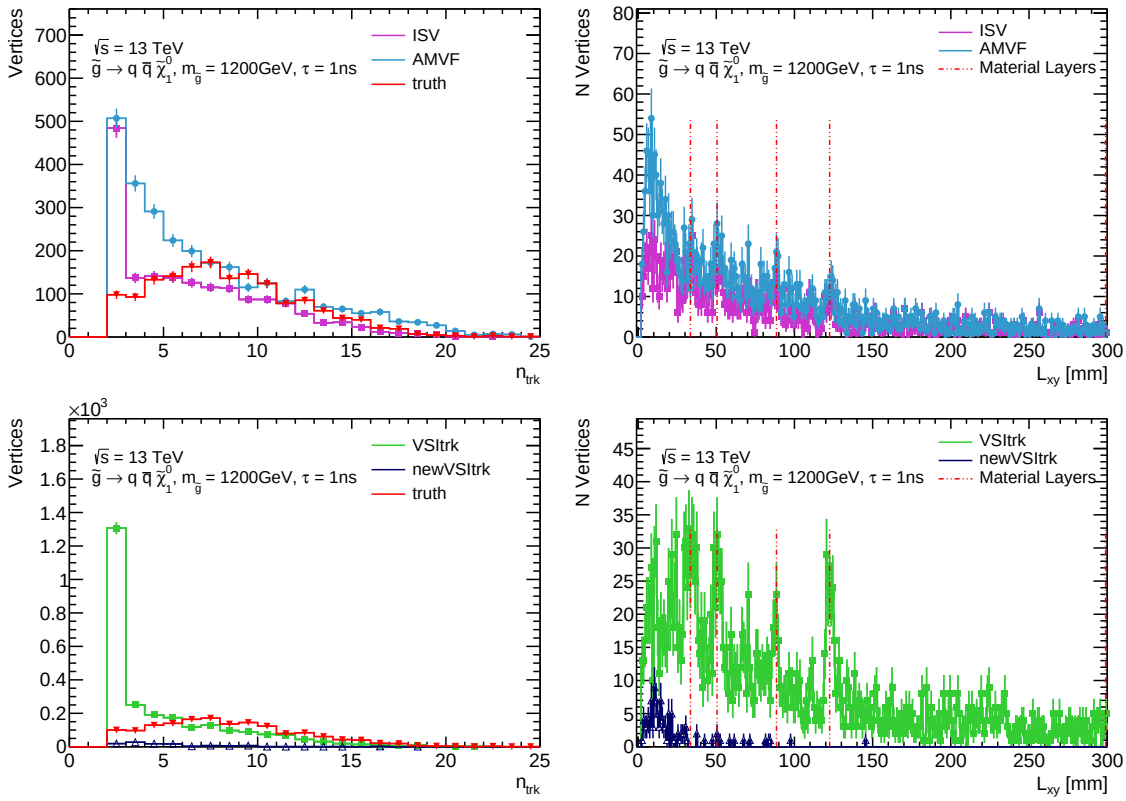

Figure 4.9: Number of tracks at vertex (left) and radial position of reconstructed vertices (right) reconstructed from 1000 events of a simulated BSM gluino sample using ISV and MAVF (top) or VSI and newVSI (bottom) algorithms. The label 'truth' on the left plot is used to label the tracks at generator (truth) level with sufficient momenta to be reconstructed.

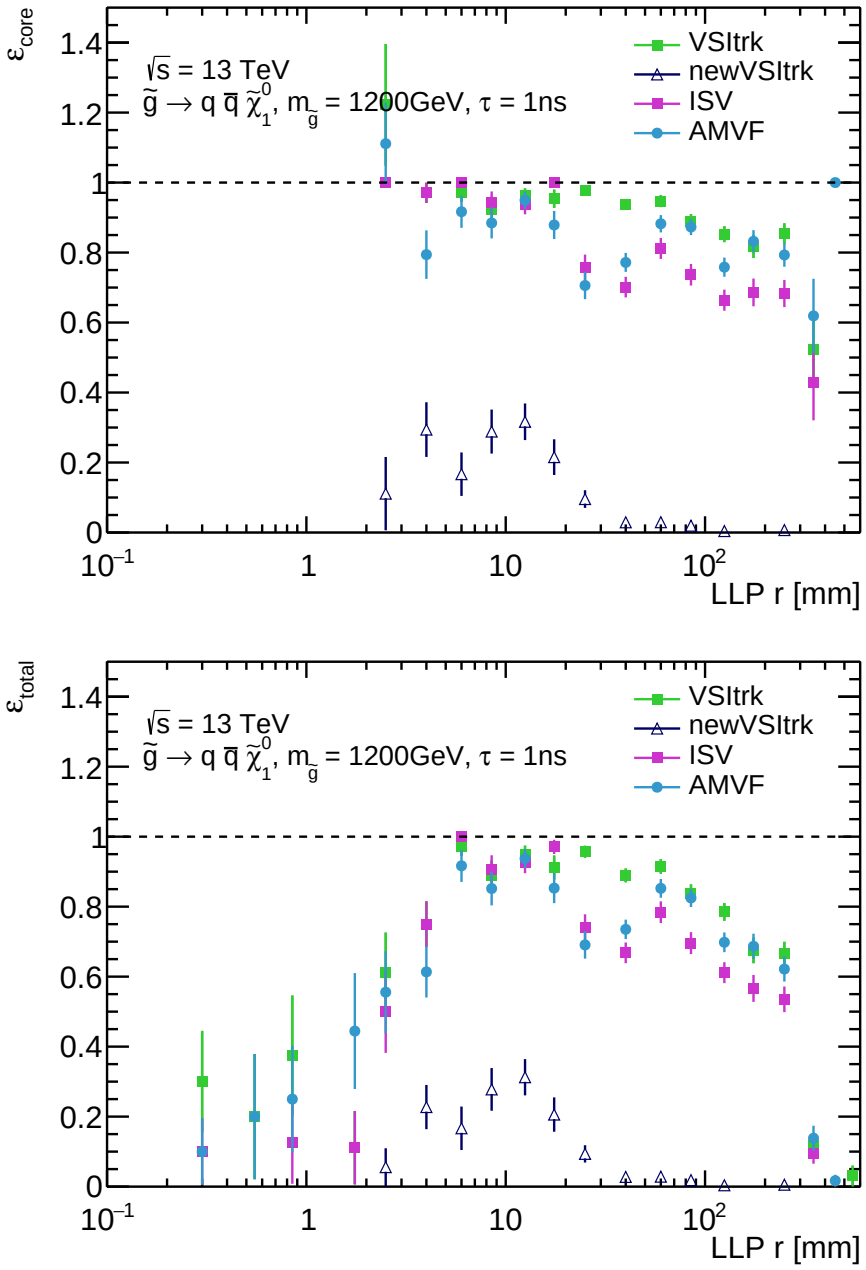

Figure 4.10: Core (top) and total (bottom) reconstruction efficiency as a function of radial position of the reconstructed vertices. Core efficiency describes the success rate of vertex fitting when tracks from the decay are provided, whereas the total reconstruction efficiency depends on the core efficiency, seeding efficiency and the detector acceptance of the signal sample.

Chapter 5

Long Lived Particles

The majority of new physics searches conducted with the ATLAS detector focus on "prompt" particles, which are characterised by their decay shortly after creation. The decay products of these particles typically point back to the collision point, and the distance between their creation and decay is either smaller than or comparable to the spatial resolution of the detector. Conversely, particles are classified as "detector stable" when they typically decay outside of the detector volume. Between these two extremes lies a previously less explored domain known as long-lived particles (LLPs). Long-lived particles are produced and exist for a certain duration before eventually decaying within the detector. It's worth noting that the concept of long-lived particles is not exclusive to BSM physics. In the ATLAS experiment, LLPs are generally considered those with a lifetime exceeding 1.5 ps (longer than the average lifetime of a b-hadron) and a travel distance exceeding 1 millimeter before decay. Figure 5.1 illustrates the Standard Model particles in the metastable region, which lies between the detector's prompt and detector-stable categories. Prompt searches typically focus on identifying neutral stable particles, which are potential candidates for dark matter. These searches infer the presence of such particles by calculating MET from the prompt particles detected in the event. In contrast, LLP searches employ different strategies. They either directly search for the signature of the LLP itself or seek a displaced signature arising from the decay products of these particles. One significant advantage of LLP searches is exactly the limited presence of SM background, making them well-suited for probing signatures with very small cross-sections. However, due to the scarcity of long-lived particles in the SM, reconstructing these particles

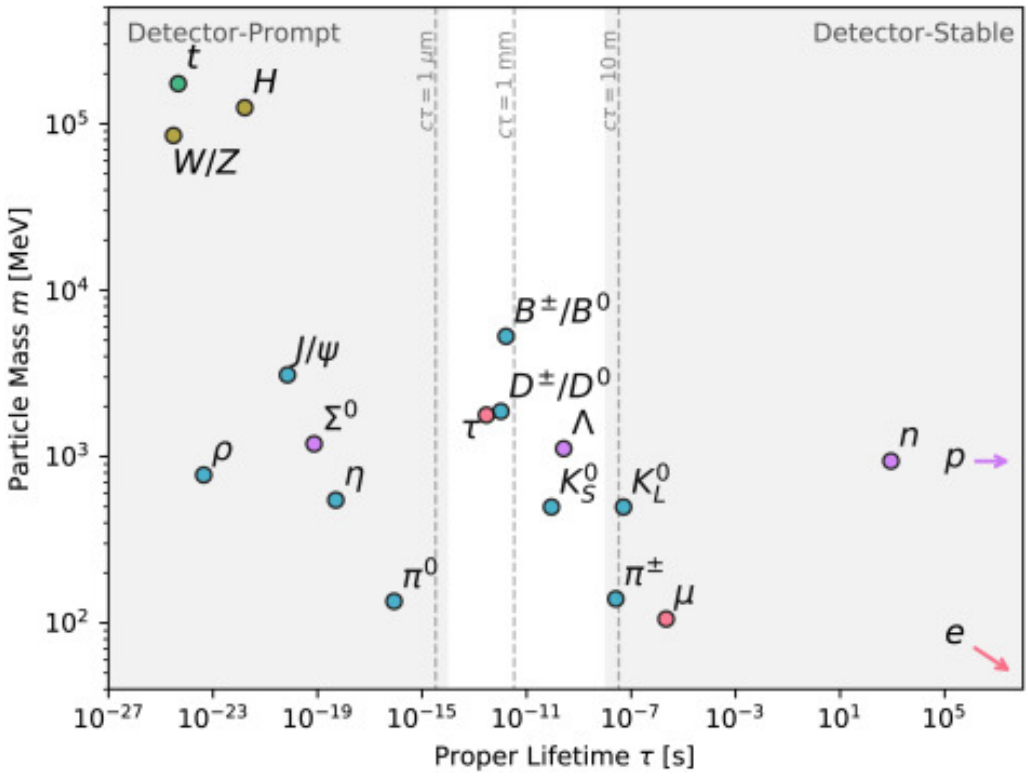

Figure 5.1: Distribution of mass and lifetimes for a number of SM particles. The shaded regions represent detector prompt, on the left, and detector stable, on the right, regions [50].

and their decay processes presents a technical challenge for conventional reconstruction algorithms, which were designed with the SM in mind. The under-exploration of this phase space has been significantly influenced by the absence of background contributions coming from the SM processes. Instead, fake signals and mis-reconstruction play a substantial role in this scenario. This chapter aims to provide an overview of key concepts employed in LLP searches at colliders and to review prior research that has already delved into this uncharted territory.

5.1 Lifetime

While theory cannot predict the exact lifetime of an individual particle, it can provide us with the decay rate, Γ. The decay rate represents the probability per unit time that a particular particle will undergo decay. Typically, a particle can decay through multiple

distinct channels, and the total decay rate is the sum of the rates for all possible decay channels:

$$\Gamma_{total} = \sum_i \Gamma_i. \tag{5.1}$$

The decay rate, or width, for each process can be calculated by:

$$\Gamma_i = \frac{1}{2m} \int |\mathcal{M}|^2 d\Phi, \tag{5.2}$$

where m is the mass of the particle that is decaying, $d\Phi$ is the phase space of the decay and $\mathcal{M}$ is the matrix element of the particle's decay into its decay products. The matrix element describes the particular decay channel from the initial state to the final state. If a particle can decay in multiple channels, the width of each decay is summed into the particle's *total width*. The branching ratio represents the probability that a particle will decay to a specific channel and is given by:

$$\mathrm{Br}_i = \frac{\Gamma_i}{\Gamma_{total}} \tag{5.3}$$

Given a sample of N_0 identical particles at time $t = 0$, then the number of particles decreases exponentially as:

$$N(t) = N_0 e^{-t\Gamma}. \tag{5.4}$$

A particles's lifetime, τ, is then defined as the time it takes e^{-1} of the initial number of particles to decay:

$$\tau = \frac{1}{\Gamma}. \tag{5.5}$$

Consequently, the particle's lifetime is determined by its decay width. For a particle to have a long lifetime, either the matrix element of the decay process or the available phase space for the decay must be restricted. Small matrix elements can result from weak couplings to final-state particles or involvement of highly off-shell intermediate states. Similarly, limited decay phase space can arise in cases where the final-state particles have nearly degenerate masses. It's worth noting that both small matrix elements and constrained decay phase space are characteristics shared by both SM and BSM theories.

5.2 Collider Searches

In the past, particle physics searches primarily concentrated on heavy particles with relatively short lifetimes. However, there has been a notable shift in focus towards long-lived particles, regardless of whether they are heavy or light. Long-lived particles are increasingly recognised as potentially pivotal in the quest to advance beyond the Standard Model. Many of these particle signatures exhibit minimal or zero background from the Standard Model, making them highly promising for discovery. These long-lived particles can manifest in various detector signatures, as illustrated by some examples in Figure 5.2. However, the full extent of their discovery potential has yet to be realised. Numerous new signatures for future LHC runs within existing experiments, as well as in the context of entirely new experiments designed to probe long-lived particles, are currently under consideration. The various search efforts conducted by ATLAS and CMS all share a common objective: to either directly detect the long-lived particle itself or indirectly observe its decay products. Only some of the searches, those relevant for this model and analysis formulation, are presented below.

Direct Searches

Long-lived particles can be massive, possess an electric charge and move at relatively low speeds. These slower-moving particles become detectable as they traverse through the detector, engaging in interactions with the detector material. However, the distinctive tracks they leave behind are discernible due to their exceptionally high ionisation loss. In other searches, the focus was on long-lived particles that decay into unconventional track signatures, such as disappearing or kinked tracks. These signatures typically involve prompt tracks. Such searches have a rich historical background and also mark the start of the investigation related to the model addressed in this thesis, described more in Chapter 5.3.

Indirect Searches

If the particle travels a significant amount of time, 1 ps for the ATLAS detector, before decaying to reconstructable objects inside the detector volume, the decay vertex can often be reconstructed. Since it is removed from the primary vertex, where the particle was

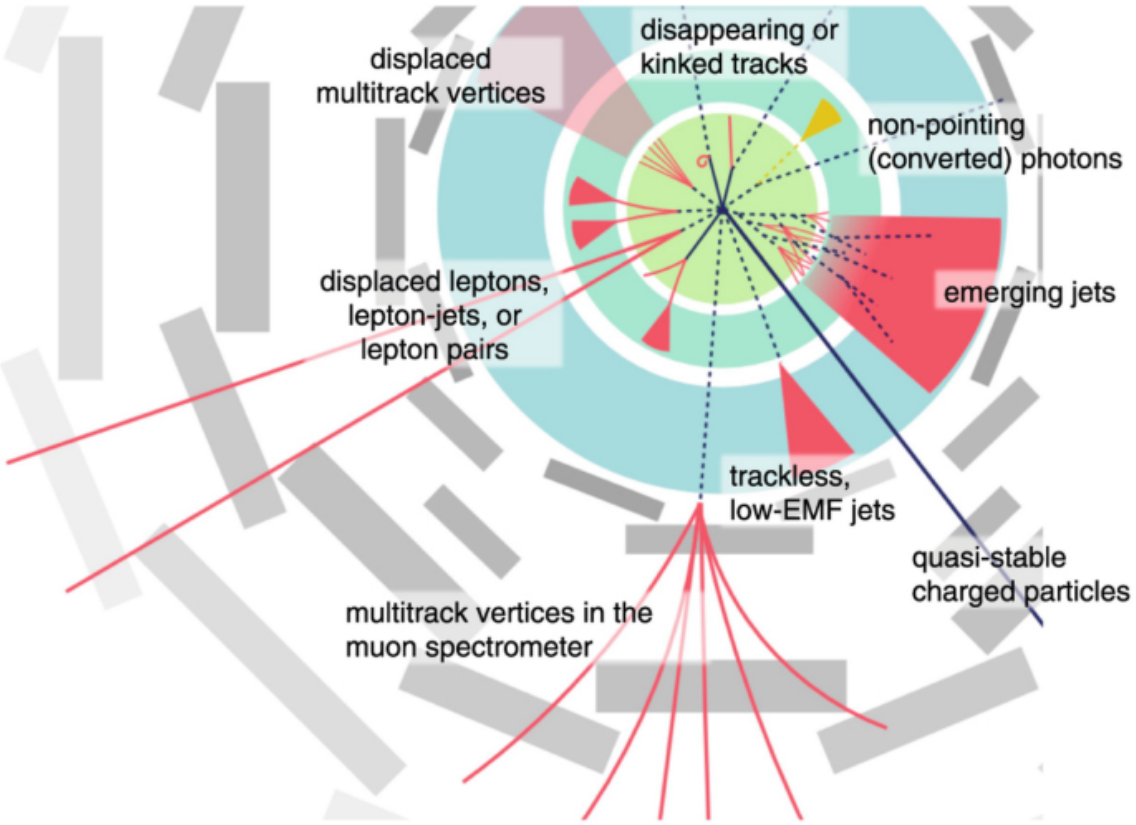

Figure 5.2: A depiction of some of the LLP signatures in the ATLAS detector. [51]

created, it is called a displaced vertex. The lifetime of the particle can be directly inferred from the separation between the primary and displaced vertex. Numerous ATLAS searches involve the reconstruction of displaced vertices either from or in conjunction with other physical entities like jets, leptons, or MET. However, many prior searches necessitated a secondary vertex and lacked sensitivity to $\tilde{l}$ production. In this analysis, the two displaced l particles, resulting from pair-produced $\tilde{l}$, do not share the same origin in their decay process and thus are not associated to the same secondary vertex. Since the only other particles generated in the decay chain, the $\tilde{G}$ and ν, are uncharged, they do not leave any tracks. Consequently, it is impossible to reconstruct a displaced vertex in the event and moreover, the leptons do not point back to the primary vertex. This search imposes no requirements for other objects to be present in the event, nor does it place restrictions on the amount of MET, rendering it model-independent for future reinterpretations.

5.3 Past Searches

A gap in the exploration of displaced lepton signatures has previously left an uncharted phase space for LHC-accessible SUSY. Since the slepton's lifetime is related to the SUSY breaking scale, which remains uncertain within this framework, and the substantial difference in background sources as the particle's lifetime varies, multiple analyses have been subjected to reinterpretation as well as new ones have been devised to address narrower ranges of lifetime. This chapter is dedicated to examining the previously established stringent constraints, recent findings, and the specific region of phase space that this analysis investigates.

5.3.1 LEP and Reinterpretation of Run 1 Results

LEP

The LEP experiments, including OPAL, L3, ALEPH, and DELPHI, conducted searches for long-lived slepton signatures originating from the process $e^+e^- \to \tilde{l}_R^+\tilde{l}_R^-$. By combining their results, these experiments excluded the existence of super partners for right-handed muons and electrons, regardless of their lifetime, for masses below 93.3 GeV and 65.8 GeV, respectively. Notably, the OPAL experiment, in particular, established the most stringent constraints on all lifetimes of $\tilde{\tau}_1$, which is a combination of super partners of both right- and left-handed τ leptons, for masses less than 87.6 GeV [52].

ATLAS and CMS

During Run 1 of the LHC, neither ATLAS nor CMS conducted specific searches targeting this GMSB model. Consequently, initially reinterpretations involved various existing searches to explore this signature. The only LHC search for displaced leptons, which did not involve the reconstruction of a displaced vertices, was carried out by the CMS experiment. However, this search did not focus on slepton decays but rather on an R-parity violating $\tilde{t}$ decay model. It selected events featuring displaced leptons of different flavours, specifically $e\mu$, utilising 19.7 fb^{-1} of 8 TeV data [53]. Upon reinterpretation, it was determined that the constraints set by OPAL remained the most stringent.

For the longer lifetimes within this GMSB model, reinterpretations of a CMS search for heavy stable charged particles was conducted, which established robust constraints

for lifetimes above $c\tau \sim 2$ m [54]. For shorter lifetimes, reinterpretation of a disappearing track search conducted by CMS and ATLAS, resulted in stringent limits at $c\tau \sim 50$ cm [55, 56]. The reinterpretation demonstrated a significant enhancement over the OPAL result, and the details can be found in Figure 5.3. Notably, the mentioned reinterpretations were conducted on searches employing Run 1 data at a center-of-mass energy of $\sqrt{s} = 8$ TeV.

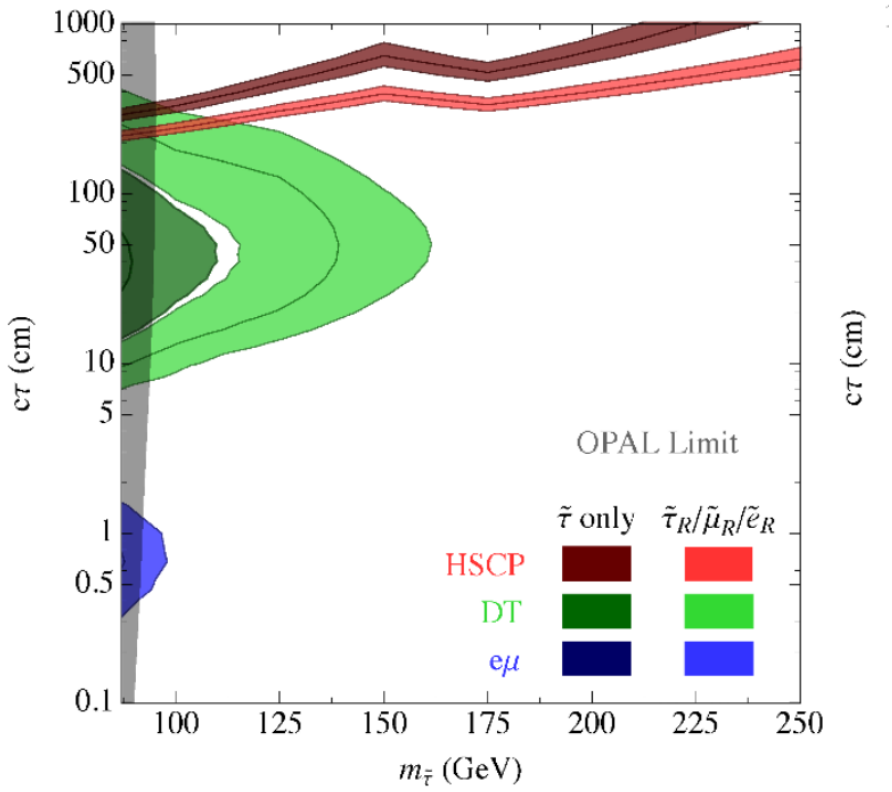

Figure 5.3: Constraints on direct production for the case of a single isolated, light, right-handed stau NLSP (dark), as well as for the case of nearly degenerate three generations of right-handed sleptons (bright). The CMS displaced $e\mu$ search is in blue. The disappearing track searches at CMS and ATLAS are in green, where only the most sensitive of the two is displayed. The CMS heavy stable charged particle search is in red. The most stringent LEP2 bounds from OPAL are shown in light grey [15].

5.3.2 LHC Run 2 Results

The shift to increase focus towards long-lived particles during Run 2 marked a significant advancement in reconstruction techniques and detection methodologies on both ATLAS and CMS. Combined with the higher center-of-mass energy compared to Run 1, these developments led to substantial enhancements in the constraints initially established by OPAL. Both ATLAS and CMS conducted dedicated searches aimed at probing this GMSB model. In the following section, we will delve into their outcomes, providing the motivation behind conducting the analysis presented in this work.

CMS

The recent CMS search [57] conducted during Run 2 specifically targeting this GMSB signal model employs a data-driven background estimation approach. The data is segregated into three distinct channels based on the lepton flavors: $ee, \mu\mu, e\mu$. Within each channel, the phase space is further divided into signal, SR I-IV, background and control regions, A-C, utilising the transverse impact parameters ($|d_0|$) of the two leptons as discriminators, as illustrated in Figure 5.4.

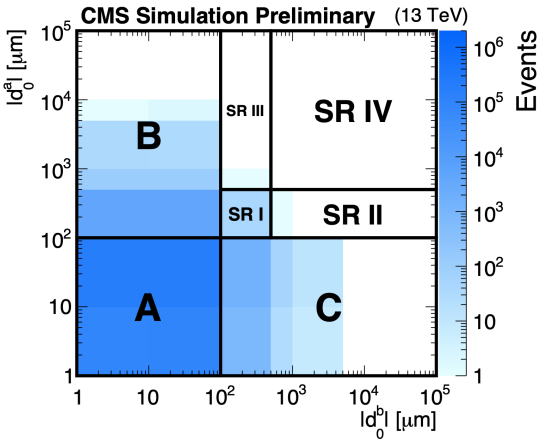

Figure 5.4: A diagram depicting the region separation of data in the recent CMS search. A, B and C are control regions, D is the inclusive signal region, SR, further separated into SRs I-IV [57].

The background in the signal region is estimated with an ABCD data-driven method, described in Chapter 6.4. Due to non-closure and significant correlation, an additional

uncertainty is assigned to account for this. The analysis excluded:

- $\tilde{\mu}$ with masses of at least 50 GeV with proper lifetimes between 0.2 ps and 8.8 ns, with a maximum exclusion at 610 GeV occurring at proper lifetime of 100 ps,
- $\tilde{e}$ with masses of at least 50 GeV with decay lengths between 0.007 and 70 cm, with a maximum exclusion at 610 GeV occurring at decay length of 0.7 cm,
- $\tilde{\tau}$ with masses of at least 50 GeV with decay lengths between 0.015 and 20 cm, with a maximum exclusion at 405 GeV occurring at decay length of 2 cm,

where the exclusion limits are shown in Figure 5.5.

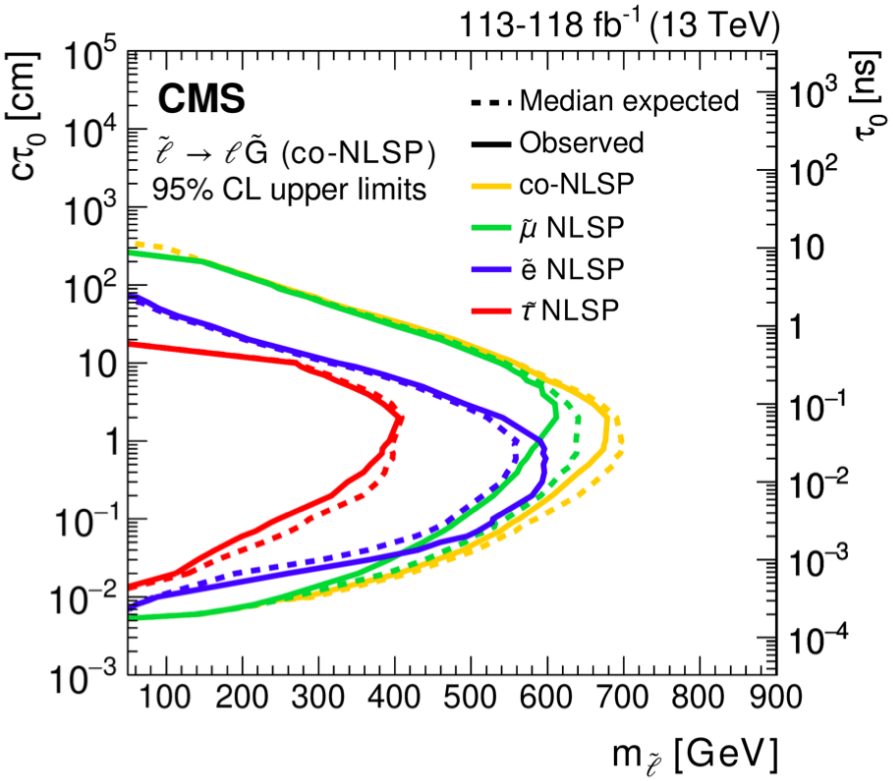

Figure 5.5: Constraints on long lived slepton lifetimes and mass obtained by the CMS search. [57]

ATLAS

There are two important results results coming from Run 2 searches on ATLAS. Differing from the CMS approach, ATLAS opted to divide and address distinct lifetime ranges using separate analyses. The slepton model was reinterpreted in a prompt search, targeting final states featuring two leptons and MET. This search was designed to target a model with slepton pair production where $\tilde{\chi}_1^0$ serves as the NLSP [58]. The higher end of the lifetime spectrum for this GMSB model was the focus of a search for leptons with high displacement employing large-radius tracking for reconstructing tracks [59].

This search succeeded in excluding sleptons within a lifetime range of 10 ps to 10 ns, with the most stringent exclusion at 100 ps, for masses up to 800 GeV. Both of these results are overlaid in Figure 5.6, revealing a narrow region in between the prompt search and the recent displaced lepton search that remains unexplored. This uncharted territory forms the core of the current analysis, which primarily focuses on a search for a GMSB model featuring $\tilde{G}$ as the NLSP, characterised by two moderately displaced leptons within the slepton lifetime range spanning from 1 ps to 100 ps. The requirement for the leptons to exhibit displacement is maintained, but the analysis employs conventional tracking techniques for track reconstruction.

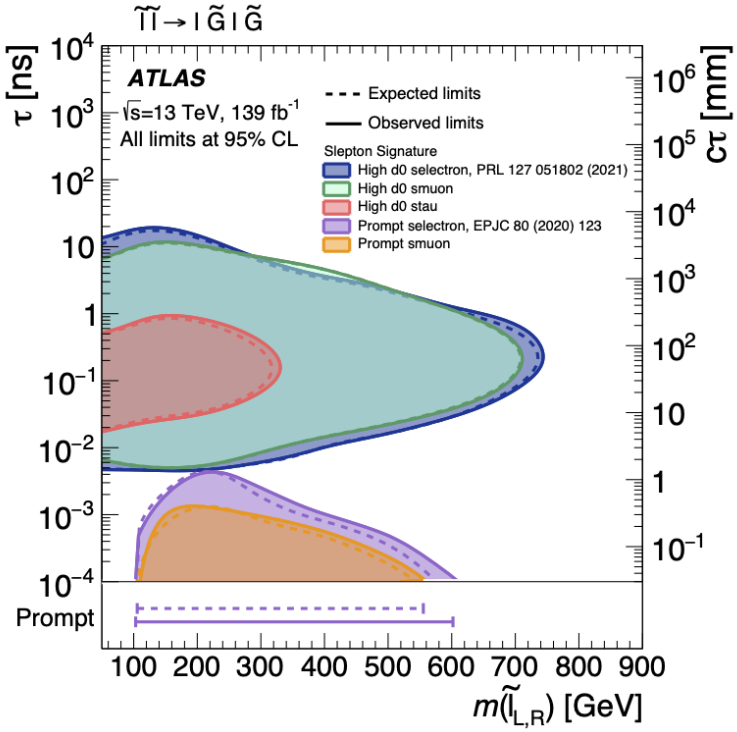

Figure 5.6: Expected (dashed) and observed (solid) exclusion contours for $\tilde{l}$ NLSP for the high d_0 analysis and prompt analysis reinterpretation.

Chapter 6

Search For Intermediately Displaced Leptons

In a typical particle physics analysis focused on the search for BSM phenomena, the initial step involves an examination of the signal model and its associated kinematics. Then, one must identify background processes, which are interactions that produce the same detector signature as the signal model but arise from SM processes, issues related to reconstruction, or incorrect object identification. In indirect searches, such as the analysis described here, it is often more convenient to employ the transverse impact parameter, denoted as d_0, as a measure of an object's displacement. The parameter d_0 is defined during the fitting process of an Inner Detector (ID) track, as discussed in Chapter 3.2.6.1. While the radial distance, R, from the collision point could theoretically provide immediate information about a particle's lifetime, the detector can only offer the radius of the first hit registered by the particle as it traverses through the detector. The initial silicon layer, known as the Insertable B-Layer (IBL), is situated at a distance of 33 mm from the interaction point. This is too far for the lifetimes considered in this analysis, as illustrated in Figure 6.1. Such a configuration would also introduce leptons originating from interactions with detector material as an additional source of background. Figure 6.1 presents a truth-level comparison between the lepton's radius of origin and its d_0 parameter. The calculation of d_0 relies on successful reconstruction of a track for either of the two lepton flavours. Tracking efficiency is assumed to be symmetric around

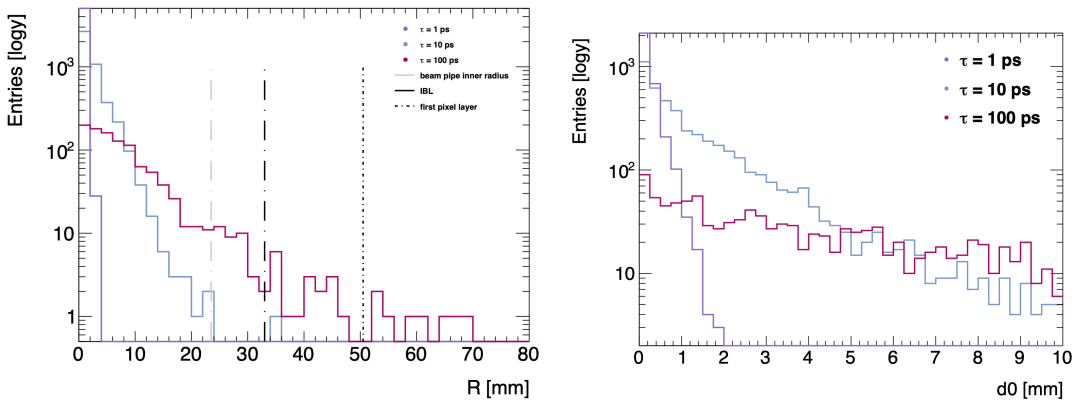

Figure 6.1: Truth level comparison of R, left, and d_0, right, parameters for muons coming from smuon decays with three different lifetimes; 1, 10 and 100 ps.

the detector volume and, after GSF tracking, equivalently efficient for both muons and electrons. A comparison of reconstruction efficiency for muons and electrons can be seen in Figures 6.2. The ability to reconstruct an electron object in comparison to a muon track is worse at the outer edges of the barrel region, where electrons can escape through material gaps without leaving energy in the forward calorimeters. Since this analysis relies on selection criteria based on d_0, defined in the xy-plane, it might be tempting to consider incorporating the z_0 track parameter, which is defined in the z-plane, to further enhance the separation between signal and background. However, as illustrated in Figure 6.3, a comparison of z_0 between signal and $Z \to \mu^+\mu^-$ Monte Carlo (MC) data reveals that the distributions exhibit a similar shape. Consequently, this variable cannot be effectively used for signal-background separation. Both d_0 and z_0 are defined relative to the beam spot. Nonetheless, the relatively large standard deviation of z_0 arises from the beam spot's substantial width in the z-plane: $\sigma_z \sim 34$ mm. In contrast, the beam spot width along the x and y axes is much smaller, approximately $\sigma_x \sim \sigma_y \sim 7\mu$m [60]. Consequently, the calculation of d_0 in the xy-plane is not significantly impacted by the uncertainty in beam spot size and maintains excellent resolution on the order of $\mathcal{O}(10)$ μm, as depicted in Figure 6.3.

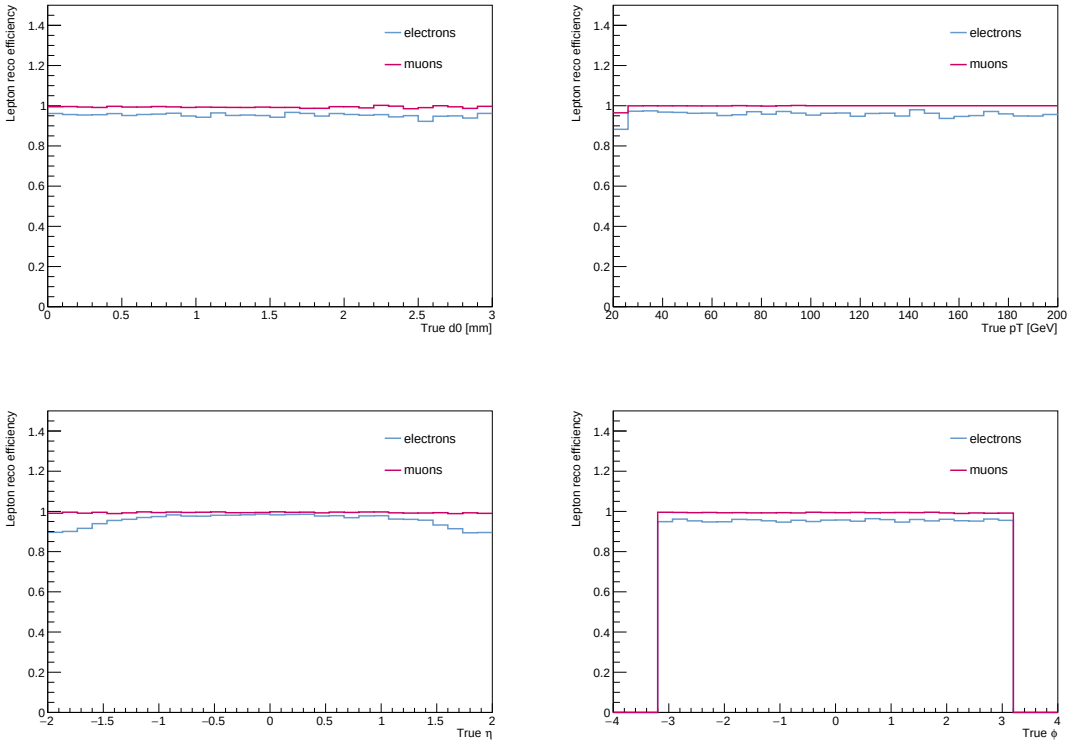

Figure 6.2: Reconstruction efficiency for electrons and muons coming from slepton decay as a function of true (generated) level d_0, p_T, η and Φ, in order from left to right and top to bottom.

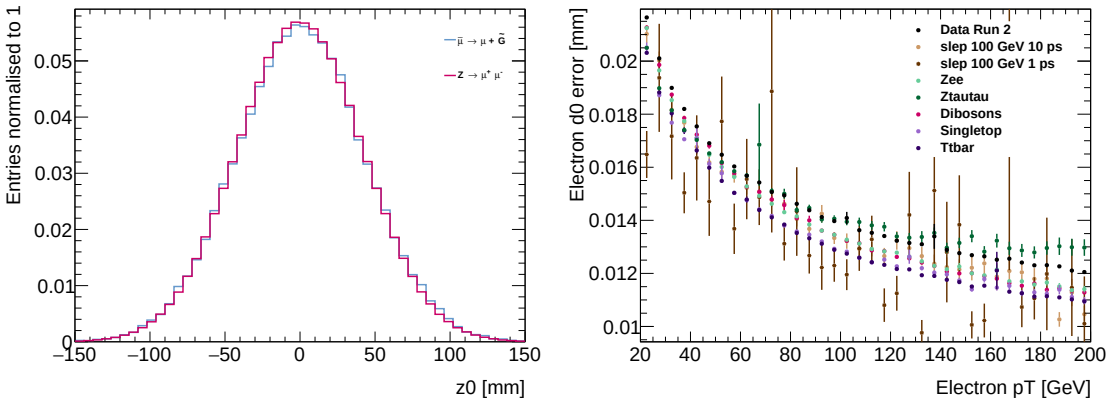

Figure 6.3: Comparison of z_0 distribution for signal and MC on the left and $\sigma(d_0)$ as a function of electron's p_T for data and MC on the right.

6.1 Analysis Strategy

This analysis is organised into three distinct regions, each categorised by the flavours of the lepton pairs under consideration. Within each region, there are subdivisions into control (CRs), validation (VRs), and signal (SRs) regions. The signal regions are strategically defined to maximise the dominance of the signal while minimising background contributions. If the sleptons are to exist, then the number of events in the signal regions would be greater than the expected background events. Therefore these regions are kept blinded until the analysis is fully developed. Control regions are in contrast very background dominant, with very few signal events. These regions are used to study potential discrepancies in the modelling of background processes in comparison to data. Importantly these regions facilitate the extraction of background estimations that can be extrapolated to the signal region. The validation regions serve the purpose of confirming the extrapolation method is correct.

The general event selection is characterised by a final state with two isolated opposite sign lepton pairs that have a transverse impact parameter between $0.1 < |d_0| < 3$ mm, where the signal region is defined as $|d_0| > 0.6$ mm. Potential background sources producing this signature are: single top production, $t\bar{t}$, $W \to l\nu$, $Z \to ll$ and di-boson production. The remaining sources of background originate from various factors, such as failures in reconstruction or identification algorithms, as well as the presence of large tails in decays associated with heavy flavour physics and cosmic ray muons.

Fake leptons result from the miss-association of an ID track with a calorimeter deposit in the case of electrons, or a MS track in the case of muons. These tracks do not correspond to real particles that have passed through the detector. This occurrence is more likely for electrons when the track is incorrectly matched to a genuine calorimeter deposit originating from photons or converted photons.

Despite the fact that the ATLAS detector is situated deep underground, muons can still penetrate through to it, particularly through the service shaft located above the detector. If this coincides with a collision, the event may be triggered and reconstructed as one or two muons. Last, events featuring either displaced muons and electrons experience a significant background due to decays associated with heavy flavour physics, primarily originating from b-hadrons. b-quarks are produced in abundance during LHC collisions, and they

hadronize into b-hadrons with an average lifetime of 1.5 ps, precisely within the targeted lifetime range of the signal sleptons. Approximately 11% of b-hadron decays include a lepton. None of these background sources are accurately modelled in MC simulations; thus, a data-driven background estimation method is employed.

6.2 Data and Monte Carlo Samples

Although this analysis uses a data-driven background estimation method, described in Section 6.4, this analysis uses both data and Monte Carlo for validation and selection optimisation. Monte Carlo samples of both the benchmark model and representative Standard Model backgrounds are generated to define signal regions, background sources and interpretation of the results.

6.2.1 Data

This analysis makes use of 139 fb^{-1} of $\sqrt{s} = 13$ TeV pp collision data collected by the ATLAS detector during Run 2. The data was collected using three different triggers depending on the lepton flavour combination, described in Table 6.2. In order to ensure that the data is of good quality, i.e. the LHC had stable beams, all sub-detectors were running, the solenoid magnet and toroid fields were in normal conditions and no excess detector-related noise was recorded, a so-called Good Run List (GRL) is produced centrally by the ATLAS collaboration [61]. The GRL removes entire luminosity blocks in which the detector was not performing optimally and additional quality selections have to be made on an event-level basis to account for sub-detector imperfections, these include:

- no events with noise bursts or data corruption from the LAr calorimeter,
- no corrupted events from the tile calorimeter,
- no events affected by the recovery procedure for single event upsets in the SCT,
- no incomplete events caused by Timing, Trigger and Control (TTC) restarts.

6.2.2 Monte Carlo

Monte Carlo samples are computer generated simulations or a given physics process, either from the SM or hypothetical new BSM processes. There are multiple reasons why MC samples are used in particle physics analysis:

- to estimate the types of processes one might expect in real data and at what rates,
- to model the behaviour of signal and background processes in order to optimise the analysis strategy for their discrimination,
- as a framework to interpret the significance of observed phenomena.

In this thesis MC simulations are used to study differences in kinematic variables for leptons coming from signal and potential background sources to find an analysis strategy maximising discovery potential. Additionally the MC is used to study the expected rates of signal and background sources as well as set limits on the masses and lifetimes of the signal model. Generating MC simulations is not a trivial matter.

Firstly, the physical process, the so-called hard-process, at the collision is modelled. As previously mentioned, the LHC collides protons, which are not elementary particles. The protons are composed of many partons; quarks and gluons, where the energy of the proton is divided amongst the constituent partons, therefore making the center of mass energy of the physical process unknown. This is modelled by Parton Distribution Functions (PDFs). They are probability density functions, $f(x, Q^2)$, where x is the fraction of the proton's longitudinal momentum carried by a parton and Q is the energy scale of the parton-parton interaction. The PDFs used to produce signal samples in this analysis are NNPDF23LO [62]. The MC generator then randomly generates the momenta of the particles in available phase space for many events based on the matrix element of the hard process. Generally, the MC generator is used to model the full process from hard scatter to final state particles, including radiation of initial and final state partons involved in the hard process, hadronisation and modelling of other interactions taking place within the same proton-proton collision. For this analysis MadGraph5_aMC@NLO [63] is used to produce $pp \to \widetilde{l}\widetilde{l}$ events with up to two additional radiated partons, using a perturbative QCD calculation at next-to-leading order accuracy. The hadronisation and

parton showering is handled by Pythia8.230 using the A14 tune [64]. Lastly simulated pileup collisions are overlaid onto the event to mimic the conditions at the LHC. Up to this stage the particles are referred to as truth-level and are stored in the MC simulations for later study.

Next each event is propagated through a simulation of the detector created in GEANT4 [65]. Each particle created at the previous step propagates through the detector simulation and all of its magnetic fields to accurately simulate the particle's trajectory, the detector signature and material interactions. The sleptons in the signal sample used in this analysis decay at this stage due to the sleptons longer lifetime. The decay products are then propagated through the detector simulation. Finally the particle trajectories are digitized, where the energy deposits of the particles are converted to the response of the read-out system of the ATLAS detector, which is then reconstructed the same way as data. At this stage the particles are referred to as reconstruction-level. An enormous amount of time an effort is put into modelling the MC as precisely and accurately as possible. However, many corrections must be made to the samples and the discrepancies between data and MC are an important uncertainty in this analysis and many others.

The simplified model used for the signal samples involves only a few particles and interactions in a given SUSY model. All sparticles not directly involved in the assumed topology have their masses set sufficiently high that they can be considered decoupled and the gravitino mass is fixed at 0.1 keV. The signal samples are generated with different lepton flavours $\tilde{l}$, over a range of masses, from 50 to 700 GeV, and lifetimes of 0.1, 1, 10 and 100 ps, where a mass degeneracy between the left- and right-chiral states is assumed. The sleptons are produced according to their cross sections, roughly 2/3 left-handed and 1/3 right-handed. The mixing of $\tilde{\tau_1}$ and $\tilde{\tau_2}$ is set to be $\sin\phi_{\tilde{\tau}} = 0.95$. In addition to the signal MC samples, several background MC samples are used to define the signal, background and validation regions. The dominant background process, $pp \to bb \to ll$, is not well modelled, therefore that MC sample is not used and a fully data-driven background estimation is used to determine its contribution.

Lifetime Reweighting of Signal Samples

Signal samples are produced with only a few representative mean lifetimes. In order to obtain the intermediate lifetime points, a reweighting procedure is performed. Each slepton decays independently, so they are reweighted separately. If τ is the proper lifetime of the slepton, then the probability of the slepton decay at time t is:

$$P(t) = \frac{1}{\tau} \exp(-\frac{t}{\tau}). \tag{6.1}$$

The probability of a slepton of the same mass, but different proper lifetime $\tau^{'}$, to decay at the same time is:

$$P^{'}(t) = \frac{1}{\tau^{'}} \exp(-\frac{t}{\tau^{'}}). \tag{6.2}$$

To reweigh a MC sample with the slepton proper lifetime τ to $\tau^{'}$, we define a weight for each slepton:

$$w_i = \frac{\tau}{\tau^{'}} \exp(\frac{t_i}{\tau} - \frac{t_i}{\tau^{'}}), \tag{6.3}$$

where the event weight, after reweighting of both slepton lifetimes, is simply the product: $w_{event} = w_1 w_2$. Figure 6.4 shows the truth level distribution of the proper lifetime for a slepton sample generated with the average lifetimes of 1 ps and 10 ps and the distribution of a 10 ps sample reweighted down to 1ps. The agreement between $|d_0|$ distributions with the true lifetime and after reweighting are within statistical uncertainty.

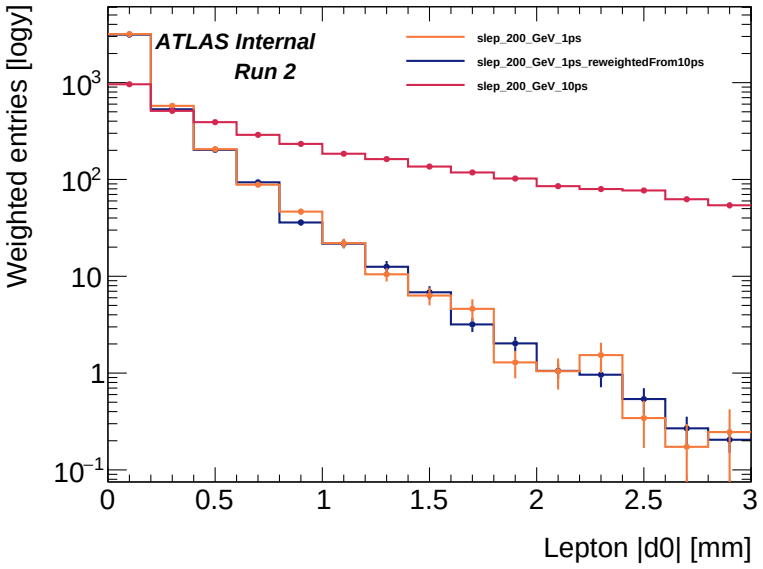

Figure 6.4: Truth level distribution of d_0 for slepton of mass 200 GeV with generated lifetimes of 1 ps and 10 ps in comparison to 10 ps sample reweighted down to 1 ps.

6.3 Event Selection

In addition to the quality criteria already discussed in Chapters 3.2.6 and 6.2.1, events must pass a trigger. Triggers used in this analysis are presented in Table 6.2. The naming convention follows the description in Section 3.2.5. They select events based on lepton combinations and a p_T cut of 20 GeV is imposed to make sure the triggers are fully efficient. The leptons must reside within $|\eta| < 2.5$, pass lepton quality criteria and satisfy the loose isolation cut. Events with invariant mass of the two leptons $m_{ll} < 20$ GeV are rejected in order to reduce background contribution from SM processes, specifically aiming to remove events where same leptons come from b-hadrons. Events are required to have a reconstructed primary vertex, which is defined as the vertex with the highest $\sum p_T^2$ of associated tracks to the vertex and the vertex is required to have at least two tracks. As the sleptons in the signal samples used in this analysis have a long mean lifetime, there is no requirement that the lepton tracks should point to or be matched to the primary vertex. The initial selection and quality requirements are summarised in Table 6.1.

From the pool of events in which at least two leptons meet the selection criteria, five distinct datasets are created to target smuons, selectrons, and staus. For the selectron

variable/lepton flavour	μ	e
p_T	> 20 GeV	
$\|\eta\|$	< 2.5	
$\|d_0\|$	0.1 mm $< \|d_0\| <$ 3.0 mm	
invariant mass	> 20 GeV	
quality	Medium	LooseAndBLayerLLH
isolation	PflowLoose_VarRad	Loose_VarRad

Table 6.1: Overview of lepton selection criteria.

variable/lepton combination	ee	$\mu\mu$	$e\mu$
trigger	HLT_2e17_lhvloose_nod0	HLT_2mu14	HLT_e17_lhloose_nod0_mu14

Table 6.2: Overview of triggers used per lepton combination.

signal samples, from the dataset that comprises events with two electrons, we select events in which highest p_T electrons both satisfy the selection criteria outlined in Table 6.1. Similarly, a dataset for the smuon search is formed, which includes events with the two highest p_T muons that meet the selection criteria. In the case of staus, the stau can produce final states with all lepton combinations, so the data is categorised into three sets based on the flavour of lepton pairs: $ee, \mu\mu, e\mu$. In each case, the highest two p_T leptons must pass the previously described selection criteria for the specific channel. However, in situations where multiple leptons are present in an event, that event could potentially be counted multiple times across different stau channels. To check for potential contributions from such events a control region is used where all leptons in the event have $d_0 < 0.6$ mm. In this region the number of events where at least two lepton combinations satisfy selection criteria is counted. The result is presented in Table 6.3 with each step in the selection includes the previous step. As the number of events with multiple lepton combinations passing selection criteria is not zero, the dataset for staus is further split. In each channel, where the two leptons passed selection criteria, we additionally require that those leptons are the highest two p_T leptons in the event.

To asses the efficiency of this selection, a similar calculation is performed using the stau signal MC. In events passing signal selection the highest two p_T leptons are selected

selection	number of events
multiple leptons with 0.1 mm $<|d_0|<$0.6 mm	974420
$\geq$ 3 leptons pass ID cut	14357
$\geq$ 3 leptons eta $<\|2.5\|$	14357
$\geq$ 3 leptons with p_T >20 GeV	2035
$\geq$ 3 leptons pass isolation	194
$\geq$ 2 combinations of leptons with m_{ll} >20 GeV	5
$\geq$ 2 combinations of leptons are opposite sign	5
event passes multiple triggers	1

Table 6.3: Cutflow yields for events with multiple leptons.

and then checked, at truth level, if these leptons originate from stau decays. Yields across channel in this truth analysis for a single representative stau sample are presented in Table 6.4. Efficiency of this selection, calculated as the ratio of truth matched and total events across channels, is > 99%.

channel	total	truth matched
ee	2055	2052
$\mu\mu$	5203	5198
$e\mu$	3395	3382
total	10653	10632

Table 6.4: Yields for stau MC across channels.

6.4 Background Estimation

In this analysis, background estimation is performed separately for each lepton flavour combination due to variations in the sources and amounts of background. Figure 6.5 illustrates the total production cross section measurements conducted by the ATLAS detector for several Standard Model (SM) processes. It is evident that W and Z boson production at the LHC are the most dominant background processes, followed by top quark and di-boson productions. All these particles have decay modes that result in two leptons in the final state. For example, $Z \to l^+l^-$, $t\bar{t} \to l^+\nu_l l^-\bar{\nu}_l b\bar{b}$. While the W boson cannot

directly decay to two leptons, it can decay to a lepton and a neutrino pair, $W \to l\nu_l$. In some cases, another lepton of opposite charge can be produced from a separate interaction within the same event, leading to the same signature as our signal.

The nature of the background sources also influences the design of the signal regions, which are described in detail in Sections 6.4.2- 6.4.4. However, a consistent data-driven background estimation method is applied across all of them. This chapter provides an overview of this method and outlines the approach taken for its validation.

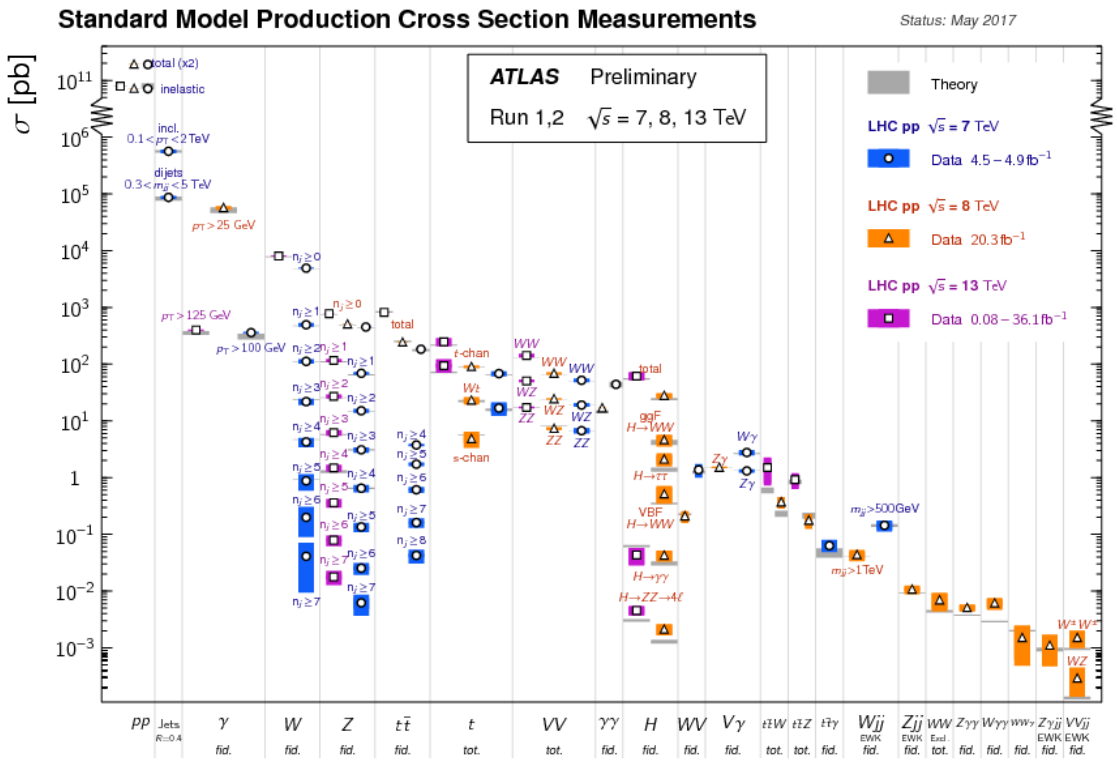

Figure 6.5: A summary of cross-section measurements in pp collisions for a variety of SM processes by the ATLAS collaboration. [66]

6.4.1 ABCD Data-Driven Background Estimation

The ABCD method makes selection cuts on two independent variables in order to separate the data into four regions in a 2D plane. The two continuous variables chosen in this analysis are the absolute values of the transverse track parameter, d_0, of the two leptons. Signal region, D, is defined by a region where both leptons d_0 are above a certain value

and the cuts are allowed to be asymmetric. The signal region cut can be inverted to form three additional regions; A, B and C, which serve as CRs. The cuts are visualised in a 2D plane in Figure 6.6.

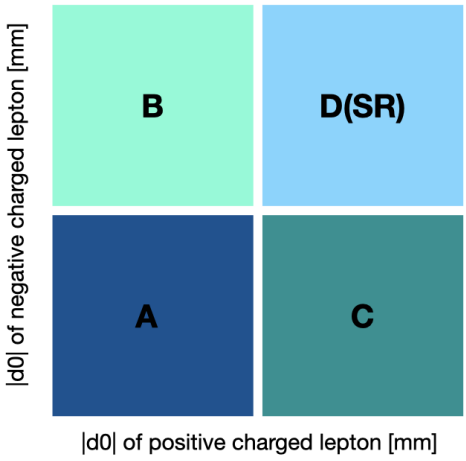

Figure 6.6: Diagram depicting the initial ABCD regions.

The basic assumption of the ABCD method is that the following relationship holds:

$$\frac{N_B^{bkg}}{N_A^{bkg}} = \frac{N_D^{bkg}}{N_C^{bkg}} \tag{6.4}$$

where $N_i^{bkg}, i \in \{A, B, C, D\}$ is the number of background events in the i-th region. If the number of signal events in regions A, B and C is significantly low in comparison to the number of background events in each region, then the number of background events can be estimated in the region D by:

$$N_D^{pred.bkg} = \frac{N_B^{bkg} \times N_C^{bkg}}{N_A^{bkg}}. \tag{6.5}$$

6.4.1.1 Extending the ABCD Method

In order to improve the ability to discriminate between the signal and background, additional uncorrelated variables may be added to region definitions. In this analysis the invariant mass of both leptons and their opening angle, ΔR, are added. Their discriminating abilities are shown in Figure 6.7. The opening angle is added as a single

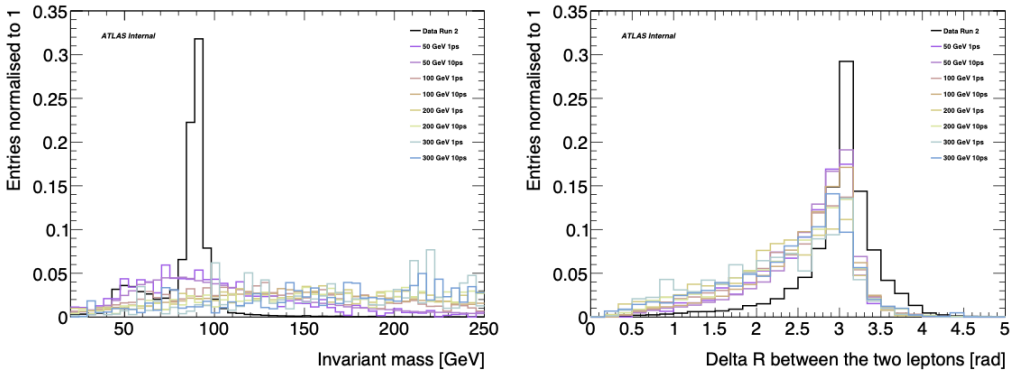

Figure 6.7: Comparison of invariant mass, on the left, and opening angle, on the right right, distributions for data and signals of various lifetimes and masses, as indicated in the legend.

cut while the invariant mass was added as an additional separation variable, therefore extending the ABCD method from a 2D to a 3D estimation, as illustrated in Figure 6.8. The signal region is now region H and the predicted number of background events can be calculated by:

$$N_H^{pred.bkg} = \frac{N_B^{bkg} \times N_G^{bkg}}{N_A^{bkg}}. \tag{6.6}$$

Due to the region G lying in the set of regions with higher invariant mass cut, as well as higher cuts in d_0, it can have a higher signal to background ratio. In order to estimate the background contribution using only regions with the least amount of signal contamination, the yields in region G are replaced by an estimation from other regions as:

$$N_H^{bkg} = \frac{N_C^{bkg} \times N_E^{bkg}}{N_A^{bkg}}. \tag{6.7}$$

Substituting this into the previous equation yields:

$$N_H^{pred.bkg} = \frac{N_B^{bkg} \times N_C^{bkg} \times N_E^{bkg}}{(N_A^{bkg})^2}. \tag{6.8}$$

If a potential new particle exists, then: $N_i^{data} = N_i^{signal} + N_i^{bkg}$. Therefore under the assumption that the signal events are negligible in regions A, B, C and E, the number of

expected background events in H is:

$$N_H^{pred.bkg} = \frac{N_B^{data} \times N_C^{data} \times N_E^{data}}{(N_A^{data})^2}. \tag{6.9}$$

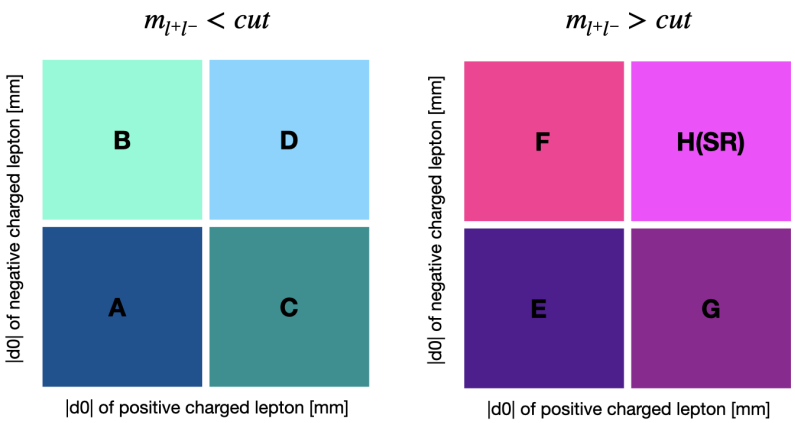

Figure 6.8: Diagram depicting the extended ABCD regions.

6.4.1.2 Fine Tuning

Since all of the discriminating variables in this analysis are continuous, it makes it possible to perform a scan of all possible region sizes and their combinations in order to maximise the signal sensitivity. Apart from d_0 and the invariant mass, the opening angle, ΔR, is used as a separation criterion, which proved to be helpful with reducing signal contamination as will be shown in Chapter 6.4.2.

The regions A-H can be separated to include gaps between them, as shown in Figure 6.9. These gaps provide a further separation between background and signal enriched regions as well as provide regions for validation. The scan includes all possible regions where ranges and relationships defined in Table 6.5 are obeyed. Favourable region definitions are found by studying: the expected CL_s values, the expected significance, signal contamination and number of events in each of the regions used in the background

estimation to assure there is enough statistics. CL_s are further described in Chapter 8.2. The scan does not include any systematic uncertainties or statistical uncertainty on the signal samples. Due to the number of regions and signal samples, the computing time is reduced for each grid point by using the PyHF [67, 68] package for CL_s and significance calculation. Favourable regions are found for all datasets and signal combinations as outlined in Section 6.3.

variable	range	steps	requirement
low_d0_CR	0.1 - 0.5 mm	0.1 mm	difference between low_d0_CR and high_d0_CR is at least 0.1 mm
high_d0_CR	0.2 - 0.6 mm	0.1 mm	
low_d0_SR	0.2 - 3.0 mm	0.1 mm	difference between low_d0_SR and high_d0_SR is at least 0.1 mm
high_d0_SR	0.3 - 3.0 mm	0.1 mm	
invariant mass	25 - 210 GeV	5 Gev	/
ΔR	0.0 - 5.0 rad	0.1 rad	/

Table 6.5: Table of discriminating variables and their ranges used to optimise the ABCD method. Invariant mass and opening angle cut have no dependance or requirements on the other variables.

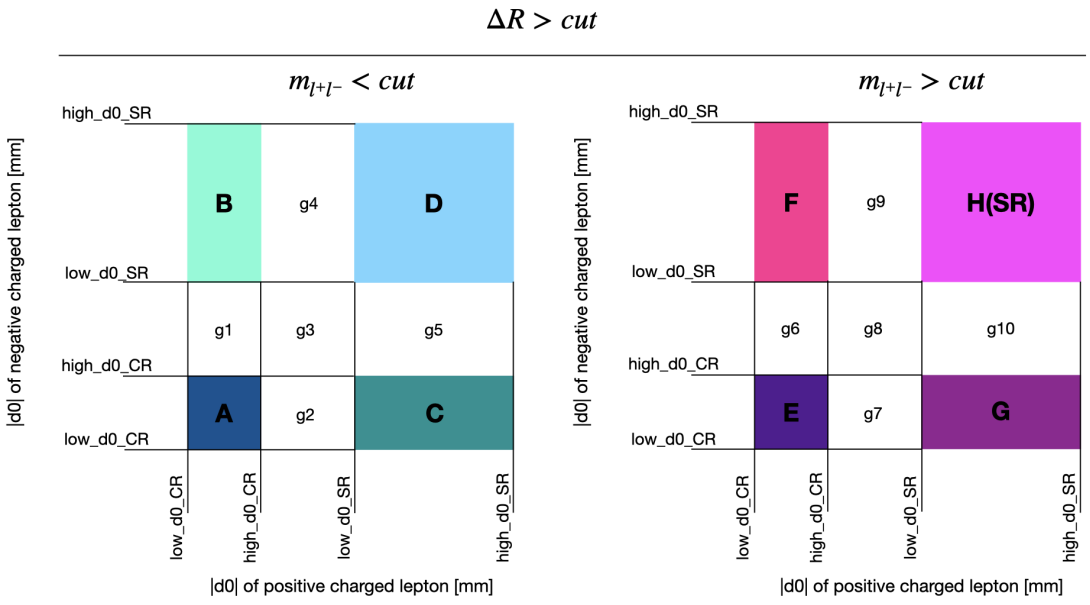

Figure 6.9: Diagram depicting the extended ABCD regions with gaps.

6.4.1.3 Validaton

The ABCD method has two basic assumptions, which allow for the ABCD method to hold. Firstly, that the variables used for separation are uncorrelated.

Correlation Studies

Two random variables can have nonlinear dependance, which would invalidate the methods assumptions. Therefore both a Pearson correlation test as well as a distance correlation test is performed. They are both calculated for both lepton d_0 as well as for each leptons d_0 and invariant mass. To perform this test in data, the signal region is blinded and three control regions are defined as visualised in Figure 6.10 and listed below:

- CR1: $0.1 < |d_0|_{l^+} < 0.6$ mm, $0.1 < |d_0|_{l^-} < 0.6$ mm,
- CR2: $0.1 < |d_0|_{l^+} < 0.6$ mm, $0.6 < |d_0|_{l^-} < 3.0$ mm,
- CR3: $0.6 < |d_0|_{l^+} < 3.0$mm, $0.1 < |d_0|_{l^-} < 0.6$ mm,

where l^+ and l^- indicate the variable corresponds to the positive and negative charged lepton respectively. These regions are also used in MC.

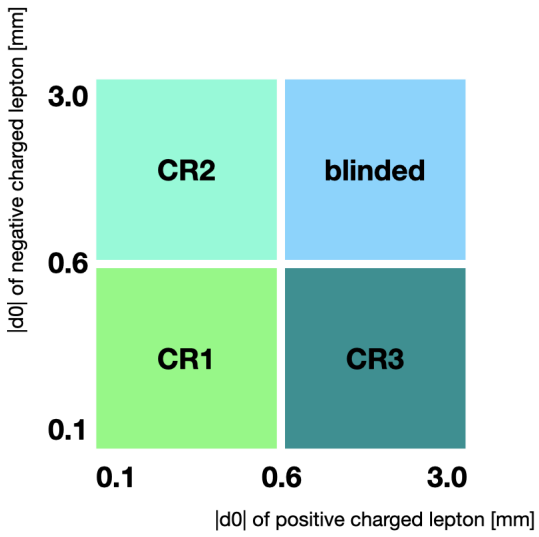

Figure 6.10: Diagram depicting the control regions for correlation studies.

The Pearson correlation coefficient is defined as:

$$\rho_{X,Y} = \frac{Cov(X,Y)}{\sigma_X \sigma_Y}, \tag{6.10}$$

where X and Y are two random variables and $Cov(X,Y)$ is the covariance:

$$Cov(X,Y) = \mathbb{E}[(X - \mu_X)(Y - \mu_y)] \tag{6.11}$$

A value close to 0 indicates linear independence. To test for possible non-linear relationship the distance correlation is used. If (X_k, Y_k), $k = 1, 2, .., n$ is a statistical sample of the variables X and Y, the $n \times n$ distance matrices $(a_{j,k})$ and $(b_{j,k})$ that contain all pairwise distances are:

$$\begin{aligned} a_{j,k} &= ||X_j - X_k|| \\ b_{j,k} &= ||Y_j - Y_k|| \end{aligned} \tag{6.12}$$

where $j, k = 1, 2, .., n$ and $||\vec{v}||$ is the Euclidean norm of a vector v: $||\vec{v}|| = \sqrt{\vec{v} \cdot \vec{v}}$. One can then define the double-centred matrices $A_{j,k}$ and $B_{j,k}$ as:

$$A_{j,k} = a_{j,k} - \overline{a_{j,\cdot}} - \overline{a_{\cdot,k}} + \overline{a_{\cdot\cdot}} \tag{6.13}$$

$$B_{j,k} = b_{j,k} - \overline{b_{j,\cdot}} - \overline{b_{\cdot,k}} + \overline{b_{\cdot\cdot}} \tag{6.14}$$

where $\overline{a_{j,\cdot}}$ and $\overline{a_{\cdot,k}}$ contain row-wise and column-wise means respectively and $\overline{a_{\cdot\cdot}}$ is the grand mean of the matrix. The sample distance covariance and distance variance are therefore:

$$\mathrm{d}Cov_n^2(X,Y) = \frac{1}{n^2} \sum_{j=1}^{n} \sum_{k=1}^{n} A_{j,k} B_{j,k} \tag{6.15}$$

$$\mathrm{d}Var_n^2(X) = \mathrm{d}Cov_n^2(X,X) = \frac{1}{n^2} \sum_{k,l}^{n} A_{k,l}^2 \tag{6.16}$$

and the distance correlation is:

$$\mathrm{d}Cor(X,Y) = \frac{\mathrm{d}Cov(X,Y)}{\sqrt{\mathrm{d}Var(X)\mathrm{d}Var(Y)}}. \tag{6.17}$$

The distance correlation value can range from 0 to 1, where the former implies independence between X and Y. To ensure enough statistics for the correlation study, this is performed with the leptons selection criteria defined in 6.1 per lepton flavour combination. The study is summarised in Tables 6.6- 6.14. No significant correlation is found in the $\mu\mu$ and $e\mu$ channels. In the ee channel a small correlation is observed, but due to the lack of statistics, the uncertainties are relatively large as well. From this we expect some disagreement in closure in the ee channel, details are described in Section 6.4.3.

region name	number of events	Pearson correlation factor	error	distance correlation
CR1	61,677	0.016	0.004	0.017
CR2	5,357	0.035	0.014	0.012
CR3	5,292	0.0078	0.014	0.0084

Table 6.6: Pearson correlation factor and distance correlation between $|d_0|$ positive and negative charged leptons in $\mu\mu$ channel for data.

region name	number of events	Pearson correlation factor	error	distance correlation
CR1	14398	0.09	0.01	0.09
CR2	104	-0.11	0.10	0.18
CR3	137	-0.12	0.09	0.18

Table 6.7: Pearson correlation factor and distance correlation between $|d_0|$ positive and negative charged leptons in ee channel for data.

region name	number of events	Pearson correlation factor	error	distance correlation
CR1	17214	0.02	0.01	0.02
CR2	823	-0.00	0.03	0.05
CR3	818	-0.04	0.03	0.06

Table 6.8: Pearson correlation factor and distance correlation between $|d_0|$ positive and negative charged leptons in $e\mu$ channel for data.

region name	number of events	Pearson correlation factor	error	distance correlation
CR1	61,677	-0.015	0.0040	0.012
CR2	5,357	-0.0088	0.014	0.020
CR3	5,292	-0.033	0.014	0.052

Table 6.9: Pearson correlation factor and distance correlation between $|d_0|$ of the positive muon and $m_{\mu\mu}$ for data.

region name	number of events	Pearson correlation factor	error	distance correlation
CR1	14398	-0.12	0.01	0.17
CR2	104	0.23	0.10	0.32
CR3	137	-0.28	0.09	0.31

Table 6.10: Pearson correlation factor and distance correlation between $|d_0|$ of the positive electron and m_{ee} for data.

region name	number of events	Pearson correlation factor	error	distance correlation
CR1	17214	-0.01	0.01	0.01
CR2	823	-0.03	0.03	0.07
CR3	818	0.02	0.03	0.05

Table 6.11: Pearson correlation factor and distance correlation between $m_{e\mu}$ and $|d_0|$ of the positive charged lepton in $e\mu$ pair for data.

region name	number of events	Pearson correlation factor	error	distance correlation
CR1	61,677	-0.0063	0.0040	0.019
CR2	5,357	0.026	0.014	0.052
CR3	5,292	-0.010	0.014	0.031

Table 6.12: Pearson correlation factor and distance correlation between $m_{\mu\mu}$ and $|d_0|$ of the negative charged muons for data.

region name	number of events	Pearson correlation factor	error	distance correlation
CR1	14398	-0.11	0.01	0.16
CR2	104	-0.21	0.10	0.29
CR3	137	0.01	0.09	0.11

Table 6.13: Pearson correlation factor and distance correlation between m_{ee} and $|d_0|$ of the negative charged electron for data.

region name	number of events	Pearson correlation factor	error	distance correlation
CR1	17214	0.00	0.01	0.01
CR2	823	-0.06	0.03	0.07
CR3	818	0.04	0.03	0.05

Table 6.14: Pearson correlation factor and distance correlation between $m_{e\mu}$ and $|d_0|$ of the negative charged lepton in $e\mu$ pair for data.

Signal Contamination

The second assumption of the ABCD method is that the regions used for estimating the background yields have very little signal contamination. This means that:

$$\delta_i \equiv \frac{N_i^{sig}}{N_i^{bkg}} \ll 1 \quad \forall\, i \in \{A, B, C, E\}, \tag{6.18}$$

and this holds for all regions simultaneously. Another relevant quantity, as shown in [69], is the normalised signal contamination, defined as:

$$r_H \equiv \delta_H^{-1}(\delta_C + \delta_B + \delta_E - 2\delta_A) = (\frac{N_H^{sig}}{N_H^{bkg}})^{-1}(\frac{N_C^{sig}}{N_C^{bkg}} + \frac{N_B^{sig}}{N_B^{bkg}} + \frac{N_E^{sig}}{N_E^{bkg}} - 2 \times \frac{N_A^{sig}}{N_A^{bkg}}), \tag{6.19}$$

which implies that for the ABCD method to be valid $r_H \ll 1$ must be satisfied. To explicitly show this, we first assume that the following holds exactly:

$$N_H^{bkg} = \frac{N_B^{bkg} \times N_C^{bkg} \times N_E^{bkg}}{(N_A^{bkg})^2}. \tag{6.20}$$

If there is any signal contamination, then we can substitute the contributions from C into the equation:

$$N_H^{pred.bkg} = \frac{N_B^{bkg} \cdot (1+\delta_B) \cdot N_C^{bkg} \cdot (1+\delta_C) \cdot N_E^{bkg} \cdot (1+\delta_E)}{(N_A^{bkg} \cdot (1+\delta_A))^2}. \tag{6.21}$$

Simplifying and keeping terms of first order of δ:

$$N_H^{pred.bkg} = \frac{N_B^{bkg} \times N_C^{bkg} \times N_E^{bkg}}{(N_A^{bkg})^2}(1+\delta_B+\delta_C+\delta_E-2\delta_A) \tag{6.22}$$

Since Equation 6.20 holds exactly, this leaves:

$$N_H^{pred.bkg} = N_H^{bkg}(1+\delta_B+\delta_C+\delta_E-2\delta_A) \tag{6.23}$$

Substituting in Equation 6.19:

$$N_H^{pred.bkg} = N_H^{bkg}(1+r_H \cdot \delta_H), \tag{6.24}$$

δ_H is typically large as the signal contribution in H should be significant in order to be sensitive to finding a signal. Therefore, for the background prediction to not be over inflated $|r| \ll 1$. If the background is inflated, signal the sensitivity is greatly reduced. Signal contamination is further analysed in each channel for the relevant signal smaples.

Closure Test

In order to validate that the ABCD method accurately described the background distribution, the gap regions g1-g3 and A,B,C and E are used. If the selected set of regions does include gaps, then the number of events in gap regions g4-g7 are predicted. Gaps g8, g9, g10 and regions E, F and D are not used, since they represent regions with high signal contributions and can be subsets of other signal regions as will be proven to be the smuon case in SR$\mu\mu$. The estimated number of events in validation regions is calculated via the relationship 6.5, yielding:

$$
\begin{aligned}
N_{g_4}^{pred.} &= \frac{N_B^{data} \times N_{g_2}^{data}}{N_A^{data}} \\
&= \frac{N_B^{data} \times N_{g_3}^{data}}{N_{g_1}^{data}} \\
N_{g_5}^{pred.} &= \frac{N_C^{data} \times N_{g_1}^{data}}{N_A^{data}} \\
&= \frac{N_C^{data} \times N_{g_3}^{data}}{N_{g_2}^{data}} \\
N_{g_6}^{pred.} &= \frac{N_{g_1}^{data} \times N_E^{data}}{N_A^{data}} \\
N_{g_7}^{pred.} &= \frac{N_{g_2}^{data} \times N_E^{data}}{N_A^{data}}
\end{aligned}
$$

The estimated number of events is compared to the observed number of events by defining σ as:

$$
\sigma = \frac{N_i^{pred.} - N_i^{data}}{\sqrt{\mathrm{Err}(N_i^{pred.})^2 + \mathrm{Err}(N_i^{pred.})^2}} \; i \in \{g_4, g_5, g_6, g_7\}, \tag{6.25}
$$

where the uncertainties are statistical. The uncertainty on N_i^{data} is the square root of the number and the uncertainty on $N_i^{pred.}$ is the propagated error from the calculation of $N_i^{pred.}$. Closure tests depend on the definition of signal regions per lepton flavour combinations and are conducted in each channel individually.

6.4.2 SR$\mu\mu$

The second-highest production cross section observed at the LHC is associated with the Z boson. One of the Z boson's decay modes is $Z \to \mu^+\mu^-$, resulting in two oppositely charged muons in the final state. While the Z boson's decay is prompt, it can also decay to $Z \to \tau^+\tau^-$, where tau leptons have a relatively short lifetime before they decay. Moreover, tau leptons can decay into muons, giving rise to an opposite-sign muon pair in the Z boson's decay. This decay process can result in muons that are displaced from the point of interaction. However, as depicted in Figure 6.11, this is not the predominant source of background in this channel. The primary background contribution arises from the decays of b-hadrons.

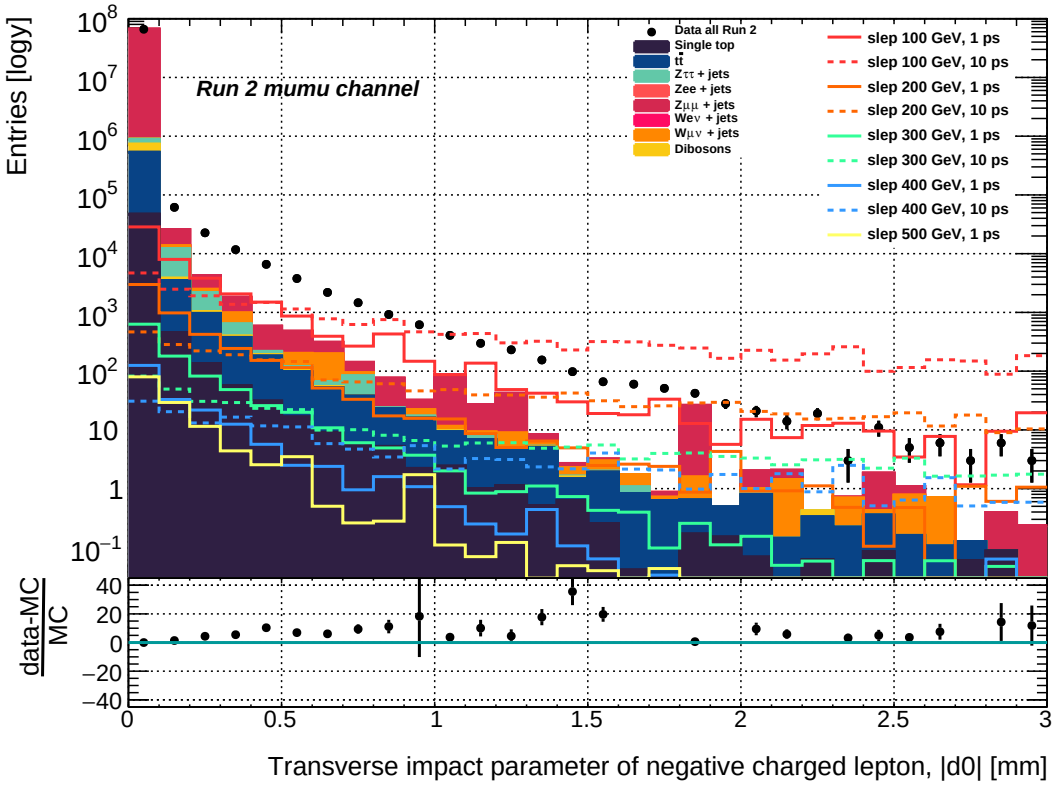

Figure 6.11: Distribution of the transverse impact parameter of negatively charged muon in the $\mu\mu$ channel.

If both of the muons originate from the same hadron, the d_0 variables would exhibit correlation. To ensure that the two muons do not originate from the same b-hadron, an initial invariant mass cut of $m_{\mu^+\mu^-} > 20$ GeV is applied. This threshold is chosen because it exceeds the mass of any of the b-hadrons in the bottomium family. Additionally the requirement that both muons have $|d_0|> 0.1$ mm is imposed. The justification of this cut is better seen in a 2D d_0 distribution of $Z \to \mu^+\mu^-$, $Z \to \tau^+\tau^-$ and data with the baseline selection, displayed in Figure 6.12. Following the removal of the dominant prompt processes, the primary remaining SM particles with non-negligible lifetimes are those associated with heavy flavor processes. Since there is no available cross-section information for b-physics Monte Carlo simulations, this represents a significant background contribution that is estimated using the data-driven background method.

Smuons

To further limit contributions from Z decays, the invariant mass cut is extended to $m_{\mu^+\mu^-} > 110$ GeV. The impact of this cut is seen in Figure 6.12. After performing the fine-tuning of ABCD regions, the results reveal that these regions fall into three sets based on the smuon masses. Regions 1 is the set of regions favourable for smuon masses ≥ 300 GeV, Regions 2 is suited for smuon masses of 200 GeV and Regions 3 is well-suited for smuon masses of 50 and 100 GeV. The details of these regions are summarized in Table 6.15. One

	$\lvert d_0\rvert_{CR}^{low}$	$\lvert d_0\rvert_{CR}^{high}$	$\lvert d_0\rvert_{CR}^{low}$	$\lvert d_0\rvert_{CR}^{high}$	$m_{\mu\mu}$	additional cut
Set of Regions 1	≥ 0.1	< 0.3	≤ 0.6	< 3	200	-
Set of Regions 2	≥ 0.1	< 0.3	≤ 0.6	< 3	140	-
Set of Regions 3	≥ 0.1	< 0.3	≤ 0.6	< 1.3	125	$\Delta R_{\mu\mu} > 3$

Table 6.15: Table containing the numerical values of parameters that define three sets of regions targeting smuon signal samples in the $\mu\mu$ channel. For visual representations see Figure 6.9.

can immediately spot the similarities between the sets of regions and wonder why is the most relaxed set not suitable for all smuon samples. The reason is signal contamination. The aim of decreasing the invariant mass cut is so that the number of signal events in the lower regions of the set, which are used for the background estimation, is small. Adding an

extra constraint on the opening angle between two muons in Regions 3 to be larger than a threshold might appear counterintuitive, as Figure 6.7 illustrates that cutting above a threshold reduces signal more than data. Nevertheless, this cut was required to control signal contamination for 50 and 100 GeV smuon samples, which have substantial cross sections. As a reminder, right-handed super-partners of the smuons of all lifetimes up to 93.3 GeV have been excluded by OPAL, the limit is seen in Figure 5.3. Table 6.16 provides an overview of the event counts in data within each group of regions and the predicted event counts in region H. These regions estimate that the analysis is sensitive to excluding

	N_A^{data}	N_B^{data}	N_C^{data}	N_E^{data}	predicted N_H^{bkg}
Set of Regions 1	2580 ± 51	290 ± 17	258 ± 16	183 ± 14	2.06 ± 0.25
Set of Regions 2	1721 ± 42	196 ± 14	182 ± 13	1042 ± 32	12.50 ± 1.48
Set of Regions 3	1045 ± 32	104 ± 10	109 ± 10	1659 ± 41	17.20 ± 2.62

Table 6.16: Data yields, A-E, and predicted number of events in H for three sets of regions targeting smuon signal samples.

($\mathrm{CL}_s < 0.05$) smuons of masses 50 GeV down to 1 ps, 200 GeV down to 2 ps, 200 GeV down to 2 ps, 300 GeV down to 2ps, 400 GeV down to 3ps and 500 GeV down to 6 ps. The analysis is also sensitive to finding evidence (with a significance $> 3\sigma$) of smuons of masses 50 GeV down to 2 ps, 100 GeV down to 2 ps, 200 GeV down to 2 ps, 300 GeV down to 3 ps and 400 GeV down to 6 ps. The values of δ_i and $|r|$, defined by 6.19, which quantify the amount of signal contamination, are calculated for each signal sample in their respected set of regions and were both found to be $\ll 1$. The numbers for a representative sample of smuon 600 GeV and 6 ps sample are:

$$\delta_A = 0.00020 \pm 0.00028$$

$$\delta_B = 0.0031 \pm 0.0033$$

$$\delta_C = 0.0040 \pm 0.0040$$

$$\delta_E = 0.0300 \pm 0.0140$$

$$|r| = 0.000037 \pm 0.000015$$

Staus in $\mu\mu$ channel

The invariant mass cut of 110 GeV imposed in the $\mu\mu$ channel for smuons before region selection has proven to be too stringent for staus. The amount of background in comparison to the small predicted yields of staus in the di-muon channel is too large and for this reason there is no sensitivity to staus in the regions selected for smuons. To specifically target stau decays to muon pairs the invariant mass cut is relaxed to 20 GeV before fine tuning the ABCD regions. The scan reveals there is no need for multiple regions due to very high background yields and subsequently low signal contamination for all masses and lifetimes. The selected region is defined in Table 6.17, the event counts and predicted number of events in region H are presented in Table 6.18.

	$\lvert d_0\rvert_{CR}^{low}$	$\lvert d_0\rvert_{CR}^{high}$	$\lvert d_0\rvert_{CR}^{low}$	$\lvert d_0\rvert_{CR}^{high}$	$m_{\mu\mu}$	additional cut
Set of Regions 1	≥ 0.1	< 0.3	≤ 0.6	< 3	65	-

Table 6.17: Table with numerical values of parameters that define two sets of regions targeting stau signal samples in the $\mu\mu$ channel. For visual representations see Figure 6.9.

	N_A^{data}	N_B^{data}	N_C^{data}	N_E^{data}	predicted N_H^{bkg}
Set of Regions 1	(1.505 ± 0.012)e+04	(1.660 ± 0.04)e+03	(1.680 ± 0.04)e+03	(1.197 ± 0.011)e+04	147 ± 6

Table 6.18: Data yields, A-E, and predicted number of events in H for two sets of regions targeting stau signal samples in the $\mu\mu$ channel.

This region estimates the analysis is sensitive to exclude ($\mathrm{CL}_s < 0.05$) staus in the $\mu\mu$ channel of masses 50 GeV in the range 50 ps down to 6 ps and 100 GeV 20 ps down to 12 ps. Values of δ_i and $|r|$ for all signal samples are calculated and found to be $\ll 1$. Values for a single representative sample of stau 100 GeV and 10 ps samples are:

$$\delta_A = 0.0001 \pm 0.0001$$

$$\delta_B = 0.0021 \pm 0.0004$$

$$\delta_C = 0.0024 \pm 0.0005$$

$$\delta_E = 0.0007 \pm 0.0001$$

$$|r| = 0.0320 \pm 0.0050$$

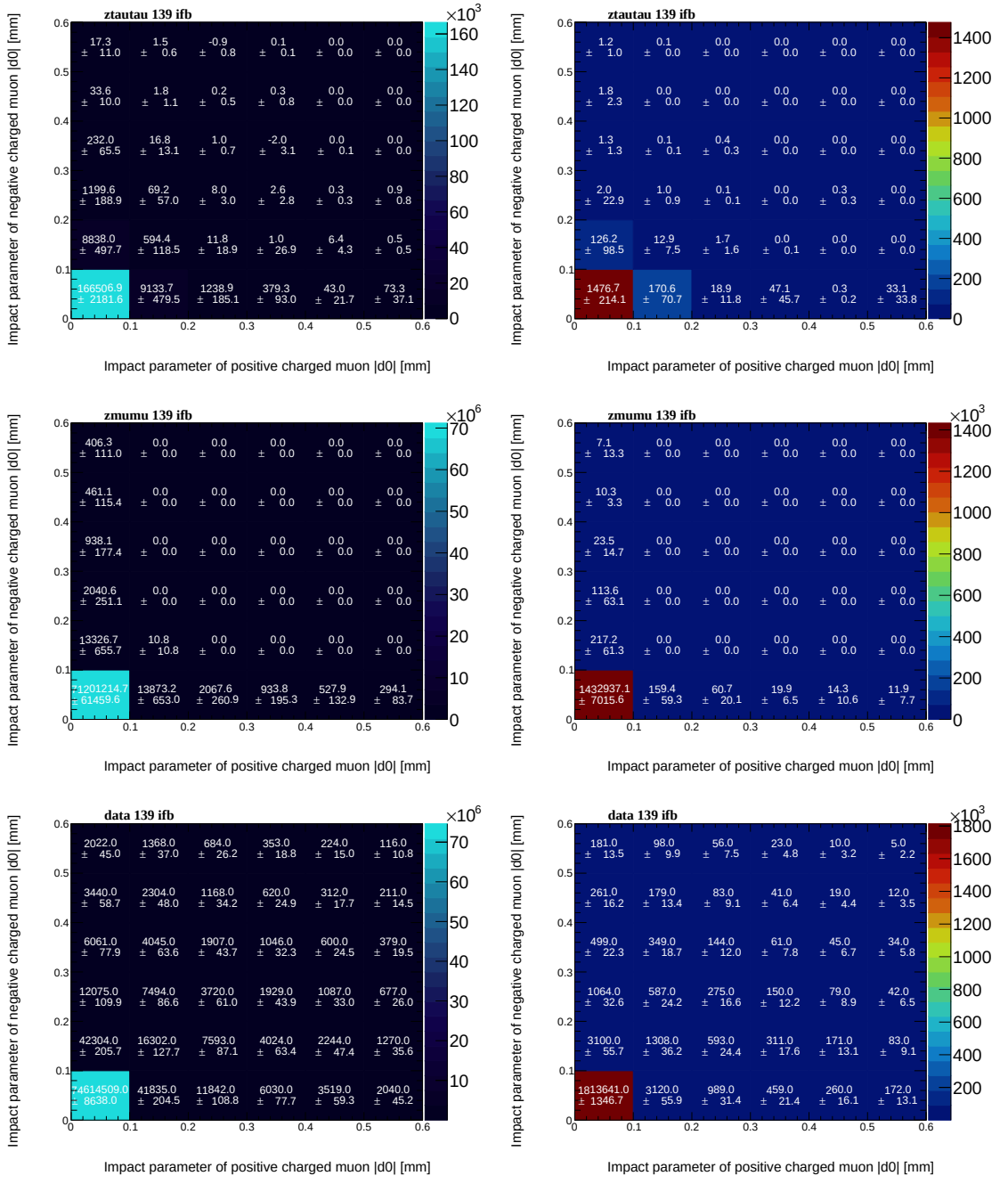

Figure 6.12: Z boson contributions to control regions in $\mu\mu$ channel before, left, and after, right, a 110 GeV invariant mass cut.

6.4.3 SRee

Similar to the SR$\mu\mu$ channel, the expectation is for the major SM contributions to come from Z boson and heavy flavour. However, due to the differences in lepton ID selection, these two channels exhibit a significant difference in the amount and background sources. The algorithms for both electron and muon identification are constructed using a comparison between data and simulated samples of $Z \to ee(\mu\mu)$ and $J/\psi \to ee(\mu\mu)$ decays. Both of those processes are prompt, however the muon identification algorithm is based on a cut approach as described in Section 3.2.6.3. The electron identification algorithm is based on a likelihood method as described in Section 3.2.6.2 and uses both d_0 and $\sigma(d_0)$ in the construction of the likelihood function. Since the function is trained on prompt events, it is highly biased towards selecting low d_0 electrons. The efficiency of electron ID is compared to the muons ID in Figure 6.13. The figure shows efficiency per lepton, resulting in an efficiency of $\approx 60\%$ at higher d_0 when requiring two electrons in the event. Although it might seem like a minor obstacle, its impact on data is substantial.

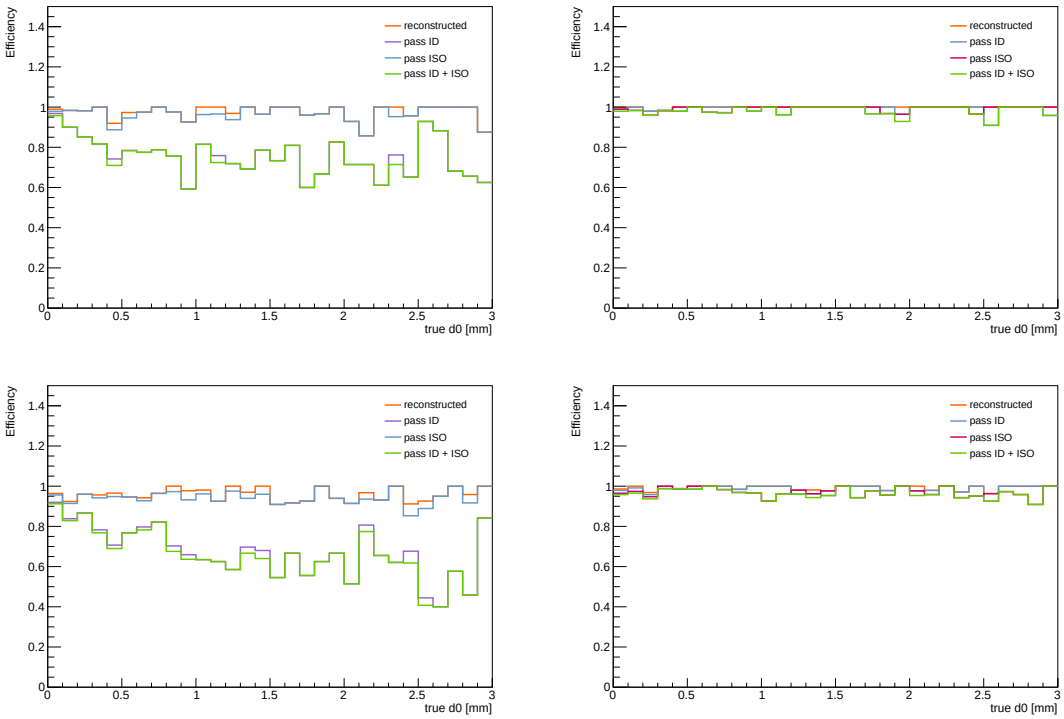

Figure 6.13: Lepton reconstruction, ID and isolation efficiency per lepton for the 50 GeV 0.1 ps slepton (top) and stau (bottom) samples in ee (left) and $\mu\mu$ (right) channels.

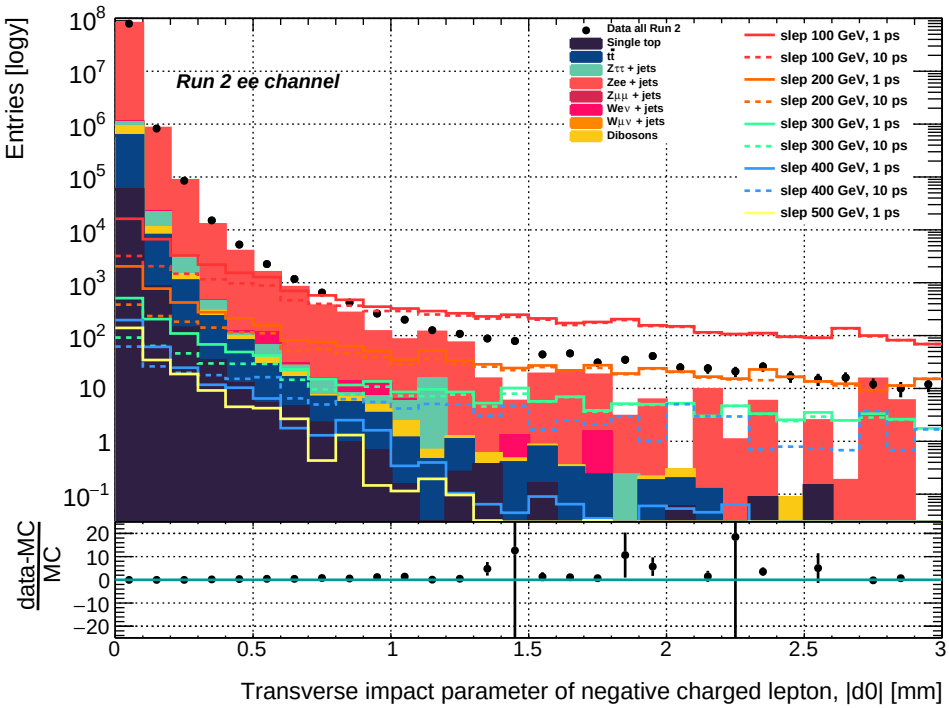

Figure 6.14: Distribution of the transverse impact parameter of negatively charged electron in the ee channel.

As depicted in Figure 6.14, due to the difference in lepton ID, data is better modelled by the SM MC than in the $\mu\mu$ channel and contributions from b-processes are almost completely reduced. This means that while b-physics is the sole background at high d_0, it is not the dominant process at lower d_0 where the control regions lie. If one was to use those CRs for background estimations, the variables would be exhibit correlation, therefore non-closure would be expected, but more importantly the prediction would be overestimating a background process that is simply not present in the high d_0 regions. To limit contributions coming from Z decays, but not those of b-physics, two avenues are explored:

1. impose a higher d_0 cut and optimise the 3D ABCD regions,

2. impose an invariant mass cut, $m_{ee} > 100$ GeV, keep the low d_0 cut, but resort to a 2D ABCD estimation.

Reasoning for these two options is better seen in 2D distributions of data and Z decays shown in Figure 6.15. The first option modifies the variables low_d0_CR and high_d0_CR, depicted in Figure 6.9 and defined in Table 6.5, such that their corresponding ranges, scanned in the fine tuning step, start at 0.2 and 0.3 mm respectively. This would not eliminate contributions coming from Z decays, but rather move the control regions higher in d_0 such that the $Z \to ee$ is no longer the dominant process. It is beneficial to explore, since this option leaves more data in CRs for validation studies. Following extensive studies, it became evident that there are significant differences in the underlying data distributions between the low and the high invariant mass regions when employing a 3D ABCD method. Validation studies revealed significant discrepancies between the predicted and observed number of events, as anticipated due to the strongest correlation being observed between the d_0 variables and invariant mass.

The second option eliminates contributions coming from $Z \to ee$, but leaves very limited statistics for further separation into the 8 A-H regions. This would result in predicted backgrounds with large uncertainties since there are low data yields in the control and validation regions. For this reason with an increase in the initial invariant mass cut the 3D ABCD background estimation is replaced by the classical 2D ABCD as depicted in Figure 6.6. The background estimate is then calculated with Equation 6.5. Note that this is equivalent to calculating the predicted number of events in H in the 3D ABCD version, but with regions E,F and G and further details are described in the language of 3D ABCD. The reason this was avoided and not explored in the di-muon channel is signal contamination; regions E, F and G are expected to have higher signal counts. Correlation is studied in modified regions depicted in Figure 6.10, where the invariant mass cut is raised. However as it can be seen from Figure 6.15, there are only a handful of events in CR1 and CR3 respectively. To increase statistics in the two edge regions, the signal region lower limit, previously set to 0.6 mm, is lowered to 0.2 mm. Correlation studies are presented in Table 6.19. Secondary contributions can come from algorithmic fakes. To study the contribution of electrons coming from mis-matched photons or converted photons, a truth level study is performed on $Z \to e^+e^-$, $Z \to \tau^+\tau^-$ and $t\bar{t}$ MC. Figure 6.16 shows that the fake contributions are negligible when using with the loosest, but in this regime stringent, ID requirement.

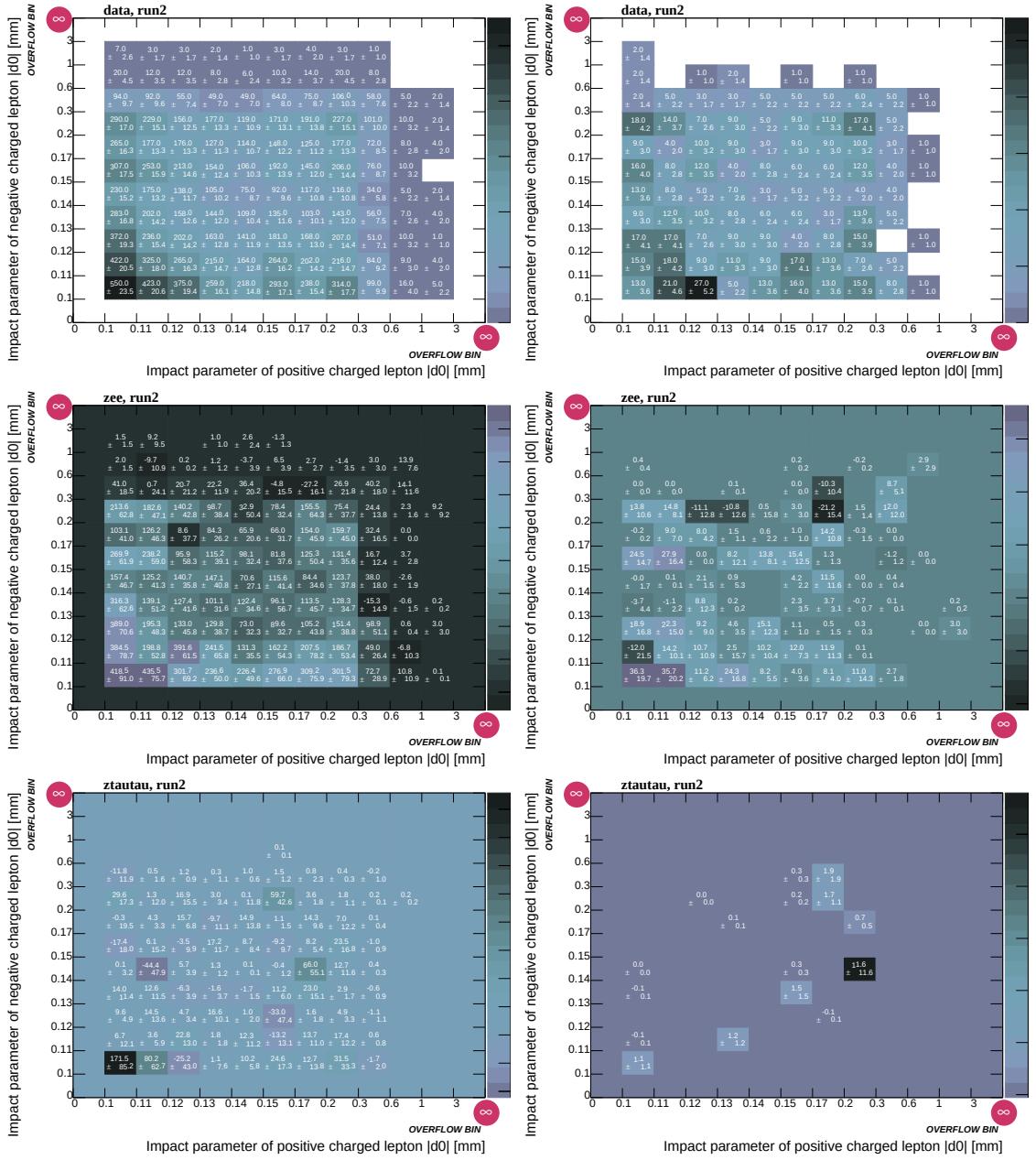

Figure 6.15: Comparison of 2D distributions of the transverse impact parameters of electrons in data and $Z \rightarrow ee$ MC before (left) and after (right) a 100 GeV invariant mass cut.

region name	number of events	pearson correlation factor	error	distance correlation
CR1	484	0.01	0.05	0.08
CR2	109	-0.12	0.10	0.18
CR3	109	0.01	0.10	0.13

Table 6.19: Pearson correlation factor and distance correlation between $|d_0|$ positive and negative charged leptons in ee channel for data with a $m_{ee} > 100$ GeV cut.

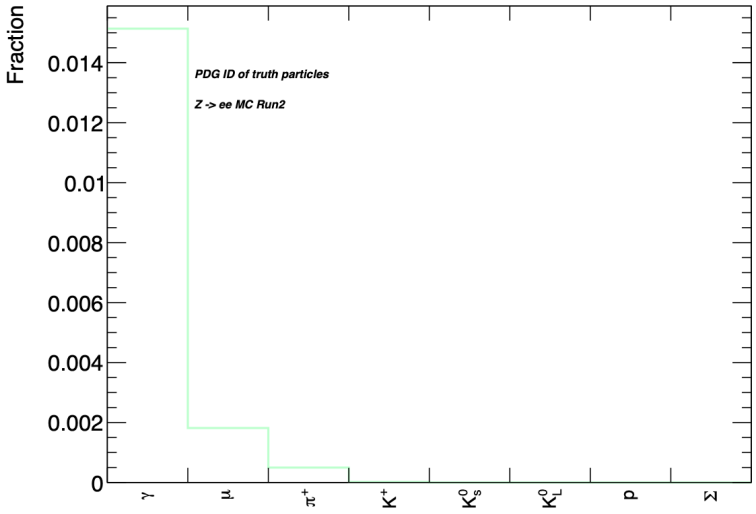

Figure 6.16: Fraction of particles, assorted by their truth PDG ID, that are identified as electrons at reconstruction level, but are not electrons at truth level.

Selectrons

Due to smaller background yields, in comparison to the di-muon channel, there is more sensitivity to the higher mass selectron samples with very low cross sections. With sensitivity to a wider range of masses, it is expected that a sole region will not be optimal for all signal samples. The selectron regions fall into three sets, defined in Table 6.20, which were selected such that the d_0 and invariant mass cuts vary as little as possible for maximal exclusion and reinterpretability in the future. Opening angle cuts are then

	$\lvert d_0\rvert_{CR}^{low}$	$\lvert d_0\rvert_{CR}^{high}$	$\lvert d_0\rvert_{SR}^{low}$	$\lvert d_0\rvert_{SR}^{high}$	m_{ee}	additional cut
Set of Regions 1	≥ 0.1	< 0.2	≤ 0.3	< 3	110	-
Set of Regions 2	≥ 0.1	< 0.2	≤ 0.3	< 3	110	$\Delta R_{ee} > 3.1$
Set of Regions 3	≥ 0.1	< 0.2	≤ 0.3	< 3	110	$\Delta R_{ee} > 3.4$

Table 6.20: Table containing the numerical values of parameters that define three sets of regions targeting selectron signal samples. For visual representations see Figure 6.9.

additionally added for the same reasons as in the smuon case; signal contamination. Set of Regions 1 is favourable for signal samples in the high mass range, Regions 2 is targeting signal samples with masses 400 - 500 GeV, Regions 3 is suited for samples with masses of 300 and below. Signal samples of mass 200 GeV and below exhibit significant signal contamination in that region. However, as a reminder the LEP results exclude selectrons of all lifetimes up to 65.8 GeV, the high-d_0 analysis excludes selectrons of masses 50 - 200 GeV down to ≈5 ps, while the lower lifetimes are covered by the prompt analysis. Table 6.21 provides an overview of the event counts in data within each group of regions and the predicted event counts in region H.

	N_E^{data}	N_F^{data}	N_G^{data}	predicted N_H^{bkg}
Set of Regions 1	262 ± 16	24 ± 5	22 ± 5	2 ± 0.6
Set of Regions 2	164 ± 13	19 ± 4	14 ± 4	1.6 ± 0.6
Set of Regions 3	86 ± 9	17 ± 4	9 ± 3	1.8 ± 0.8

Table 6.21: Data yields, E-F, and predicted number of events in H for four sets of regions targeting selectron signal samples.

These regions predict sensitivity to excluding selectrons of masses 50 GeV down to 1 ps, 100 GeV down to 1 ps, 200 GeV down to 1 ps, 300 GeV down to 1 ps, 400 GeV down to 1 ps, 500 GeV down to 1 ps, 600 GeV down to 2 ps and 700 GeV down to 2 ps. At the time of writing this thesis, samples with higher masses were not available for any lifetimes, nor were 700 GeV samples with lifetimes above 10 ps. The values of δ_i and $|r|$, which quantify the amount of signal contamination, are calculated for each signal sample in their respected set of regions and were both found to be $\ll 1$. The numbers for a representative sample of smuon 400 GeV and 10 ps sample are:

$$\delta_E = 0.0012 \pm 0.0003$$
$$\delta_F = 0.0495 \pm 0.0208$$
$$\delta_G = 0.0633 \pm 0.0268$$
$$|r| = 0.0098 \pm 0.0287$$

Staus in ee channel

As mentioned in Chapter 6.3, stau decays are separated into three orthogonal signal regions. This is done to enhance sensitivity to staus in a single multi-bin fit across channels, where a single signal strength parameter is used and can vary equally across channels. This exclusion fit setup is further described in Chapter 8. Since stau regions were fine tuned with a 3D ABCD method in the $\mu\mu$ channel, initially the same method is employed in the ee channel. This means the first option previously described in this section is employed, ie increasing the lower d_0 cut for CRs, but leaving the initial invariant mass cut at 20 GeV. The two sets of regions resulting from the ABCD fine tuning procedure showed big discrepancies between the predicted and observed number of events in the validation regions. This indicated that in the 3D ABCD method the background distribution in the lower invariant mass regions (A-D) is not equal to that in the higher mass regions (E-H). The background estimation resulting from this method would be wrong. Therefore background estimation is performed in the same manner as the selectron case; using a 2D ABCD method in the higher invariant mass regions. The fine tuning results in a selection of two sets of regions, defined in Table 6.22. The variation is needed to target the higher mass signal samples, but also reduce signal contamination for lower mass samples. The

set of Regions 1 is favoured by slepton masses of 200 GeV and above, Regions 2 is defined for sleptons of mass 100 and 50 GeV. Event counts and predicted number of events in region H are presented in Table 6.23. These regions predict the limits to exclude stau

	$\lvert d_0\rvert_{CR}^{low}$	$\lvert d_0\rvert_{CR}^{high}$	$\lvert d_0\rvert_{SR}^{low}$	$\lvert d_0\rvert_{SR}^{high}$	m_{ee}	additional cut
Set of Regions 1	≥ 0.1	< 0.2	≤ 0.4	< 3	100	-
Set of Regions 2	≥ 0.1	< 0.2	≤ 0.4	< 3	100	-

Table 6.22: Table containing the numerical values of parameters that define two sets of regions targeting stau signal samples in the *ee* channel. For visual representations see Figure 6.9.

	N_E^{data}	N_F^{data}	N_G^{data}	predicted N_H^{bkg}
Set of Regions 1	424 ± 21	20 ± 4	11 ± 3.32	0.52 ± 0.20
Set of Regions 2	313 ± 18	17 ± 4	11 ± 3.32	0.60 ± 0.23

Table 6.23: Data yields, E-F, and predicted number of events in H for three sets of regions targeting stau signal samples in *ee* channel.

samples of 200 GeV from 15 ps down to 3 ps, 100 GeV down to 2 ps and 50 GeV down to 2 ps. There is not a single set of regions for which signal contamination would be less than 0.1 for stau samples of 50 GeV with 1 ps lifetime. Again the values of δ_i and $|r|$, which quantify the amount of signal contamination, are calculated for signal samples in their respected set of regions and were both found to be $\ll 1$ for all other samples. The numbers for a representative sample of stau 300 GeV and 1 ps sample are:

$$\delta_E = 0.0001 \pm 0.0001$$

$$\delta_F = 0.0002 \pm 0.0001$$

$$\delta_G = 0.0004 \pm 0.0002$$

$$|r| = 0.0336 \pm 0.0292$$

6.4.4 SR$e\mu$

SM contributions in the $e\mu$ channel are predominantly from $Z \to \tau^+\tau^-$, W decays with an an additional lepton in the final state and $t\bar{t}$ events. Figure 6.17 shows a comparison of contributions from SM MC and data, where it can be seen that a non-negligible contribution is coming from b-physics processes. This contribution is smaller in relative comparison to the $\mu\mu$ channel, but larger that contributions in ee channel.

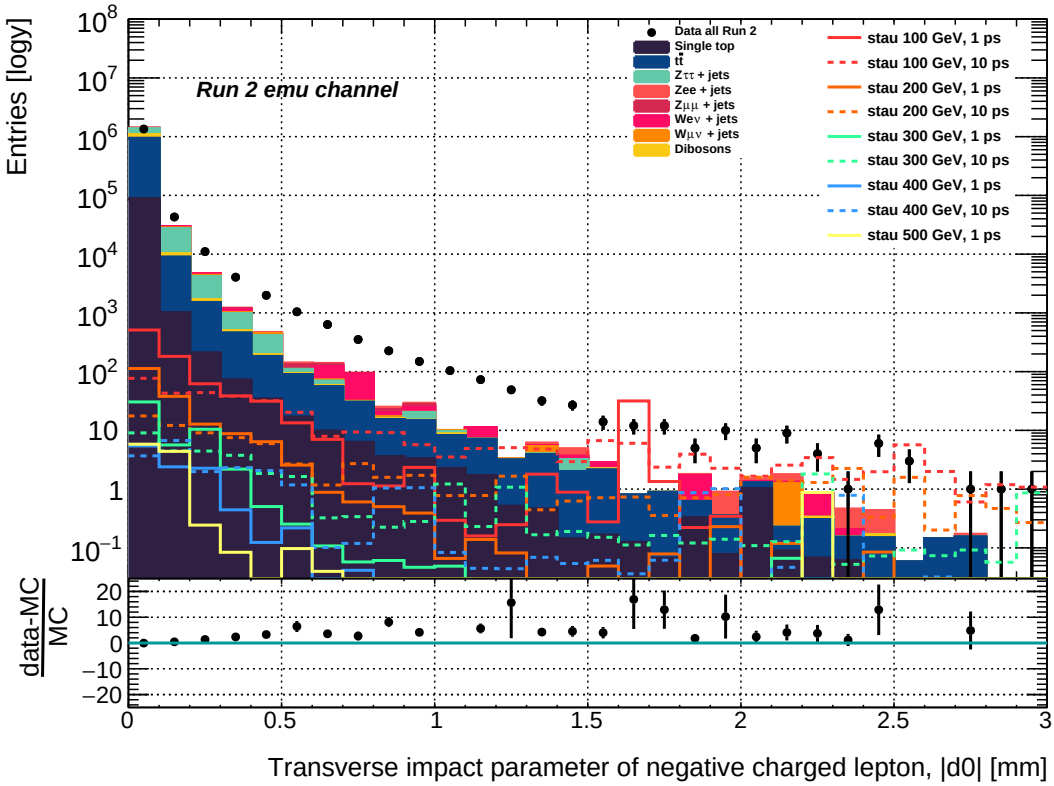

Figure 6.17: Distribution of the transverse impact parameter of negatively charged lepton in the *emu* channel.

To further limit contributions coming from Z decays, instead of an additional higher invariant mass cut, both leptons are required to have $|d_0| > 0.2$ mm. A comparison of 2D d_0 distributions between data in the control regions and $Z \to \tau\tau$ is shown in Figure 6.18.

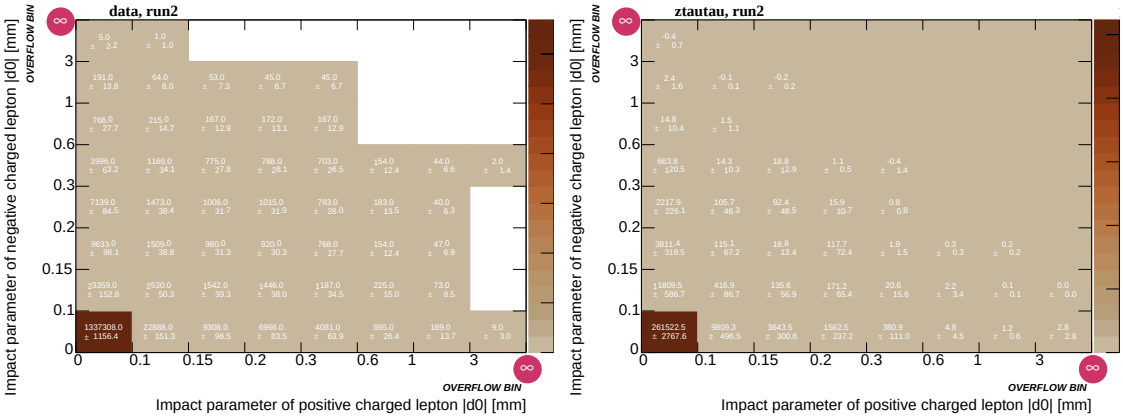

Figure 6.18: Comparison of 2D distributions of the transverse impact parameters of leptons in data and $Z \to \tau\tau$ MC.

Staus in $e\mu$ channel

It is expected that, since stau decays are split into three different channels, there would be statistically more events in the $e\mu$ channel than in channels with leptons of the same flavour. However, as was shown in Figure 6.17, the inclusion of a muon increases the contributions coming from heavy flavour processes and therefore background events. After performing the fine-tuning of the ABCD regions, the result show it is beneficial to select two sets of regions to target different stau mass points. Selecting more regions would give sensitivity only to higher lifetimes, which are already covered by the previous Run 2 high-d_0 analysis. The regions are defined in Table 6.24, with respective data yields in Table 6.25.

	$\lvert d_0\rvert_{CR}^{low}$	$\lvert d_0\rvert_{CR}^{high}$	$\lvert d_0\rvert_{CR}^{low}$	$\lvert d_0\rvert_{CR}^{high}$	$m_{\mu\mu}$	additional cut
Set of Regions 1	≥ 0.2	< 0.3	≤ 0.4	< 3	150	-
Set of Regions 2	≥ 0.2	< 0.3	≤ 0.5	< 3	70	-

Table 6.24: Table containing the numerical values of parameters that define two sets of regions targeting stau signal samples in the $e\mu$ channel. For visual representations see Figure 6.9.

	N_A^{data}	N_B^{data}	N_C^{data}	N_E^{data}	predicted N_H^{bkg}
Set of Regions 1	868 ± 29	487 ± 22	485 ± 22	11 ± 3.3	3.4 ± 1.1
Set of Regions 2	622 ± 25	348 ± 19	329 ± 18	257 ± 16	76 ± 10

Table 6.25: Data yields, A-E, and predicted number of events in H for three sets of regions targeting stau signal samples in the $e\mu$ channel.

Due to higher background yields in comparison to the di-electron channel, signal contamination is not an issue in this channel. In comparison to the di-muon channel, the background yields are smaller and there is sensitivity to samples of mass 200 GeV and lifetimes in range 3 - 15 ps, and mass 300 GeV with lifetimes 30 ps - 12 ps. Equally to the same flavour channels the power of exclusion extends to samples of mass 100 GeV down to 5 ps and 50 GeV down to 3 ps. Again the values of δ_i and $|r|$, which quantify the amount of signal contamination, are calculated for signal samples in their respected set of regions and were both found to be $\ll 1$ for all other samples. The numbers for a representative sample of stau 200 GeV and 1 ps sample are:

$$\delta_A = 0.0002 \pm 0.0001$$

$$\delta_B = 0.0002 \pm 0.0002$$

$$\delta_C = 0.0006 \pm 0.0002$$

$$\delta_E = 0.0236 \pm 0.0193$$

$$|r| = 0.2199 \pm 0.2587$$

Summary: Signal Region Selection

In summary, the previous three subsections have defined signal regions aimed at various signal samples based on the lepton flavour in the final state. Specifically, selectrons were targeted in the ee channel, smuons in the $\mu\mu$ channel, and staus in the ee, $e\mu$, and $\mu\mu$ channels. The determination of the number of signal regions within each channel took into account both the background process abundance and the expected sensitivity to the signal process. For instance, the $\mu\mu$ channel for smuons has three distinct signal regions, each focusing on different mass ranges of the signal samples, while there is only one signal region for staus decaying to $\mu\mu$ pairs. In the $e\mu$ and ee channels, lower data yields at higher d_0 were observed compared to the $\mu\mu$ channel. This heightened sensitivity to higher mass signal samples with low cross-section necessitated an increase in the number of signal regions for these channels to ensure minimal signal contamination in control regions.

The development of signal regions and background estimation methods in individual channels did not occur simultaneously. In the $\mu\mu$ channel, the ABCD method was selected to circumvent the use of b-physics MC, which exhibited notable miss-modelling of data at high d_0. Subsequently, after the publication of the $\mu\mu$ channel results, the ABCD method was adopted across the analysis for consistency. Initially, there were no indications that such different data yields would be observed in $\mu\mu$ and ee channels. This discrepancy was attributed to the structural differences in lepton identification. However, the significant reduction in b-physics contributions in channels with electrons in the final state posed challenges in ensuring sufficient statistics for the method and in eliminating contributions from Z decays. Electron channels exhibited larger tails in Z decays, compounding the difficulty in maintaining the method's validity. Hence, as Chapter 7 will elaborate, more significant non-closure discrepancies are observed in the electron channels. The definition of the signal region and the method employed in these channels is, therefore, provisional and data is not yet unblinded. Ongoing investigations aim not to replace the ABCD method but to modify its application or address its overestimation. Various alternatives are under consideration, such as defining additional regions entirely orthogonal to the currently proposed ones by inverting one of the selection criteria. This may involve selecting anti-isolated leptons or same-sign lepton pairs and subsequently deriving transfer factors to the existing signal regions. Another avenue involves deriving correction factors

from $Z \to ll$ MC and/or data with tagging Z decays, as detailed in [70]. Consequently, the subsequent chapters exclusively address the unblinded findings in the $\mu\mu$ channel while showcasing a promising sensitivity reach in the electron channels.

Chapter 7

Uncertainties

In order to accurately count the number of events in a signal region coming from a potential BSM model and compare it to the number of observed events in data, the uncertainties on these numbers have to be obtained. For this the extent to which the MC correctly simulates the actual environment we see in data has to be studied. In general the generated MC shows higher efficiencies than are seen in data. This is due to the fact that MC assumes a perfectly aligned detector with all of its subsystems performing optimally, which is not true in practice. The MC is corrected to better represent the data using *scale factors* or a systematic uncertainty is applied to the final signal counts. Since this analysis uses a data-driven background estimation method, the uncertainties one would expect arising from MC are signal process modelling, reconstruction and normalisation. The signal MC is normalised to the measured integrated luminosity in data for the 2015-2018 period of data taking. ATLAS periodically measures the luminosity using the LUCID-2 detector and the uncertainty on this measurement contributes a flat 0.83 % [71].

7.1 Experimental Systematic Uncertainties

The scale factors are calculated to account for the difference in reconstruction and selection efficiencies of leptons in MC and data. The total scale factor is a product of individual scale factors coming from trigger, reconstruction, identification and isolation steps:

$$\epsilon_{total} = \epsilon_{trigger} \times \epsilon_{reconstruction} \times \epsilon_{ID} \times \epsilon_{isolation}. \tag{7.1}$$

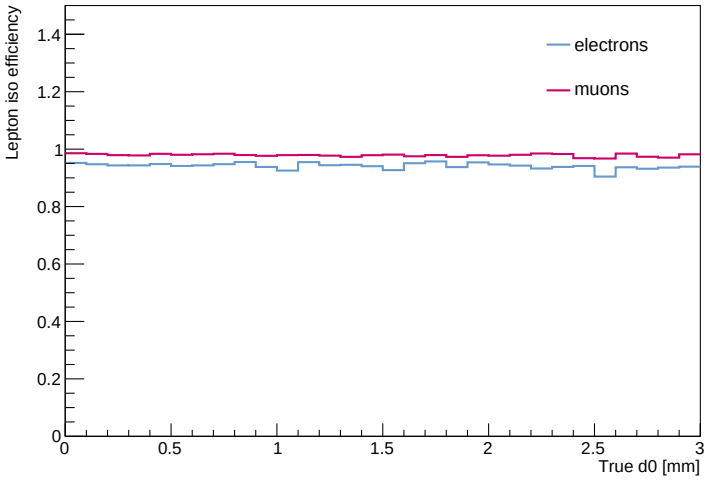

Figure 7.1: Lepton isolation efficiency per lepton for the 50 GeV 10 ps slepton sample.

Each individual scale factor is derived from a *tag and probe* analysis using $Z \to ee(\mu\mu)$ and $J/\psi \to ee(\mu\mu)$ events. The leptons are *tagged* by their invariant mass being close that of Z or J/ψ (within resolution effects), then the *probe* measures the selection efficiency by requiring that one of the leptons pass a given requirement. The statistical uncertainty on this value is evaluated and applied as an additional uncertainty on the signal. The ATLAS Collaboration centrally defines scale factors for prompt electrons and muons, so efficiencies in data and signal are studied for each step individually. Reconstruction efficiency was discussed in Chapter 6 and is shown in Figure 6.2. Identification efficiency was mentioned in Chapter 6.4.3 and shown in Figure 6.13 and isolation efficiency is shown in Figure 7.1. Identification and isolation efficiencies include reconstruction efficiency.

The systematic uncertainty is estimated by increasing/decreasing the scale factors up/down by the scale factor's statistical or systematic uncertainty. The increases/decreases are calculated using Gaussian smearing. For a given variable and variation, a Gaussian function with μ = nominal scale factor and σ = statistical uncertainty is constructed. Each lepton is then given a random value from this Gaussian and the scale factor for that lepton in increased/decreased by adding/substracting the difference of the value from the nominal value. The impact of these changes is then studied by comparing the distribution of key kinematic variables ($|d_0|, p_T, \eta$) for nominal and up/down variations. Figures 7.2 show the nominal and up/down variations for a

representative selectron signal sample. For all signal samples the majority of variations $\sigma_{nom}^{up(down)} < 0.2$ and so no systematic uncertainties are added.

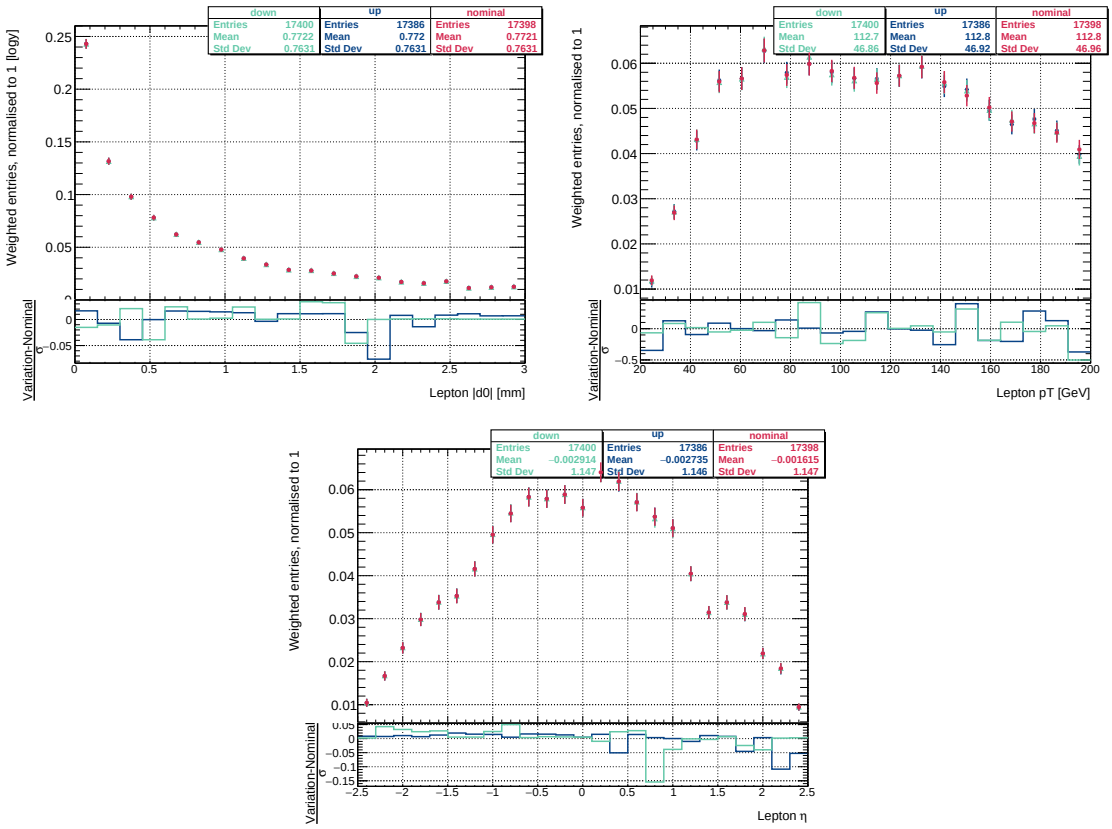

Figure 7.2: The down, up and nominal variations for the EGamma Resolution uncertainty in the selectron 200 GeV 10 ps signal MC sample plotted for key kinematic variables, in order: $|d_0|, p_T$ and η.

Tables 7.1- 7.2 shows the number of expected events in their respective signal regions for nominal and up/down variations on for those variations for which $\sigma_{nom}^{up(down)} > 0.5$. The last column in the table is the significance, defined as:

$$\sigma_{nominal}^{up(down)} = \left| \frac{N^{up(down)} - N^{nominal}}{\sqrt{(Err_{stat.}^{up(down)})^2 + (Err_{stat.}^{nominal})^2}} \right| \tag{7.2}$$

for the up/down variations and the systematic uncertainty. Where the distribution of possible variations is believed to be uniform and the corresponding Gaussian width is

calculated as:

$$\frac{N^{up} - N^{down}}{\sqrt{12}} \tag{7.3}$$

As can be seen in Table 7.1 the systematic uncertainty on the variation of PRW_DATASF, representing the uncertainty arising from pileup modelling, is much less than the statistical uncertainty, so no systematic is added. The only uncertainty added is that of trigger scale factors. The biggest deviations seen are presented in Table 7.2 and they are derived for each affected signal sample individually.

MC sample name	up ± stat. uncertainty	σ^{up}_{nom}	down ± stat. uncertainty	σ^{down}_{nom}	nominal ± stat. uncertainty ± syst. uncertainty
smuon 300 GeV 9ps	52.040 ± 2.058	0.520	51.252 ± 2.078	0.243	50.553 ± 1.989 (3.934 %) ± 0.227 (0.450 %)
smuon 300 GeV 10ps	53.809 ± 2.106	0.546	52.966 ± 2.137	0.256	52.211 ± 2.033 (3.895 %) ± 0.243 (0.466 %)
smuon 300 GeV 12ps	55.476 ± 2.203	0.576	54.508 ± 2.243	0.257	53.715 ± 2.122 (3.950 %) ± 0.279 (0.520 %)
smuon 300 GeV 15ps	54.980 ± 2.357	0.584	53.801 ± 2.373	0.222	53.075 ± 2.254 (4.247 %) ± 0.340 (0.641 %)
smuon 300 GeV 20ps	50.451 ± 2.561	0.555	48.994 ± 2.486	0.144	48.495 ± 2.419 (4.988 %) ± 0.421 (0.868 %)

Table 7.1: Signal yields for the up, down and nominal number of events for the variation PRW DATASF for the signal samples that have $\sigma > 0.5$.

MC sample name	up ± stat. uncertainty	σ^{up}_{nom}	down ± stat. uncertainty	σ^{down}_{nom}	nominal ± stat. uncertainty ± syst. uncertainty
smuon 400 GeV 3ps	5.189 ± 0.301	0.694	4.698 ± 0.273	0.518	4.902 ± 0.284 (5.795 %) ± 0.142 (2.892 %)
smuon 400 GeV 4ps	8.552 ± 0.375	0.926	7.740 ± 0.338	0.686	8.075 ± 0.352 (4.364 %) ± 0.234 (2.903 %)
smuon 400 GeV 5ps	11.553 ± 0.430	1.091	10.460 ± 0.387	0.807	10.911 ± 0.403 (3.693 %) ± 0.316 (2.893 %)
smuon 400 GeV 6ps	14.007 ± 0.471	1.204	12.686 ± 0.423	0.892	13.231 ± 0.441 (3.332 %) ± 0.381 (2.882 %)
smuon 400 GeV 7ps	15.914 ± 0.501	1.279	14.418 ± 0.451	0.948	15.035 ± 0.470 (3.124 %) ± 0.432 (2.872 %)
smuon 400 GeV 8ps	17.345 ± 0.526	1.324	15.719 ± 0.473	0.983	16.391 ± 0.493 (3.005 %) ± 0.469 (2.863 %)
smuon 400 GeV 9ps	18.385 ± 0.546	1.345	16.668 ± 0.492	1.001	17.378 ± 0.512 (2.944 %) ± 0.496 (2.852 %)
smuon 400 GeV 10ps	19.112 ± 0.564	1.348	17.333 ± 0.508	1.005	18.070 ± 0.529 (2.925 %) ± 0.514 (2.842 %)
smuon 400 GeV 12ps	19.879 ± 0.598	1.308	18.042 ± 0.540	0.980	18.805 ± 0.562 (2.987 %) ± 0.530 (2.820 %)
smuon 400 GeV 15ps	19.940 ± 0.657	1.176	18.117 ± 0.597	0.886	18.879 ± 0.620 (3.282 %) ± 0.526 (2.788 %)
smuon 400 GeV 20ps	18.678 ± 0.768	0.919	16.996 ± 0.703	0.699	17.705 ± 0.730 (4.123 %) ± 0.486 (2.743 %)
smuon 400 GeV 30ps	14.978 ± 0.895	0.613	13.656 ± 0.824	0.475	14.220 ± 0.855 (6.013 %) ± 0.382 (2.683 %)

Table 7.2: Signal yields for the up, down and nominal number of events for the variation MUON EFF TrigSystUncertainty for the 400 GeV signal samples.

7.2 Theoretical Uncertainties

Additional uncertainties come from renormalisation and factorisation scales that are used to generate the MC. These impact both the cross section measurement and the lepton

kinematics. The A14 tune optimises variations in parameters that correspond to initial and final state radiation and multiparton interactions. The variations have been reduced to a set ob observables: underlying event effects (VAR1), jet structure effects (VAR2) and three for different aspects of jet production (VAR3a, VAR3b, VAR3c). The sleptons decay in GEANT4, therefore d_0 is not available at truth level and since the distribution depends on the p_T and η of the lepton, those variables are studied. No significant deviation in those two kinematic variables is seen compared to the nominal values. A comparison of the up and down variations for both the η and p_T distribution is shown in Figures 7.3- 7.8. The cross section uncertainties are provided centrally and presented in Tables 7.3- 7.5.

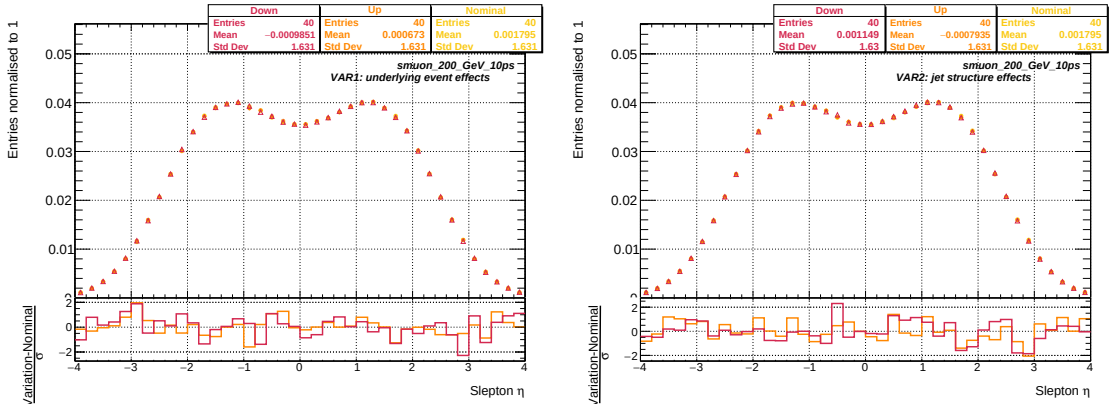

Figure 7.3: The up, down and nominal variations VAR1 (left) and VAR2 (right) for the η of the smuon in the smuon 200 GeV 10 ps signal MC sample.

Smuon mass [GeV]	Cross section σ [pb]	Down unc. [%]	Up unc. [%]
50	3.991	-3.9	2.2
100	0.2679	-1.8	1.6
200	0.02194	-1.9	1.9
300	0.004508	-2.1	2.2
400	0.001337	-2.8	3.0
500	0.0004836	-3.3	3.4
600	0.0001981	-3.6	3.6
700	8.836e-05	-3.8	3.8

Table 7.3: Summary table of cross-sections for slepton pair production for left-handed sleptons $\ell_L^+\ell_L^-$ and the associated uncertainties.

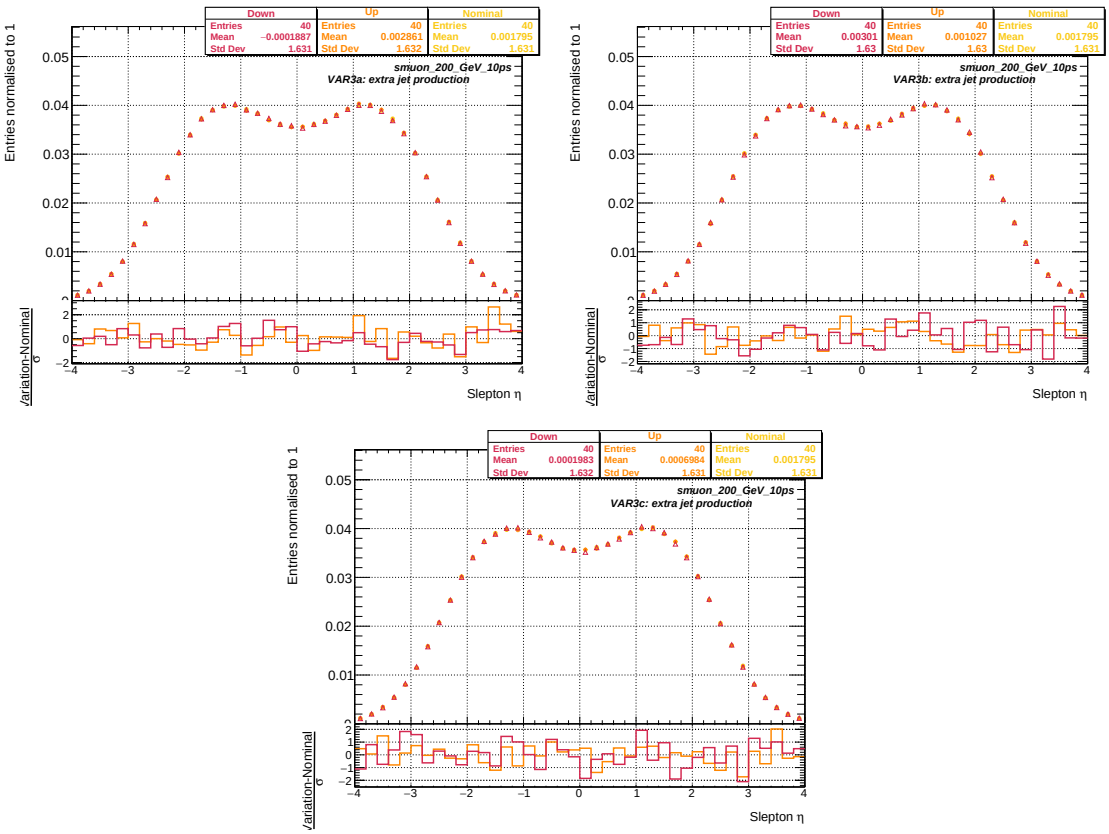

Figure 7.4: The VAR3a (left) and VAR3b (right), then below is VAR3c for the η of the smuon in the smuon 200 GeV 10 ps signal MC sample.

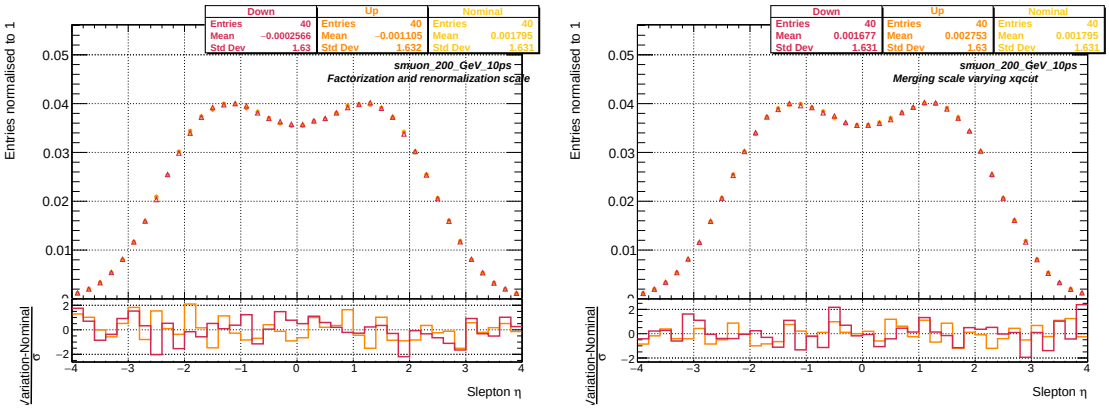

Figure 7.5: The factorization and renormalization scale (left) and the merging scale (right) for the η of the smuon in the smuon 200 GeV 10 ps signal MC sample.

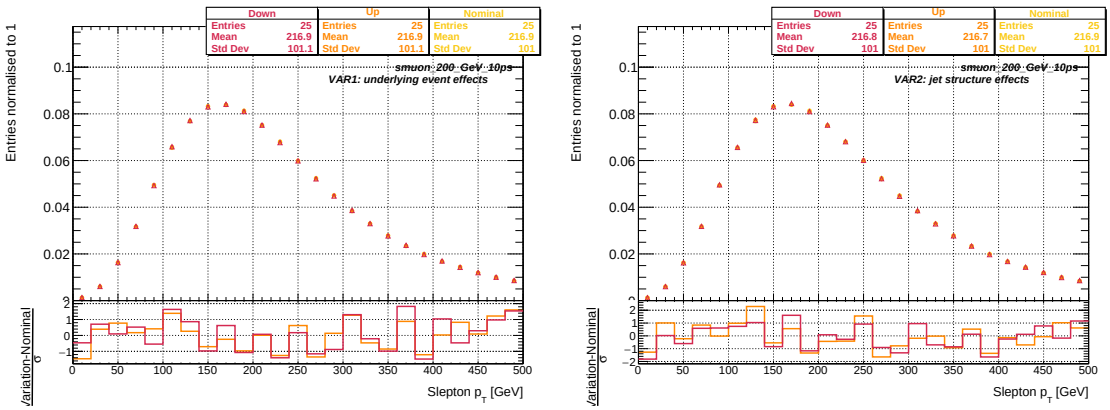

Figure 7.6: The up, down and nominal variations VAR1 (left) and VAR2 (right) for the p_T of the smuon in the smuon 200 GeV 10 ps signal MC sample.

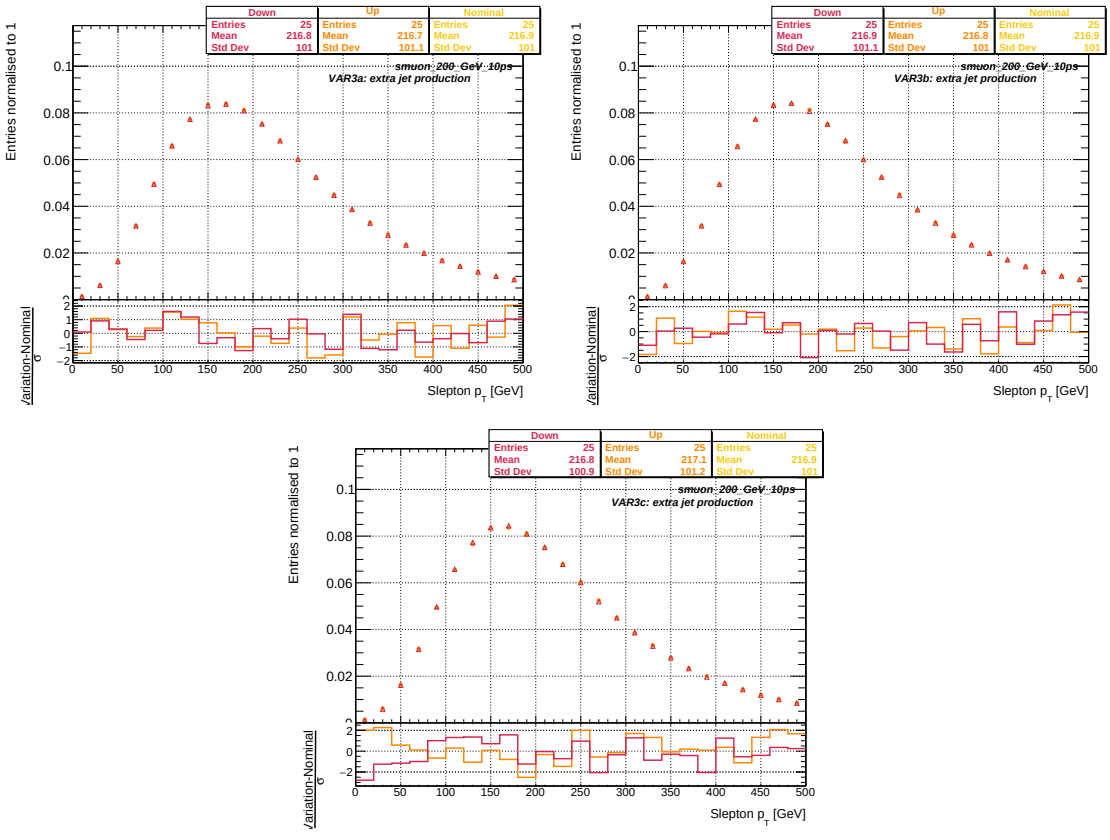

Figure 7.7: The VAR3a (left) and VAR3b (right), then below is VAR3c for the p_T of the smuon in the smuon 200 GeV 10 ps signal MC sample.

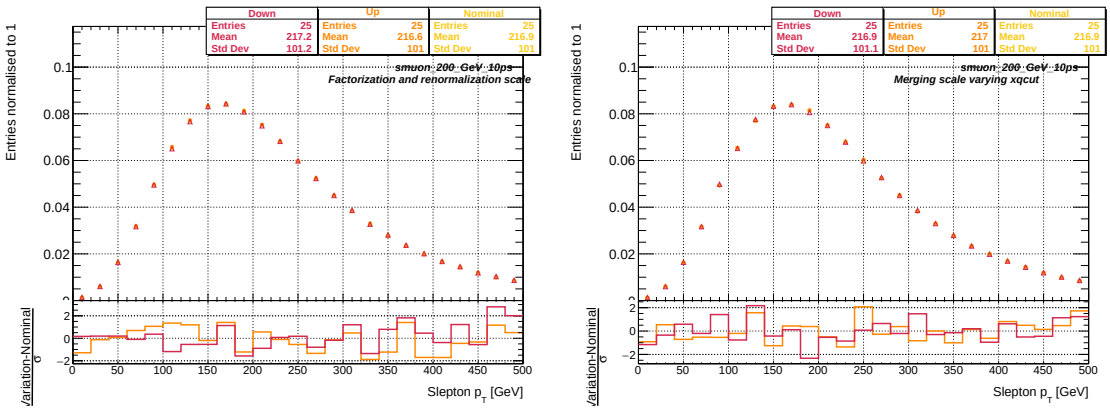

Figure 7.8: The factorization and renormalization scale (left) and the merging scale (right) for the p_T of the smuon in the smuon 200 GeV 10 ps signal MC sample.

Smuon mass [GeV]	Cross section σ [pb]	Down unc. [%]	Up unc. [%]
50	1.377	-3.9	2.3
100	0.09779	-2.1	1.9
200	0.008372	-2.2	2.2
300	0.001746	-2.2	2.3
400	0.0005221	-2.7	2.8
500	0.0001901	-3.0	3.0
600	7.829e-05	-3.6	3.6
700	3.511e-05	-3.8	3.8

Table 7.4: Summary table of cross-sections for slepton pair production for right-handed sleptons $\ell_R^+\ell_R^-$ and the associated uncertainties.

Smuon mass [GeV]	Cross section σ [pb]	Down unc. [%]	Up unc. [%]
50	5.368	-3.9	2.2
100	0.3657	-1.8	1.7
200	0.03031	-2.0	2.0
300	0.006254	-2.1	2.3
400	0.001859	-2.8	2.9
500	0.0006736	-3.2	3.3
600	0.0002763	-3.6	3.6
700	0.0001235	-3.8	3.8

Table 7.5: Summary table for the sum of the right- and left-handed cross-sections for slepton pair production and the associated uncertainties.

7.3 Background Estimation Uncertainties

Lastly the statistical uncertainty for MC is calculated as the square root of the sum of weights squared: $\sqrt{\sum_i w_i^2}$ and the statistical uncertainty for each background estimate is calculated via the standard error propagation of the Poisson statistical uncertainties on the number of events in regions used in the calculation. Signal contamination is shown to be negligible in all channels and there is no correlation between the variables used for the ABCD method. Figures 7.9- 7.11 show the agreement between the observed number of events and estimated using the ABCD method. A flat non-closure systematic is assigned to each channel based on the largest relative difference observed between the predicted and observed number of events in the channel. In the *ee* channel a 2D ABCD background estimation was employed, so the validation is done in gap region 8.

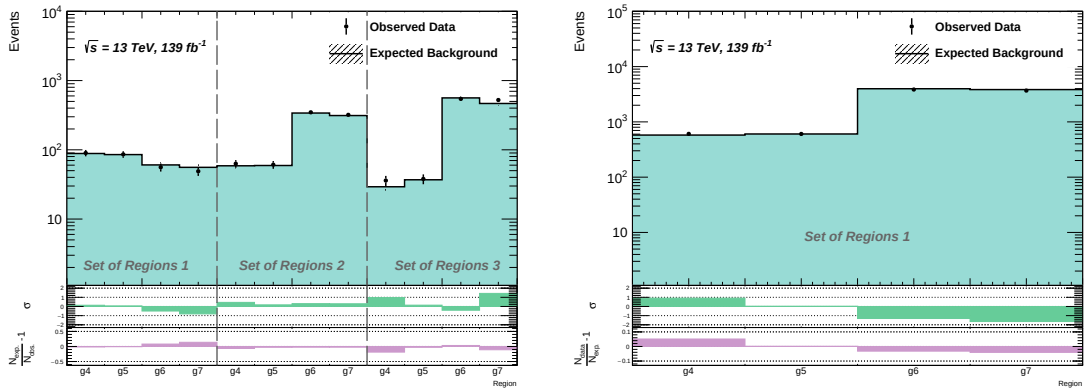

Figure 7.9: Expected and observed number of events in the validation regions g4-g7 for each set of regions in the $\mu\mu$ channel for smuons (left) and staus (right).

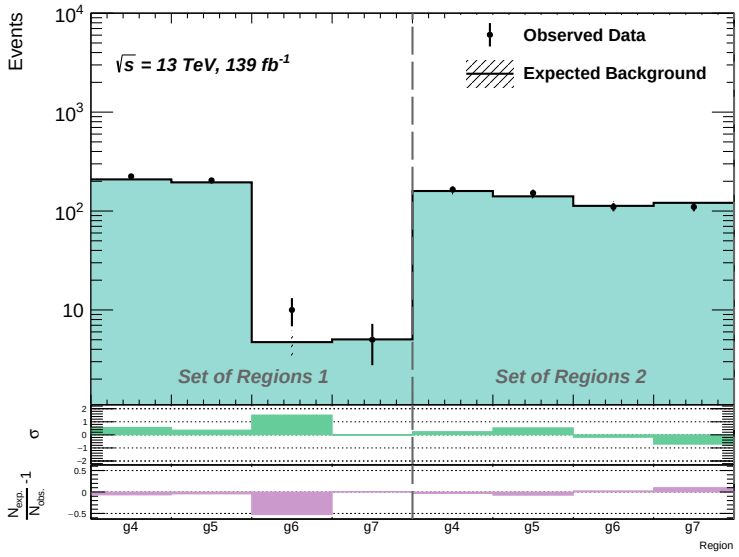

Figure 7.10: Expected and observed number of events in the validation regions g4-g7 for set of regions favourable for stau signal samples in the $e\mu$ channel.

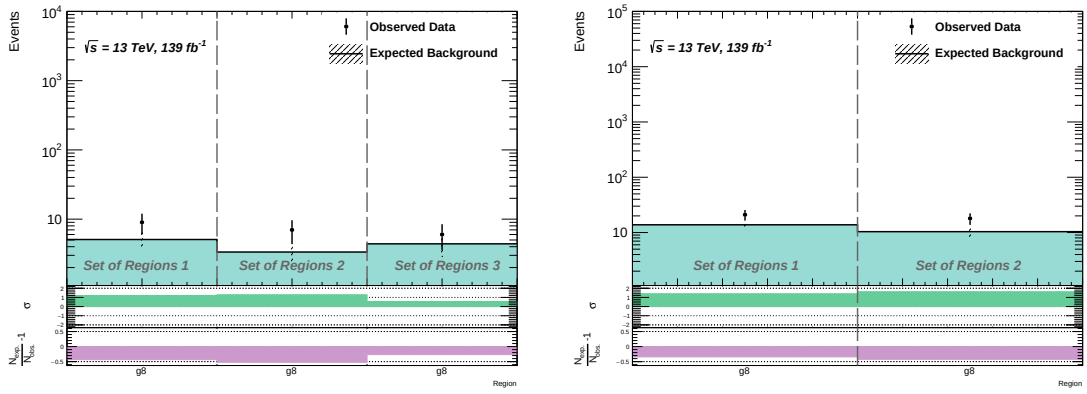

Figure 7.11: Expected and observed number of events in the validation region g8 for sets of regions favourable for selectron (left) and stau (right) signal samples.

Chapter 8

Results

A search for leptons with intermediate displacement in 139 fb^{-1} of pp collision data with $\sqrt{s} = 13$ TeV collected by the ATLAS detector between 2015 and 2018 has been outlined. Three general signal regions were defined based on the flavour combination of the two highest two p_T leptons in the event: SR$\mu\mu$ with two muons, SRee with two electrons and SR$e\mu$ with an electron and muon pair. Further quality requirements defined for each SR were selected to reject fake leptons and increase sensitivity to BSM. In each SR background was estimated and validated in data with an ABCD data-driven method. At the time of this thesis submission, only the SR$\mu\mu$ was unblinded, the results are presented below. Analysis comparison to previous searches and future prospects for all channels is discussed in more detail in Section 8.3.

8.1 Signal Yields

Table 8.1 displays the observed and predicted number of events in SR$\mu\mu$ for sets of Regions 1, 2 and 3. In each set of regions the number of observed events is consistent with the background estimate.

When the number of events, n, is large, the Poisson distribution is well approximated by a Gaussian distribution, where 68.3% of the values in the distribution are 1σ away from the mean. In general the statistical uncertainty of $\pm$ 1σ is then assigned to the observed number, which is $\sigma = \sqrt{n}$ for a Poisson distribution. However, when n is small, the Poisson distribution becomes asymmetric around the mean. To quantify the agreement

Regions	predicted N_H^{bkg}	Observed N_H^{data}
Regions 1	2.06 ± 0.25	1
Regions 2	12.50 ± 1.48	7
Regions 3	17.2 ± 2.62	14

Table 8.1: The number of observed and predicted number of background events in signal region H for each set of Regions 1, 2 and 3. The uncertainty on predicted N_H^{bkg} is calculated via standard error propagation of the Poisson statistical uncertainties on the number of events in regions A, B, C, and E.

between the observed and predicted number of events a confidence interval is constructed with boundaries calculated as:

$$\text{lower} = \frac{\chi^2_{(2n,\alpha)}}{2} \tag{8.1}$$

$$\text{upper} = \frac{\chi^2_{(2(n+1),1-\alpha)}}{2}, \tag{8.2}$$

where $\chi^2_{(i,j)}$ is the chi-square quantile for upper tail probability on i degrees of freedom and $\alpha = \frac{1-0.683}{2} = 0.158$. This leads to the following confidence intervals in the SR$\mu\mu$ channel:

$$2.06 - [0.74, 4.72] \tag{8.3}$$

$$12.50 - [9.01,\ 17.13] \tag{8.4}$$

$$17.2 - [13.09,\ 22.43], \tag{8.5}$$

These are used to assign statistical uncertainty on the background estimates: $2.06^{+2.66}_{-1.32}$, $12.5^{+5.13}_{-3.49}$ and $17.2^{+5.23}_{-4.11}$. The uncertainty that arises from the statistical uncertainty on the number of events in regions A, B, C, and E is then added in quadrature the confidence intervals are: $2.06^{+2.67}_{-1.34}$, $12.5^{+5.34}_{-3.79}$ and $17.2^{+5.85}_{-4.87}$. The difference of the expected number of events and observed number of events is divided by the smallest uncertainty to gauge at the agreement. From this calculation the discrepancy in the set of Regions 1 is 0.79σ, Regions 2 1.45σ and Regions 3 0.66σ, making the observed number of events in agreement with the predicted number of events.

8.2 Interpretation

The expected and observed limits presented in this chapter are computed using an ATLAS framework called HistFitter [72]. The framework combines the observed and expected number of events with background, detector and signal systematics to calculate both model dependant and independent limits using a CL_s method. It derives a confidence interval with a signal-only hypothesis, where $CL_s \leq 5\%$ means the probability of falsely excluding the signal sample is less than or equal to 5%. For a completely background-less search, 3 events are sufficient for a 95% CL_s.

When trying to discover signs of new physics, the null hypothesis, H_0, is the background only hypothesis. It postulates that the signal process does not exist. This hypothesis is tested against the signal hypothesis, H_1, which postulates the existence of the signal, such that the number of observed events equals to the sum of signal and background:

$$\mathbb{E}(n) = \mu S + B, \tag{8.6}$$

where B is the number of predicted background events, S is the number of signal events and μ is the signal strength parameter. Under the background only hypothesis $\mu = 0$. The probability of observing n events is given by the Poisson Distribution:

$$P(n|\mu, S, B) = \frac{(\mu S + B)^n}{n!} e^{-(S+B)}. \tag{8.7}$$

The signal strength parameter is varied to construct a likelihood function, $L(\mu|S, B)$, with the objective of finding a value of μ for which the observed number of events in data is most likely. In the HistFitter framework, the calculation is done in a multi-bin fit across regions A, B, C, E and H (or E, F, G and H for selectrons), where expected number of events in H is constructed as a function of the other regions. While the low signal contamination in regions used for background calculation was necessary for the ABCD method to be valid, the signal strength parameter simultaneously increases signal yields in all regions, improving discovery potential in a simultaneous fit across the regions. In the stau case the multi-bin fit is performed across the channels in SRs only. In each channel a function for the background is constructed, but a single signal strength parameter is kept.

8.2.1 Slepton Limits

For selectron and stau signal samples, the observed number of events is set to the predicted number of events to gauge at the exclusion power of the selected regions. While the predicted exclusion power was already described in SR*ee* for selectrons, the exclusion power of staus was only described in individual channels separately. The expected combined limit and limits in individual channels for staus is presented in Figure 8.2. There are no excess events observed in the SR$\mu\mu$ channel for smuons, therefore actual limits are set on the parameter space, specifically lifetime and mass, of the GSMB SUSY model. The expected and observed exclusion contour is displayed in Figure 8.1.

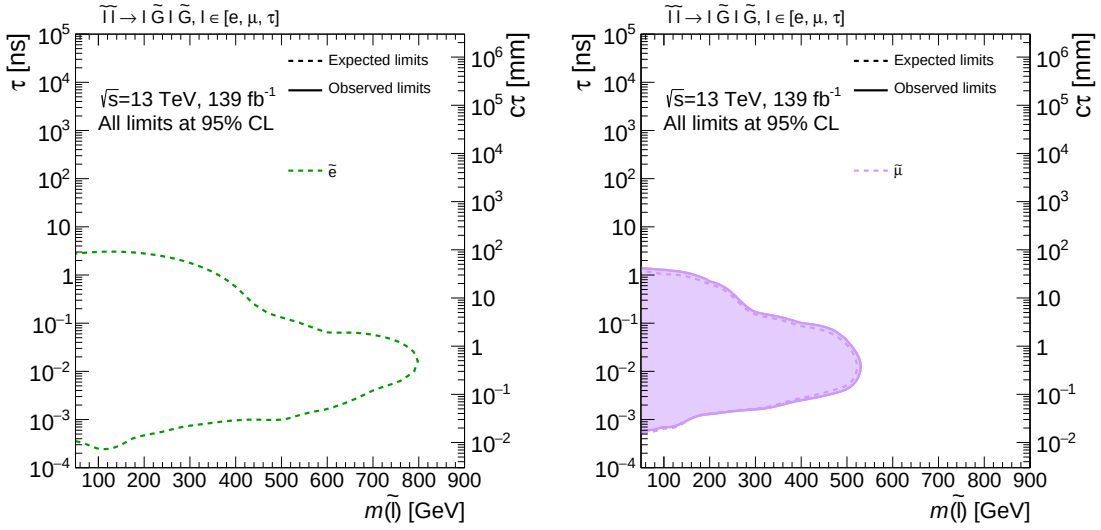

Figure 8.1: Exclusion curves for four different NLSP scenarios: $\tilde{e}$ (left) and $\tilde{\mu}$ (right).

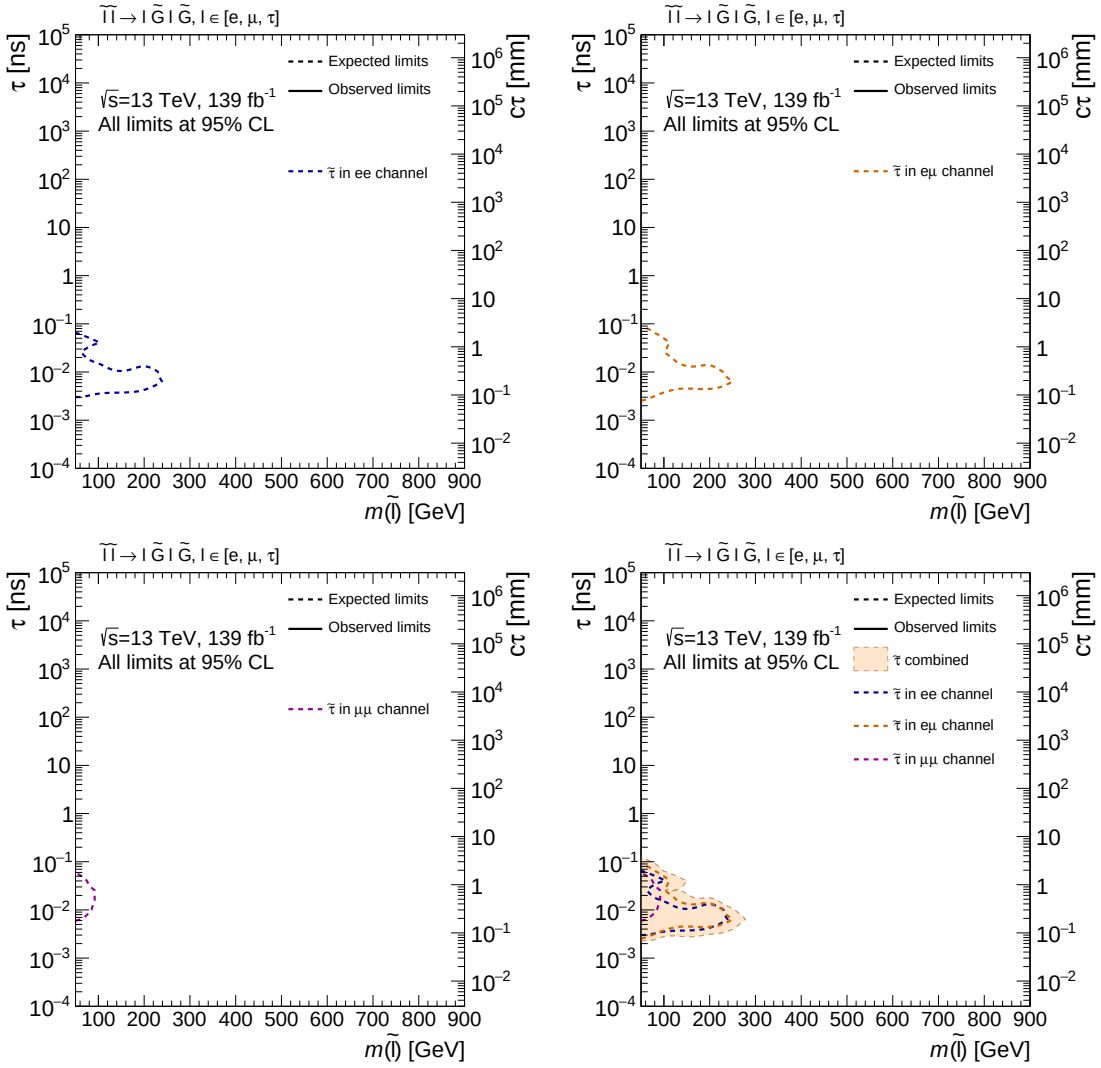

Figure 8.2: Exclusion curves for four different NLSP scenarios, in order: $\tilde{\tau}$ in ee channel, $\tilde{\tau}$ in $e\mu$ channel, $\tilde{\tau}$ in $\mu\mu$ channel and $\tilde{\tau}$ combined across channels.

Comparison to LEP and the ATLAS Run 2 Analysis

A summary of the expected and observed limits is shown in Figure 8.1. The figure includes both right- and left-handed slepton production, which can not be directly compared to the results obtained at LEP. The limits are separated to right-handed only or left-handed only, as well as $\tilde{\tau}_1$ and $\tilde{\tau}_2$ limits and are shown in Figures 8.3- 8.5, where the LEP limit is overlaid where possible. Further, the limits obtained in this analysis are compared to the recent ATLAS Run 2 results described in Section 5.3. Figure 8.6 shows the analysis nicely covers the targeted gap region between the prompt and high d_0 analysis for selectrons and smuons signal samples. There is no sensitivity to the stau signal samples with the prompt analysis, for that reason the ability to reach lower lifetimes with this analysis signifies great progress.

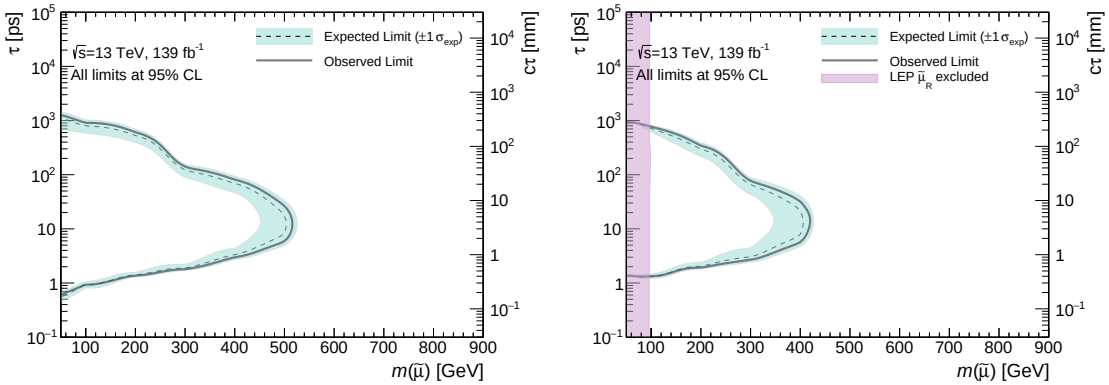

Figure 8.3: Expected (dashed) and observed (solid) exclusion contours for $\tilde{\mu}$ NLSP production as a function of the left-handed smuon, $\tilde{\mu_L}$, (left) and right-handed smuon, $\tilde{\mu_R}$, (right) mass and lifetime at 95% CLs where the purple shaded region shows the region excluded by LEP.

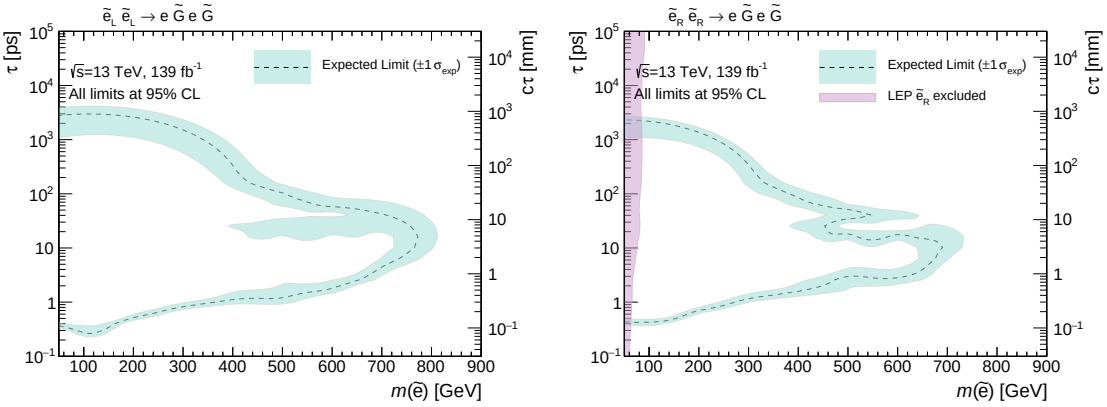

Figure 8.4: Expected (dashed) and observed (solid) exclusion contours for $\tilde{e}$ NLSP production as a function of the left-handed selectron, $\tilde{eL}$, (left) and right-handed selectron, $\tilde{eR}$, (right) mass and lifetime at 95% CLs where the purple shaded region shows the region excluded by LEP.

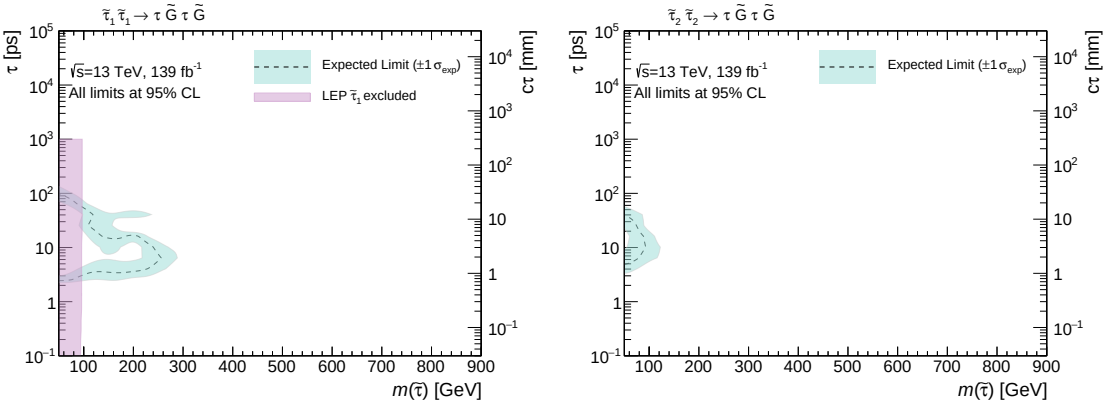

Figure 8.5: Expected (dashed) and observed (solid) exclusion contours for $\tilde{\tau}$ NLSP production as a function of the left-handed stau, $\tilde{\tau_1}$, (left) and right-handed stau, $\tilde{\tau_2}$, (right) mass and lifetime at 95% CLs where the purple shaded region shows the region excluded by LEP.

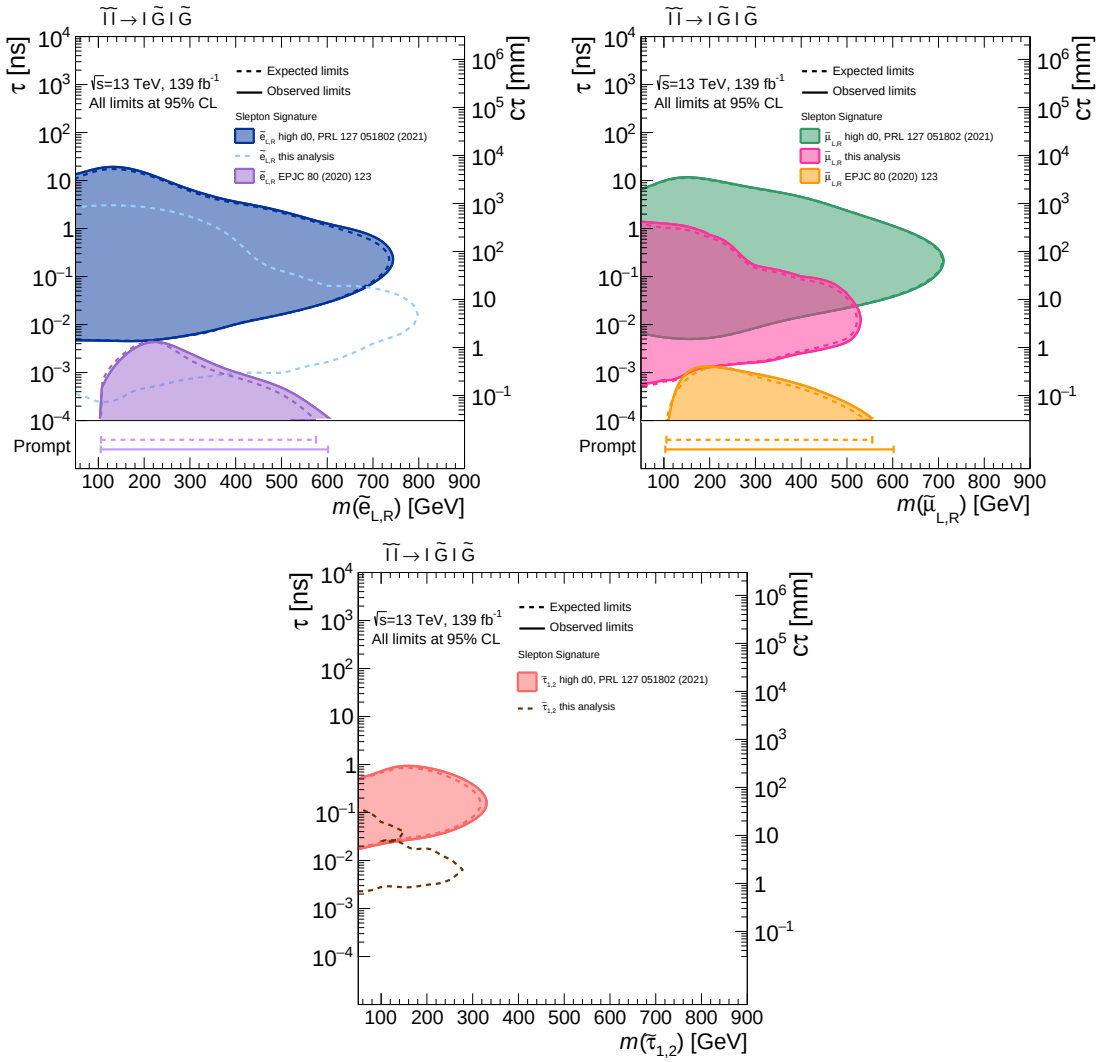

Figure 8.6: Limits on $\tilde{l}$ separated in individual flavours with the prompt and high d_0 limits shown as comparison where possible. In order: $\tilde{e}$, $\tilde{\mu}$, $\tilde{\tau}$.

8.2.2 Model-Independent Limits

In the SR$\mu\mu$ channel model independent limits are additionally set for any new BSM signal that would leave a signature in that phase space. The limits are based on the visible cross section of the new physics process, $\langle A\epsilon\sigma\rangle^{95}_{\text{obs}}$, and the observed, S^{95}_{obs}, and expected, S^{95}_{obs}, number of signal events that would be measured. From Table 8.2 BSM scenarios with visible cross sections above 0.02, 0.04 and 0.06 fb are excluded in the respective sets of Regions 1, Regions 2 and Regions 3.

Signal channel	$\langle A\epsilon\sigma\rangle^{95}_{\text{obs}}$[fb]	S^{95}_{obs}	S^{95}_{exp}	CL_B	$p(s=0)$ (Z)
Regions 1	0.02	3.3	$4.2^{+2.5}_{-1.4}$	0.27	0.50 (0.00)
Regions 2	0.04	5.2	$8.5^{+4.0}_{-2.7}$	0.08	0.50 (0.00)
Regions 3	0.06	8.9	$10.5^{+5.0}_{-3.1}$	0.26	0.50 (0.00)

Table 8.2: Left to right: 95% CL upper limits on the visible cross section ($\langle A\epsilon\sigma\rangle^{95}_{\text{obs}}$) and on the number of signal events (S^{95}_{obs}). The third column (S^{95}_{exp}) shows the 95% CL upper limit on the number of signal events, given the expected number (and $\pm1\sigma$ excursions on the expectation) of background events. The last two columns indicate the CL_B value, i.e. the confidence level observed for the background-only hypothesis, and the discovery p-value ($p(s=0)$).

8.3 Conclusion and Future Improvements

Lifetime was previously a hugely under-explored region of phase space for many BSM theories considered at the LHC. With a paradigm shift to increase focus on long-lived particles for Run 2 analysis, this thesis addressed a gap in coverage existing between the prompt and highly displaced leptons. Despite there being no significant deviation from the predicted background in the di-muon channel, it was shown that the electron channels have far greater sensitivity to heavier sleptons. Due to the larger size of discrepancy between the predicted and observed number of events in both the ee and $e\mu$ channels different background estimation method are presently being explored. The unblinding of those channels is eagerly anticipated.

The signal regions were selected carefully to maximise the sensitivity to the particular GMSB model yet limit the number of individual regions within one channel to ease future reinterpretation of this analysis. Ideally each signal sample would have its own region, nevertheless future versions of this analysis will greatly benefit from other optimisation steps. Firstly, the inclusion of MET in signal region definitions should be explored. This model predicts gravitinos (and neutrinos in $\tilde{\tau}$ decays) which would leave a true MET signature. However, MET modelling comes with additional systematic uncertainties that could hinder the results, especially in cases like the di-electron channel where the greatest limitation was lack of statistics. While the lack of statistics in the electron channel could be overcome by improving electron identification at high d_0, low background yields proved to be very beneficial to increase sensitivity to high mass slepton samples with very low cross sections. In the lifetime regime studied in this analysis, the biggest background contributions come from b-physics processes. It would be desirable to remove this background entirely and work with a background-less hypothesis. This could be easily done with stricter requirements on lepton p_T and isolation. Having said that, the remaining contributions would then be cosmic muons, fake leptons and algorithmic fakes, which are not always well understood or easy to quantify.

Lastly with an already ongoing Run 3, the future analysis of displaced leptons will greatly improve sensitivity to higher masses with additional data, but also with newly developed displaced lepton triggers. The minimal event-level requirements and very loose quality criteria in this analysis makes it applicable to many BSM theories predicting

displaced leptons in the final state. This result will hopefully be reinterpreted and combined with future Run 3 searches to make an inclusive statement about the coverage of searches at the LHC. Like a gap in coverage led to the formulation of this analysis, the inclusion of these results will most likely point to the direction for future searches at HL-LHC.

Appendix A

Industrial Placement

1.1 How much data is enough data for ML?

Machine learning (ML) entails applying artificial intelligence (AI) to create computer programs capable of learning and adapting autonomously, discerning patterns within data rather than relying on explicit human instructions. The effectiveness of ML heavily relies on the quality of the data it learns from. Defining "bad data" varies across contexts—this might encompass labelling errors or the utilisation of a non-representative training set, all resulting in the algorithm generating false predictions. Poor-quality data containing numerous missing values, errors, outliers, and noise also pose a challenge for ML systems to identify underlying patterns effectively. Alternatively, the issue might not lie in the data's quality but rather in its quantity, where an insufficient amount impedes accurate learning and prediction. Even seemingly simple problems often require thousands of examples for effective resolution, while more complex tasks like image or speech recognition may necessitate millions of instances. A well-known paper by Microsoft researchers demonstrated that various ML algorithms, differing in structural complexity, can perform nearly equally well on word-sense disambiguation when provided with ample training data. This computational linguistics challenge involves identifying the intended meaning of a word within a sentence. The Microsoft team specifically focused on selecting the accurate usage of words prone to confusion, such as principle/principal, then/than, to/too/two, and weather/wether. Despite technological advancements and the wealth of accessible data, obtaining a high-quality dataset for ML remains a significant challenge. Many ML projects

falter due to a lack of relevant data or the arduous and costly nature of the data collection process. However, there are strategies to address this issue. Projections suggest that by 2024, about 60% of data used for ML will be synthetic, artificially generated through algorithms and integrated into existing datasets as augmentation. Alongside the synthetic data generation, there has also been development in techniques tackling the data scarcity problem without augmentation, one such example is a few-shot classification method.

1.2 Few-shot classification

Manually annotating classes and their respective examples is a time-intensive process. Notably, the scarcity of examples, particularly in classes like rare species, poses a significant challenge for current vision-based systems to efficiently learn new visual concepts. Unlike the human visual system, which can recognise new classes with minimal labeled examples, machine systems struggle. Few-shot classification addresses this hurdle by leveraging AI's capability to identify similarities within classes and determine if the queried image shares patterns with any of these classes. In each few-shot classification task, there's a labeled support set that acts as a reference catalog. The algorithm then compares individual images from the query set against this catalog. A task is defined as N-way K-shot image classification, with the support set comprising N classes, each containing K labeled images, and a query set comprising Q images. The goal is to classify the Q query images among the N classes, given the N×K images in the support set. When K is exceptionally small ($K < 10$), it qualifies as few-shot image classification. Remarkably, the algorithm doesn't learn to solve a specific task; rather, it sequentially acquires proficiency in solving many other tasks, subsequently improving its ability to learn new tasks. This meta-learning process defines the algorithm's capacity to learn how to learn.

Let's consider teaching an algorithm to identify dog breeds in the before mentioned structure. We craft a 3-way 2-shot image classification system using a training set composed of N distinct dog breeds. For instance, one training task could involve labelling images as Yorkshire Terrier, Boxer, and Labradoodle, utilising $3\times2 = 6$ labeled examples of these breeds. Another task might entail labelling images as Labrador, Saint-Bernard, or Pug, employing $3\times2 = 6$ labeled examples of these breeds. Each training task maintains a consistent structure: 3 classes with 2 images per class, yet each task pertains to different

breeds of dogs. The meta-training process involves a sequence of these tasks, allowing the model to improve "through experience and task frequency". Most few-shot classification methods follow a two-step approach to classify images:

1. use a convolutional neural network for feature extraction of the images in the support and query sets

2. classify the query images by comparing them to the support images

As the algorithm evaluates an image from the query set against images in the support set, it doesn't conduct a pixel-to-pixel comparison. Instead, it assesses their positions within a feature space. Utilising a convolutional neural network, the algorithm extracts features from images, transforming each image into a one-dimensional vector within a feature space. Subsequently, the query images undergo classification via metric learning, where the classification of a query image is determined by its proximity to the support image set. The approach for distance calculation and classification strategies can be either arbitrarily chosen or fine-tuned to suit the specific classification task. For instance, in one scenario, we might employ the Euclidean distance among neighbours and the k-Nearest Neighbours classification method. In recent times, Prototypical Networks have gained traction. Here, query images aren't directly compared to all support set images; instead, they're compared to a singular prototype representing each class. These prototypes are computed using all features from a support class, ideally representing the class centre within the feature space. Typically, this involves computing the mean of the features, although any differentiable function could be employed. Subsequently, query images are classified based on their distances from these prototypes within the feature space.

1.3 Computer Says No

The 'Computer Says No' documentary showcased an instance where a robot evaluated the work of two makeup artists using scores from an algorithm employing the few-shot classification method. The algorithm employed was from an open-source package called Easyfsl, displaying impressive classification capabilities, notably demonstrated on the CU-Birds dataset. In the documentary, the algorithm adopted a 2-way 3-shot classification

structure, leveraging a pre-trained convolutional network for feature extraction. The chosen convolutional network, mobilenet_v3_large, commonly used in mobile phones for classification, object detection, and semantic segmentation, had been pre-trained on the ImageNet dataset. The ML model was then trained using tasks crafted from the YouTube Makeup (YMU) dataset. The YMU dataset comprised four images (two before and two after makeup application) of 151 subjects, totalling 604 images. The dataset showcased makeup variations from subtle to heavy, focusing primarily on eye makeup products, with additional changes in skin tone due to foundation and lipstick application. In a few instances, drastic changes in hairstyle were also observed. The algorithm underwent training on 1000 tasks constructed from 95% of the dataset and tested on the remaining 5%, achieving an accuracy score of 96.4%.

During evaluation, the trained model received two images of the same subject, each with makeup done by a different artist, and generated a classifier score used to rank the images based on makeup quality. Interestingly, alongside the makeup-subject images, the algorithm was presented with an image of the documentary presenter wearing makeup. Surprisingly, the presenter received a higher score than both subjects. However, this might not surprise those unfamiliar with the documentary. The images presented to the algorithm are displayed in Figure A.1. The presenter, in fact, is a black male, while the evaluated subject is a white female. The discrepancy arises from the fact that the algorithm was trained solely on images of Caucasian females. Consequently, when presented with images of a black male, it consistently scored them higher than the images of white females. This exemplifies the consequences of bad data discussed in the introduction—the training dataset inadequately represented the broader population, leading to biased outputs.

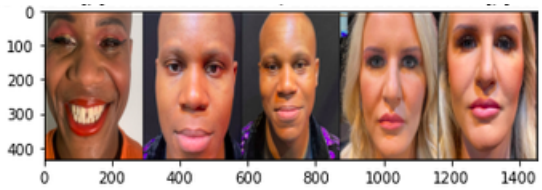

Figure A.1: Query images produced during the evaluation ordered by "goodness" of makeup from left to right.

The algorithm's output, a makeup goodness score, operates as a distance metric typical

for few-shot classification. With a 2-way 3-shot classifier, the dataset was divided into makeup and no-makeup classes. The ranking score reflects the distance from the image to the makeup class prototype, indicating the likelihood of the subject wearing makeup, not necessarily the makeup quality. Misinterpretation of algorithm outputs is a common pitfall in ML usage, where users misapply or misinterpret the model's intended purpose. Despite utilising good quality data, appropriate model structures, and finely tuned parameters, the algorithm was applied to solve the wrong problem. The documentary's intentionally flawed algorithm serves as a crucial reminder: as AI permeates various sectors, human errors in algorithm construction persist. While AI advances rapidly across diverse domains like healthcare, self-driving cars, and robotics, human fallibility remains an inherent aspect of AI development.

References

[1] ATLAS Collaboration. "Search for pairs of muons with small displacements in pp collisions at s=13 TeV with the ATLAS detector". In: *Physics Letters B* 846 (2023), p. 138172. ISSN: 0370-2693. DOI: https://doi.org/10.1016/j.physletb.2023.138172. URL: https://www.sciencedirect.com/science/article/pii/S0370269323005063.

[2] Melissa Yexley. "A Search For Long Lived Particles that Decay to Muons Using the ATLAS Detector". English. PhD thesis. Lancaster University, July 2023. DOI: 10.17635/lancaster/thesis/2047.

[3] G. Sawyer (Producer). *Computer Says No*. United Kingdom, BBC Three. 2022.

[4] David Galbraith. *UX: Standard Model of Particle Physics*. 1999. URL: https://davidgalbraith.org/portfolio/ux-standard-model-of-the-standard-model/ (visited on 08/08/2023).

[5] ATLAS Collaboration. "Observation of a new particle in the search for the Standard Model Higgs boson with the ATLAS detector at the LHC". In: *Physics Letters B* 716.1 (Sept. 2012), 1–29. ISSN: 0370-2693. DOI: 10.1016/j.physletb.2012.08.020. URL: http://dx.doi.org/10.1016/j.physletb.2012.08.020.

[6] STEPHEN P. MARTIN. "A SUPERSYMMETRY PRIMER". In: *Advanced Series on Directions in High Energy Physics*. WORLD SCIENTIFIC, July 1998, 1–98. DOI: 10.1142/9789812839657_0001. URL: http://dx.doi.org/10.1142/9789812839657_0001.

[7] K. Freese. "Review of Observational Evidence for Dark Matter in the Universe and in upcoming searches for Dark Stars". In: *EAS Publications Series* 36 (2009), 113–126.

ISSN: 1638-1963. DOI: 10.1051/eas/0936016. URL: http://dx.doi.org/10.1051/eas/0936016.

[8] Yu A Gelfand and E P Likhtman. "Extension of the algebra of Poincare group generators and violation of P invariance". In: *JETP Lett.* 13.8 (1971), pp. 323–325. URL: https://cds.cern.ch/record/433516.

[9] CSABA CSÁKI. "THE MINIMAL SUPERSYMMETRIC STANDARD MODEL". In: *Modern Physics Letters A* 11.08 (Mar. 1996), 599–613. ISSN: 1793-6632. DOI: 10.1142/s021773239600062x. URL: http://dx.doi.org/10.1142/S021773239600062X.

[10] Christopher Kolda. "Gauge-mediated supersymmetry breaking: Introduction, review and update". In: *Nuclear Physics B - Proceedings Supplements* 62.1-3 (1998), pp. 266–275. DOI: 10.1016/s0920-5632(97)00667-1. URL: https://doi.org/10.1016\%2Fs0920-5632\%2897\%2900667-1.

[11] Savas Dimopoulos et al. "Experimental Signatures of Low Energy Gauge-Mediated Supersymmetry Breaking". In: *Phys. Rev. Lett.* 76 (19 1996), pp. 3494–3497. DOI: 10.1103/PhysRevLett.76.3494. URL: https://link.aps.org/doi/10.1103/PhysRevLett.76.3494.

[12] Giacomo Sguazzoni. "GMSB Susy Searches at LEP". In: (2001), pp. 457–462. URL: https://cds.cern.ch/record/2296652.

[13] S. Ambrosanio, Graham D. Kribs, and Stephen P. Martin. "Signals for gauge-mediated supersymmetry-breaking models at the CERN LEP 2 collider". In: *Phys. Rev. D* 56 (3 1997), pp. 1761–1777. DOI: 10.1103/PhysRevD.56.1761. URL: https://link.aps.org/doi/10.1103/PhysRevD.56.1761.

[14] Savas Dimopoulos and David Sutter. "The supersymmetric flavor problem". In: *Nuclear Physics B* 452.3 (1995), pp. 496–512. DOI: 10.1016/0550-3213(95)00421-n. URL: https://doi.org/10.1016\%2F0550-3213\%2895\%2900421-n.

[15] Jared A. Evans and Jessie Shelton. "Long-lived staus and displaced leptons at the LHC". In: *Journal of High Energy Physics* 2016.4 (2016), pp. 1–39. DOI: 10.1007/jhep04(2016)056. URL: https://doi.org/10.1007\%2Fjhep04\%282016\%29056.

[16] CERN. *The History of CERN*. URL: https://timeline.web.cern.ch/timeline-header/89 (visited on 12/11/2023).

[17] Forthommel. *CERN accelerator complex*. 2021. URL: https://commons.wikimedia.org/wiki/File:Cern-accelerator-complex.svg (visited on 08/08/2023).

[18] ATLAS Collaboration. *ATLAS Luminosity Public results Run 2*. URL: https://twiki.cern.ch/twiki/bin/view/AtlasPublic/LuminosityPublicResultsRun2 (visited on 08/08/2023).

[19] A. Airapetian et al. "ATLAS: Detector and physics performance technical design report. Volume 1". In: (May 1999).

[20] The ATLAS Collaboration. "The ATLAS Experiment at the CERN Large Hadron Collider". In: *Journal of Instrumentation* 3.08 (2008), S08003. DOI: 10.1088/1748-0221/3/08/S08003. URL: https://dx.doi.org/10.1088/1748-0221/3/08/S08003.

[21] ICEPPl. *ATLAS detector*. URL: https://www.icepp.s.u-tokyo.ac.jp/en/information/20181012.html (visited on 08/08/2023).

[22] Izaak Neutelings. *ATLAS coordinate system*. URL: https://tikz.net/axis3d_cms/ (visited on 08/08/2023).

[23] ATLAS Collaboration. *ATLAS Inner Detector structure*. URL: https://atlas.cern/updates/experiment-briefing/inner-detector-alignment (visited on 08/08/2023).

[24] ATLAS Collaboration. "ATLAS pixel detector electronics and sensors". In: *JINST* 3 (2008), P07007. DOI: 10.1088/1748-0221/3/07/P07007. URL: https://cds.cern.ch/record/1119279.

[25] ATLAS Collaboration. "The barrel modules of the ATLAS semiconductor tracker". In: *Nuclear Instruments and Methods in Physics Research Section A: Accelerators, Spectrometers, Detectors and Associated Equipment* 568.2 (2006), pp. 642–671. ISSN: 0168-9002. DOI: https://doi.org/10.1016/j.nima.2006.08.036. URL: https://www.sciencedirect.com/science/article/pii/S016890020601388X.

[26] ATLAS Collaboration. "The ATLAS semiconductor tracker end-cap module". In: *Nuclear Instruments and Methods in Physics Research Section A: Accelerators, Spectrometers, Detectors and Associated Equipment* 575.3 (2007), pp. 353–389. ISSN: 0168-9002. DOI: https://doi.org/10.1016/j.nima.2007.02.019. URL: https://www.sciencedirect.com/science/article/pii/S0168900207003270.

[27] ATLAS Collaboration. "The ATLAS TRT Barrel Detector". In: *Journal of Instrumentation* 3.02 (2008), P02014. DOI: 10.1088/1748-0221/3/02/P02014. URL: https://dx.doi.org/10.1088/1748-0221/3/02/P02014.

[28] ATLAS Collaboration. "The ATLAS TRT end-cap detectors". In: *Journal of Instrumentation* 3.10 (2008), P10003. DOI: 10.1088/1748-0221/3/10/P10003. URL: https://dx.doi.org/10.1088/1748-0221/3/10/P10003.

[29] *ATLAS tile calorimeter: Technical Design Report*. Technical design report. ATLAS. Geneva: CERN, 1996. DOI: 10.17181/CERN.JRBJ.7028. URL: https://cds.cern.ch/record/331062.

[30] Nikiforos Nikiforou. "Performance of the ATLAS Liquid Argon Calorimeter after three years of LHC operation and plans for a future upgrade". In: (2013). "Comments: 12 pages, 25 figures, Proceedings of talk presented in "Advancements in Nuclear Instrumentation Measurement Methods and their Applications", Marseille, 2013". DOI: 10.1109/ANIMMA.2013.6728060. arXiv: 1306.6756. URL: https://cds.cern.ch/record/1558820.

[31] *ATLAS muon spectrometer: Technical Design Report*. Technical design report. ATLAS. Geneva: CERN, 1997. URL: https://cds.cern.ch/record/331068.

[32] Fabian Kuger. "Signal Formation Processes in Micromegas Detectors and Quality Control for large size Detector Construction for the ATLAS New Small Wheel". In: (2017).

[33] The ATLAS collaboration. "Operation of the ATLAS trigger system in Run 2". In: *Journal of Instrumentation* 15.10 (Oct. 2020), P10004–P10004. ISSN: 1748-0221. DOI: 10.1088/1748-0221/15/10/p10004. URL: http://dx.doi.org/10.1088/1748-0221/15/10/P10004.

[34] ATLAS Collaboration. "Operation of the ATLAS trigger system in Run 2". In: *JINST* 15.10 (2020). 60 pages in total, author list starting page 44, 19 figures, 3 tables, submitted to JINST, All figures including auxiliary figures are available at https://atlas.web.cern.ch/Atlas/GROUPS/PHYSICS/PAPERS/TRIG-2019-04/, P10004. DOI: 10.1088/1748-0221/15/10/P10004. arXiv: 2007.12539. URL: https://cds.cern.ch/record/2725146.

[35] Elmar Ritsch. "Fast Calorimeter Punch-Through Simulation for the ATLAS Experiment". diplomathesis. University of Innsbruck, 2011.

[36] ATLAS Collaboration. *ATLAS Track Reconstruction*. URL: https://atlassoftwaredocs.web.cern.ch/trackingTutorial/idoverview/ (visited on 08/08/2023).

[37] Margaret Susan Lutz. "Large Radius Tracking at the ATLAS Experiment". In: *PoS* EPS-HEP2017 (2018), p. 708. DOI: 10.22323/1.314.0708. URL: https://cds.cern.ch/record/2670106.

[38] *ATLAS Software Documentation*. URL: https://atlassoftwaredocs.web.cern.ch/trackingTutorial/idoverview/ (visited on 10/01/2023).

[39] *ATLAS Software Documentation*. URL: https://atlassoftwaredocs.web.cern.ch/trackingTutorial/idoverview/ (visited on 10/01/2023).

[40] ATLAS Collaboration. "Electron reconstruction and identification in the ATLAS experiment using the 2015 and 2016 LHC proton-proton collision data at $\sqrt{s}$ = 13 TeV". In: *The European Physical Journal C* 79.8 (2019). DOI: 10.1140/epjc/s10052-019-7140-6. URL: https://doi.org/10.1140\%2Fepjc\%2Fs10052-019-7140-6.

[41] I. Sanderswood. "Optimization of the Adaptive Multi Vertex Finder in ATLAS". Unpublished paper. 2019.

[42] *Performance of ATLAS Pixel Detector and Track Reconstruction at the start of Run 3 in LHC Collisions at $\sqrt{s}$ = 900 GeV*. Tech. rep. All figures including auxiliary figures are available at https://atlas.web.cern.ch/Atlas/GROUPS/PHYSICS/PUBNOTES/ATL-PHYS-PUB-2022-033. Geneva: CERN, 2022. URL: https://cds.cern.ch/record/2814766.

[43] ATLAS Collaboration. *Athena*. Version 22.0.1. Apr. 2019. DOI: 10.5281/zenodo.2641997. URL: https://doi.org/10.5281/zenodo.2641997.

[44] W. Waltenberger. "Development of Vertex Finding and Vertex Fitting Algorithms for CMS". PhD thesis. Institut für Hochenergiephysik der Österreichischen Akademie der Wissenschaften, 1996.

[45] Rudolf Frühwirth and Are Strandlie. "Pattern Recognition, Tracking and Vertex Reconstruction in Particle Detectors". In: (Jan. 2021). DOI: 10.1007/978-3-030-65771-0.

[46] The ATLAS Collaboration. *Performance of vertex reconstruction algorithms for detection of new long-lived particle decays within the ATLAS inner detector*. ATL-PHYS-PUB-2019-013. 2019. URL: https://cds.cern.ch/record/2669425/files/ATL-PHYS-PUB-2019-013.pdf.

[47] *Characterization of Interaction-Point Beam Parameters Using the pp Event-Vertex Distribution Reconstructed in the ATLAS Detector at the LHC*. Tech. rep. All figures including auxiliary figures are available at https://atlas.web.cern.ch/Atlas/GROUPS/PHYSICS/CO CONF-2010-027. Geneva: CERN, 2010. URL: https://cds.cern.ch/record/1277659.

[48] V Kostyukhin. *VKalVrt - package for vertex reconstruction in ATLAS.* Tech. rep. revised version number 1 submitted on 2003-09-24 11:10:53. Geneva: CERN, 2003. URL: https://cds.cern.ch/record/685551.

[49] The ATLAS Collaboration. *Search for long-lived, massive particles in events with displaced vertices and missing transverse momentum in $\sqrt{s}$ = 13 TeV pp collisions with the ATLAS detector*. CERN-EP-2017-202. 2018. URL: https://cds.cern.ch/record/2254594/files/ATL-COM-PHYS-2017-205.pdf.

[50] Lawrence Lee et al. "Collider searches for long-lived particles beyond the Standard Model". In: *Progress in Particle and Nuclear Physics* 106 (2019), pp. 210–255. ISSN: 0146-6410. DOI: https://doi.org/10.1016/j.ppnp.2019.02.006. URL: https://www.sciencedirect.com/science/article/pii/S0146641019300109.

[51] Lesya Horyn. "Searching for Long Lived Particles". In: *A Search for Displaced Leptons in the ATLAS Detector*. Cham: Springer International Publishing, 2022, pp. 73–79. ISBN: 978-3-030-91672-5. DOI: 10.1007/978-3-030-91672-5_7. URL: https://doi.org/10.1007/978-3-030-91672-5_7.

[52] G. Abbiendi et al. "Searches for gauge-mediated supersymmetry breaking topologies in e^+e^- collisions at LEP2". In: *Eur. Phys. J. C* 46 (2006), pp. 307–341. DOI: 10.1140/epjc/s2006-02524-8. arXiv: hep-ex/0507048.

[53] CMS Collaboration. "Search for Displaced Supersymmetry in Events with an Electron and a Muon with Large Impact Parameters". In: *Physical Review Letters* 114.6 (Feb. 2015). DOI: 10.1103/physrevlett.114.061801. URL: https://doi.org/10.1103\%2Fphysrevlett.114.061801.

[54] CMS Collaboration. "Searches for long-lived charged particles in pp collisions at $\sqrt{s}$ =7 and 8 TeV". In: *Journal of High Energy Physics* 2013.7 (July 2013). DOI: 10.1007/jhep07(2013)122. URL: https://doi.org/10.1007\%2Fjhep07\%282013\%29122.

[55] CMS Collaboration. "Search for disappearing tracks in proton-proton collisions at $\sqrt{s} = 8TeV$". In: *Journal of High Energy Physics* 2015.1 (Jan. 2015). DOI: 10.1007/jhep01(2015)096. URL: https://doi.org/10.1007\%2Fjhep01\%282015\%29096.

[56] ATLAS Collaboration. "Search for charginos nearly mass degenerate with the lightest neutralino based on a disappearing-track signature in *pp* collisions at $\sqrt{s}$ = 13 TeV with the ATLAS detector". In: *Physical Review D* 88.11 (Dec. 2013). DOI: 10.1103/physrevd.88.112006. URL: https://doi.org/10.1103\%2Fphysrevd.88.112006.

[57] CMS Collaboration. "Search for long-lived particles decaying to leptons with large impact parameter in proton-proton collisions at $\sqrt{s}$ = 13 TeV". In: *Eur. Phys. J. C* (). DOI: https://doi.org/10.1140/epjc/s10052-022-10027-3. URL: https://arxiv.org/abs/2110.04809v2.

[58] ATLAS Collaboration. "Search for electroweak production of charginos and sleptons decaying into final states with two leptons and missing transverse momentum in pp collisions using the ATLAS detector". In: *The European Physical Journal C* 80.2

(Feb. 2020). DOI: 10.1140/epjc/s10052-019-7594-6. URL: https://doi.org/10.1140.

[59] ATLAS Collaboration. "Search for Displaced Leptons in pp Collisions with the ATLAS Detector". In: *Physical Review Letters* 127.5 (July 2021). DOI: 10.1103/physrevlett.127.051802. URL: https://doi.org/10.1103.

[60] ATLAS Collaboration. *Beam Spot Public Results*. URL: https://twiki.cern.ch/twiki/bin/view/AtlasPublic/BeamSpotPublicResults (visited on 09/25/2023).

[61] T. Golling et al. "The ATLAS data quality defect database system". In: *The European Physical Journal C* 72.4 (2012). DOI: 10.1140/epjc/s10052-012-1960-y. URL: https://doi.org/10.1140\%2Fepjc\%2Fs10052-012-1960-y.

[62] Stefano Carrazza, Stefano Forte, and Juan Rojo. *Parton Distributions and Event Generators*. 2013. arXiv: 1311.5887 [hep-ph].

[63] J. Alwall et al. "The automated computation of tree-level and next-to-leading order differential cross sections, and their matching to parton shower simulations". In: *Journal of High Energy Physics* 2014.7 (2014). DOI: 10.1007/jhep07(2014)079. URL: https://doi.org/10.1007\%2Fjhep07\%282014\%29079.

[64] *ATLAS Pythia 8 tunes to 7 TeV data*. Tech. rep. All figures including auxiliary figures are available at https://atlas.web.cern.ch/Atlas/GROUPS/PHYSICS/PUBNOTES/ATL-PHYS-PUB-2014-021. Geneva: CERN, 2014. URL: https://cds.cern.ch/record/1966419.

[65] S. Agostinelli et al. "GEANT4 – a simulation toolkit". In: *Nucl. Instrum. Meth. A* 506 (2003), p. 250. DOI: 10.1016/S0168-9002(03)01368-8.

[66] Jan Kretzschmar. "Standard Model physics at the LHC". In: (2019). "Contribution to the volume "From my Vast Repertoire - the Legacy of Guido Altarelli" : 24 pages, 13 figures", pp. 153–171. DOI: 10.1142/9789813238053_0009. arXiv: 1803.10800. URL: https://cds.cern.ch/record/2644360.

[67] Lukas Heinrich, Matthew Feickert, and Giordon Stark. *pyhf: v0.6.3*. Version 0.6.3. 2022. DOI: 10.5281/zenodo.1169739. URL: https://doi.org/10.5281/zenodo.1169739.

[68] Lukas Heinrich et al. "pyhf: pure-Python implementation of HistFactory statistical models". In: *Journal of Open Source Software* 6.58 (2021), p. 2823. DOI: 10.21105/joss.02823.

[69] Gregor Kasieczka et al. "Automating the ABCD method with machine learning". In: *Physical Review D* 103.3 (Feb. 2021). ISSN: 2470-0029. DOI: 10.1103/physrevd.103.035021. URL: http://dx.doi.org/10.1103/PhysRevD.103.035021.

[70] Carleton University (CA). *Dealing with correlation in the ABCD method*. URL: https://indico.cern.ch/event/1017241/contributions/4269394/attachments/2214289/3748328/Carleton_ejs_IR_Correlation-Correction_20Mar21.pdf (visited on 12/11/2023).

[71] ATLAS Collaboration. *Luminosity determination in pp collisions at* $\sqrt{s} = 13$ *TeV using the ATLAS detector at the LHC*. 2022. arXiv: 2212.09379 [hep-ex].

[72] M. Baak et al. "HistFitter software framework for statistical data analysis". In: *The European Physical Journal C* 75.4 (Apr. 2015). ISSN: 1434-6052. DOI: 10.1140/epjc/s10052-015-3327-7. URL: http://dx.doi.org/10.1140/epjc/s10052-015-3327-7.